

CONVECTION, DIFFUSION, THERMOPHORESIS AND
ELECTRIC FIELD EFFECTS ON DIESEL SOOT
DEPOSITION IN A COOLED EXHAUST CHANNEL

CONVECTION, DIFFUSION, THERMOPHORESIS AND
ELECTRIC FIELD EFFECTS ON DIESEL SOOT
DEPOSITION IN A COOLED EXHAUST CHANNEL

by

EMMANUEL T. DELA CRUZ

A thesis

submitted to the School of Graduate Studies

in partial fulfillment of the
requirements for the degree of

Master of Applied Science

McMaster University

Hamilton, Ontario, Canada

© by Emmanuel T. dela Cruz, October 2007

Master of Applied Science

McMaster University

Hamilton, Ontario

TITLE: Convection, Diffusion, Thermophoresis and Electric Field
Effects on Diesel Soot Deposition in a Cooled Exhaust Channel

AUTHOR: Emmanuel T. dela Cruz, B. Eng

SUPERVISORS: Drs. A. A. Berezin, J. S. Chang

NUMBER OF PAGES: 130 pages (i-xvi, 1-114)

ABSTRACT

New demands and tighter government legislations on greenhouse gases and pollutants, especially for those produced by diesel engines, there has been much focus on developing more efficient diesel engine designs and pollution control devices. There are several pollution control devices currently being implemented in diesel engines such as, diesel particulate filters, selective reduction catalyst, electrostatic filters, exhaust gas recirculation systems, etc. Diesel particulate matter is of particular importance especially when deposited because of its corrosive and thermal insulating nature.

There are many complex mechanisms involved in fine particle deposition. This study will focus on the main deposition mechanisms such as convection, diffusion, thermophoresis and electric field effects. The objective of this study was to evaluate experimentally the mechanisms of diesel soot deposition in a rectangular (RWCS) and cylindrical (CWCS) wall cooled sections to evaluate thermophoretic effects. In addition, the coaxial cylindrical wall cooled section with additional with coaxial wire electrode was used to study applied electric field effect (CCWCSE) on soot deposition. A non-destructive Real-Time Neutron Radiography technique was used to evaluate the soot deposition thickness profiles inside the cooled sections.

The experiments were conducted using diesel engine exhaust from a single cylinder diesel engine operated at fixed 2.4kW, at a exhaust gas mass flow rate of 20 kg/hr with exposure times ranging 0 to 3hrs, coolant temperatures from 20 to 40 °C and exhaust gas temperatures from 250 and 270 °C. The resulting Reynolds Number based on the mass flow rate per cross-sectional area times the hydraulic diameter was 6300 for the RWCS and 9000 for the CWCS and CCWCSE.

The results show that for the RWCS, the soot deposition pattern qualitatively matched the cooling water channel outer wall surface temperature profile along with

thicker deposition at the entrance region due to convection effects. For the CWCS, the deposition was more uniformly distributed throughout the device. It was observed for both devices that as the mean soot deposition thickness increases with increasing exhaust gas exposure time and decreasing wall cooling temperature. Finally the experimental results for the CCWCSE shows that the soot deposition was enhanced by a positive or negative applied electric field.

To my Mother and Father.

ACKNOWLEDGEMENTS

I would like to express my sincere gratitude to my supervisors Dr. Jen-Shih Chang and Dr. Alexander Berezin, as well as Dr. Drazena Brocilo, Dr. Dan Ewing and Dr. Glenn Harvel for their invaluable guidance, experience and supervision throughout this work.

I would also like to express my sincere gratitude to the Thermal Products Research Group at DANA Co-Long Mfg, especially Dr. Jim Cotton, Dr. Mike Bardeleben and Edward Gerges for their valuable discussions and comments as well as the Ontario Centre for Excellence and DANA Co-Long Mfg for their financial support for this project.

I would like to thank John Colenbrander, Dr. Cecile Ayrault, Behrooz Komeili and the various tenants of NRB B109 for their assistance and personal support.

The technical assistance of Anas Khaial, TS Fabrication, Paul Bray, Barry Diacon, Glen Leinweber, Mike Butler and his staff at the McMaster Nuclear Reactor was valued and greatly appreciated.

Finally I would like to give my wholehearted gratitude to my family and friends, in particular my Mother, Father, Ate Jeng and Ate Che, who has given me their unconditional love and support in all my endeavours.

Table of Contents

1	Introduction	1
1.1	Diesel and Emission Control	1
1.2	Objective	2
2	Soot Particle Transport and Measurement Techniques	5
2.1	Diesel Engine Emissions	6
2.1.1	Diesel Engine Particulate Matter Emissions	6
2.2	Soot Transport and Deposition Models	12
2.2.1	Convection	14
2.2.2	Diffusion	15
2.2.3	Thermophoresis	17
2.2.4	Electrical Mobility	20
2.2.5	Adhesion of Particles	21
2.3	Two-Phase Flow Interaction	22
2.4	Non-Destructive Soot Deposition Measurement	23
2.5	Characterization of Soot Deposition Profiles In Diesel Engine EGR Cooling Devices	24
3	Experimental Facilities and Methodology	27

3.1	Water Cooled Sections	27
3.2	Near Zero Emission Diesel Exhaust Test Facility	35
3.3	Dynamic Neutron Radiography Facility	38
3.4	Image Processing for Determining Deposited Soot Thickness	40
4	Experimental Results	46
4.1	Particulate Matter Mass Concentration and Gas Composition	47
4.2	Rectangular Wall Cooled Section	47
4.2.1	Effect of Diesel Flue Gas Exposure Time on Soot Deposition	50
4.2.2	Effect of Cooling Temperature on Soot Deposition	61
4.3	Cylindrical Wall Cooled Section	67
4.3.1	Effect of Diesel Flue Gas Exposure Time on Soot Deposition	67
4.3.2	Effect of Cooling Temperature on Soot Deposition	77
4.4	Electrical Effects on Soot Deposition	82
4.5	Comparison with Deposition Models	89
4.6	Summary	90
5	Conclusions	95
6	Recommendations for Future Work	98
	Appendices	103
A	Venturi Calibration Curves	104
B	Real-Time Neutron Radiography Images of the Cooled Sections	106
B.1	Rectangular Wall Cooled Section	106
B.2	Cylindrical Wall Cooled Section	111

C Digital Images of Soot Inside the Cylindrical Wall Cooled Section 112

List of Figures

1.1	NO _x and PM emission standards of various governments (Johnson, 2004)	3
2.1	NO _x emission standards (Schulte-Braucks, 2005)	7
2.2	PM emission standards (Schulte-Braucks, 2005)	8
2.3	Typical mass and number concentration adapted from Kittelson (1998)	11
2.4	Typical SEM image of agglomerated soot particles	11
2.5	Relaxation time for unit density particles (Hinds, 1982)	16
2.6	Concept of neutron attenuation from a sooted pipe adapted from Ismail et al. (2004a)	25
3.1	Dimensions of the RWCS	29
3.2	Image of the RWCS	29
3.3	RTNR field of view and analysis region of the RWCS	30
3.4	Dimensions of the CWCS	30
3.5	Image of the CWCS	30
3.6	RTNR field of view and analysis region of the CWCS	31
3.7	Schematic of the CCWCSE	33
3.8	Image of the CCWCSE	33
3.9	RTNR field of view and analysis region of the CCWCSE	34
3.10	Schematic of the NZE-DTF	36

3.11	Cooling water loop	39
3.12	Location of the DNR at the MNR	41
3.13	Schematic of the RNTR	41
3.14	Block diagram of the image analysis process	42
3.15	Raw RNTR image of the RWCS	42
3.16	Normalized image of RWCS with background subtracted	43
4.1	Transient of nominal exhaust Gas PM mass concentration	48
4.2	Transient of nominal exhaust Gas CO and NOx concentration	48
4.3	Nominal Exhaust Gas O ₂ and CO ₂ concentration	49
4.4	Transient of nominal exhaust gas temperature	51
4.5	Transient of nominal coolant temperature	51
4.6	Soot deposition profile of RWCS for 40 °C, 1hr case; δ_s in mm	52
4.7	Nominal RCWS outside wall temperature profile for 40 °C, 1hr case	52
4.8	Soot deposition profile of RWCS for 40 °C, 2hr case; δ_s in mm	53
4.9	Nominal RCWS outside wall temperature profile for 40 °C, 2hr case	53
4.10	Soot deposition profile of RWCS for 40 °C, 3hr case; δ_s in mm	54
4.11	Nominal RCWS outside wall temperature profile for 40 °C, 3hr case	54
4.12	x-axis soot deposition profile of 1hr exposure time and 40 °C coolant temperature at y = 5mm, 50mm and 95mm.	56
4.13	x-axis soot deposition profile of 2hr exposure time and 40 °C coolant temperature at y = 5mm, 50mm and 95mm.	58
4.14	x-axis soot deposition profile of 3hr exposure time and 40 °C coolant temperature at y = 5mm, 50mm and 95mm.	60
4.15	Soot deposition profile of RWCS for 20 °C, 2hr case; δ_s in mm	62
4.16	Nominal RCWS outside wall temperature profile for 20 °C, 2hr case	62

4.17	Soot deposition profile of RWCS for the no coolant, 2hr case; δ_s in mm	63
4.18	Nominal RCWS outside wall temperature profile for no coolant, 2hr case	63
4.19	x-axis soot deposition profile of RWCS for 2hr exposure time and 20 °C coolant temperature at $y = 5\text{mm}$, 50mm and 95mm	64
4.20	x-axis soot deposition profile of RWCS for 2hr exposure time and no coolant at $y = 5\text{mm}$, 50mm and 95mm.	66
4.21	Transient nominal gas temperatures for CWCS	68
4.22	Transient nominal coolant temperatures for CWCS	68
4.23	Soot deposition profile of CWCS for 40 °C, 1hr case; δ_s in mm	70
4.24	Temperature profile of CWCS for 40 °C, 1hr case	71
4.25	Soot deposition profile of CWCS for 40 °C, 2hr case; δ_s in mm	72
4.26	Temperature profile of CWCS for 40 °C, 2hr case	73
4.27	Soot deposition profile of CWCS for 40 °C, 3hr case; δ_s in mm	74
4.28	Temperature profile of CWCS for 40 °C, 3hr case	75
4.29	Cross-sectional soot deposition thickness average after 1hr operation time and 40 °C coolant temperature, CWCS	75
4.30	Cross-sectional soot deposition thickness average after 2hr operation time and 40 °C coolant temperature, CWCS	76
4.31	Cross-sectional soot deposition thickness average after 3hr operation time and 40 °C coolant temperature, CWCS	76
4.32	Soot deposition profile of CWCS for 20 °C, 2hr case; δ_s in mm	78
4.33	Temperature profile of CWCS for 20 °C, 2hr case	79
4.34	Soot deposition profile of CWCS for the no coolant, 2hr case; δ_s in mm	79
4.35	Temperature profile of CWCS for the no coolant, 2hr case	80
4.36	Cross-sectional soot deposition thickness average after 2hr operation time and 20 °C coolant temperature, CWCS	80

4.37	Cross-sectional soot deposition thickness average after 2hr operation time with no coolant condition, CWCS	81
4.38	Time averaged discharge current and voltage characteristics of the CCWCSE for positive and negative polarities for soot free condition .	84
4.39	Soot deposition profile of CCWCSE for the 0kV case; δ_s in mm . . .	85
4.40	Soot deposition profile of CCWCSE for the -3kV case; δ_s in mm . . .	86
4.41	Soot deposition profile of CCWCSE for the +3kV case; δ_s in mm . .	87
4.42	Cross-sectional average of soot deposition profile for 0kV case, CCWCSE	87
4.43	Cross-sectional average of soot deposition profile for -3kV case, CCWCSE	88
4.44	Cross-sectional average of soot deposition profile for +3kV case, CCWCSE	88
4.45	Experimental results compared with modified Chang's model	91
4.46	Mean soot deposition thickness as a function of operation time for RWCS and CWCS	93
4.47	Mean soot deposition thickness as a function of initial inlet coolant temperature for RWCS and CWCS	93
4.48	Mean soot deposition thickness as a function of applied voltage for CCWCSE	94
A.1	Calibration curve of venturi flow meter I as a function of ΔP	104
A.2	Calibration curve of venturi flow meter II as a function of ΔP	105
B.1	Unprocessed RTNR image of the RWCS exposed to diesel exhaust gas for 2 hrs at an initial coolant temperature of 20 degrees celcius, 0 degrees rotation, without water	107
B.2	Unprocessed RTNR image of the RWCS exposed to diesel exhaust gas for 2 hrs at an initial coolant temperature of 20 degrees celcius, 0 degrees rotation, with water	107

B.3	Unprocessed RTNR image of the RWCS exposed to diesel exhaust gas for 2 hrs at an initial coolant temperature of 20 degrees celcius, 30 degrees rotation, without water	108
B.4	Unprocessed RTNR image of the RWCS exposed to diesel exhaust gas for 2 hrs at an initial coolant temperature of 20 degrees celcius, 30 degrees rotation, with water	108
B.5	Unprocessed RTNR image of the RWCS exposed to diesel exhaust gas for 2 hrs at an initial coolant temperature of 20 degrees celcius, 60 degrees rotation, without water	109
B.6	Unprocessed RTNR image of the RWCS exposed to diesel exhaust gas for 2 hrs at an initial coolant temperature of 20 degrees celcius, 60 degrees rotation, with water	109
B.7	Unprocessed RTNR image of the RWCS exposed to diesel exhaust gas for 2 hrs at an initial coolant temperature of 20 degrees celcius, 90 degrees rotation, without water	110
B.8	Unprocessed RTNR image of the RWCS exposed to diesel exhaust gas for 2 hrs at an initial coolant temperature of 20 degrees celcius, 90 degrees rotation, with water	110
B.9	Unprocessed RTNR image of the CWCS exposed to diesel exhaust gas for 2 hrs at an initial coolant temperature of 20 degrees celcius, 0 degrees rotation, without water	111
B.10	Unprocessed RTNR image of the CWCS exposed to diesel exhaust gas for 2 hrs at an initial coolant temperature of 20 degrees celcius, 90 degrees rotation, without water	111

C.1	Digital image of the top portion inside the CWCS gas channel at upstream exposed to diesel exhaust gas for 2 hrs at an initial coolant temperature of 20 degrees celcius	112
C.2	Digital image bottom of the portion inside the CWCS gas channel at upstream exposed to diesel exhaust gas for 2 hrs at an initial coolant temperature of 20 degrees celcius	113
C.3	Digital image of the top portion inside the CWCS gas channel at downstream exposed to diesel exhaust gas for 2 hrs at an initial coolant temperature of 20 degrees celcius	113
C.4	Digital image of the bottom portion inside the CWCS gas channel at downstream exposed to diesel exhaust gas for 2 hrs at an initial coolant temperature of 20 degrees celcius	114

List of Tables

2.1	Typical diesel engine emissions adapted from Adler et al. (1993) . . .	7
2.2	Summary of typical deposition and transport models	13
2.3	Summary of typical thermophoretic deposition studies adapted from Romay et al. (1998)	19
3.1	Lombardini 15LD350 engine characteristics	36
4.1	Experimental parameters implemented in numerical solution	91

Chapter 1

Introduction

1.1 Diesel and Emission Control

There are a large percentage of diesel powered commercial transports currently being utilized on a global scale, these include trucks, freighters and locomotives. There is a large incentive to use diesel engines because of their higher power, low maintenance costs, and more importantly, higher fuel efficiency and approximately 30% lower CO₂ emission levels as compared to gasoline engines. Thus it is often the engine of choice for heavy-duty applications. However, there is a large trade-off with lower CO₂ and higher fuel efficiency in diesel engines, that is, a higher emission of pollutants such as nitrous oxides (NO_x), hydrocarbons (HC), particulate matter (PM), etc. (Schwela and Zali, 1999).

Airborne pollutants, in particular NO_x and PM are of important concern because of their environmental and health impacts. NO_x can have detrimental effects in the respiratory and pulmonary systems (Detels et al., 1991), it is also a pollutant that contributes to the greenhouse effect. Along with NO_x, PM can also have detrimental effects to the respiratory and pulmonary systems which can cause an increase

in mortality (Pope et al., 2002) and is also a contributor to localized city smog. Due to the severe effects of these pollutants to the human health and environment, various governments have implemented restriction levels to these pollutants from transportation vehicles. The current NO_x and PM emission standards for the USA(EPA), the European Union (EU, Japan and Canada are shown in Figure 1.1.

Due to these demanding restrictions on pollutant levels, after-treatment pollution control devices such as; selective reduction catalyst (SCR), used to reduce NO_x levels; electrostatic precipitators (ESP), used to reduce PM levels; diesel particulate filters (DPF), used to reduce PM levels; and engine control pollution control devices such as exhaust gas recirculation (EGR) systems; used to reduce NO_x levels, must be implemented to be able to continue to rely on diesel transport (Adler et al., 1993). These pollution control devices are subjected to PM from the diesel exhaust, thus it is susceptible to PM or soot deposition which can affect the efficiency and performance of these devices (White, 1963; Zhang et al., 2004; Ismail et al., 2004b). Therefore there is a need to understand the mechanisms of soot deposition.

1.2 Objective

The objective of this work is to characterize and evaluate the effect of convection, diffusion, thermophoresis and electric field on soot deposition in a turbulent flow in three devices; a rectangular wall cooled section, a cylindrical wall cooled section and a electrostatic wall cooled section using a Real-Time Neutron Radiography (RTNR) technique for determining soot deposition thicknesses inside the devices. The time transient of soot deposition will also be investigated as part of this study to determine the rate of deposition with respect to time and compare with the rate of deposition with respect to wall cooling temperature. The experiments will be performed in the

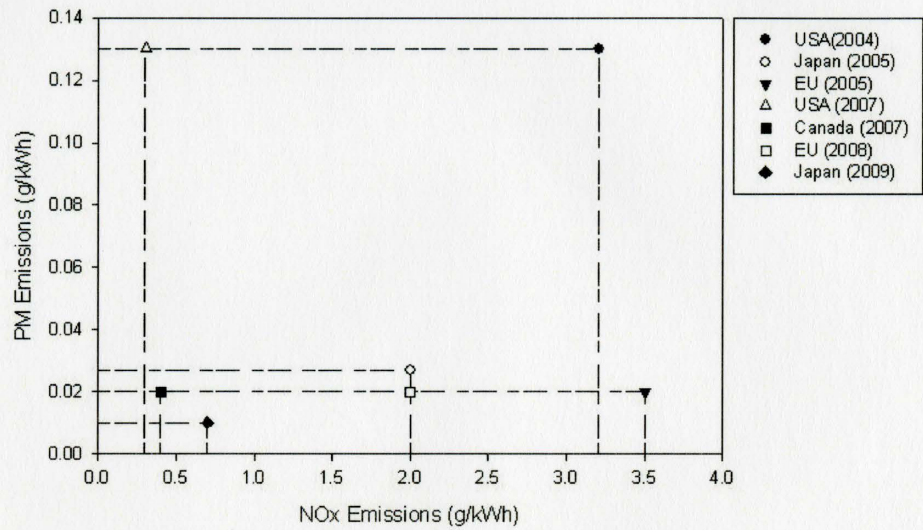


Figure 1.1: NOx and PM emission standards of various governments (Johnson, 2004)

Near-Zero Emission Diesel Exhaust Test Facility using a 2.4kW single cylinder diesel engine and the Dynamic Neutron Radiography (DNR) facility for RTNR.

This thesis contains six chapters including; an introduction; a review of the available literature in the areas of diesel emissions and composition, characteristics of diesel particulate matter and deposition, soot transport models and two phase flow interaction in Chapter 2; the experimental facilities and methodologies used in this investigation in Chapter 3; the experimental results obtained from this investigation in Chapter 4; the conclusions in Chapter 5; and finally recommendations for future work in Chapter 6.

Chapter 2

Soot Particle Transport and Measurement Techniques

In this chapter a literature review on the diesel engine emissions, particulate matter, current investigations in diesel engine exhaust soot transport and soot deposition thickness measurement techniques was given. The review will begin with typical diesel exhaust emission characteristics, in particular, size distribution and concentration of particulate matter for direct injection (DI) diesel engines. The following section will discuss the characteristics of diesel engine exhaust PM, its composition and mechanisms of formation. A critical review of soot transport and deposition models, in particular, convection, diffusion, thermophoresis and electric mobility models as well as a review on two-phase, gas-solid transport of diesel engine exhaust PM and its effect on deposition and entrainment will be discussed. Finally, a review of a non-destructive Real-Time Neutron Radiography (RTNR) technique for measuring deposited soot layers with a discussion on previous work on soot depositions in an exhaust gas recirculation (EGR) cooling device be presented in the chapter.

2.1 Diesel Engine Emissions

Diesel engine emissions consists of high concentrations of unburned hydrocarbons (HC), volatile organic compounds (VOC), particulate matter (PM), sulphur oxides (SO_x) and nitrogen oxides (NO_x). NO_x is defined as a combination of nitrogen monoxide (NO) and nitrogen dioxide (NO₂). Table 2.1 shows these diesel engine emissions and their typical concentrations at idle and maximum output. Various governments such as Canada, The United States, The European Union and Japan have been regulating and setting lower emission standards over time, with NO_x levels as shown in Figure 2.1 and PM levels as shown in Figure 2.2. Most of these emission standards target lower NO_x and PM levels, thus requiring automotive companies to implement engine control and after-treatment pollution control devices. An example of a NO_x controlling device is EGR system and cooling device which cools and recirculates the diesel exhaust back in to the main air intake to dilute the oxygen in the combustion chamber (Zheng et al., 2004; Abd-Alla, 2002). A selective reduction catalyst (SCR) could also be used to react with NO_x and reduce it to form water vapour (H₂O) and nitrogen gas (N₂) (Servati et al., 2005), this device is used in conjunction with a diesel particulate filter (DPF) to remove PM from the diesel exhaust gas. Another method used to reduce PM emissions is by an electrostatic precipitator to induce an electric charge on the PM particles and are electrostatically deposited onto the device walls (Zukeran et al., 1999).

2.1.1 Diesel Engine Particulate Matter Emissions

Over longer operation times, pollution control devices and engine components can accumulate a layer of soot that can decrease their performance (White, 1963; Zhang et al., 2004; Ismail et al., 2004b) and can also cause corrosive damage due to

Table 2.1: Typical diesel engine emissions adapted from Adler et al. (1993)

Exhaust Gas Component	Units	At Idle	At Maximum Output
Nitrous oxides(NOx)	ppm	50 - 250	600 - 2500
Hydrocarbons	ppm C ₁	50 - 500	150
Carbon monoxide	ppm	100 - 450	350 - 2000
Carbon dioxide	Vol. %	<3.5	12 - 16
Water vapour	Vol. %	2 - 4	<1
Oxygen	Vol. %	18	2 - 12
Nitrogen, etc.	Vol. %	residual	residual
Soot/PM	mg/m ²	≈20	≈200
Exhaust Gas Temperature	°C	100 - 200	550 - 750

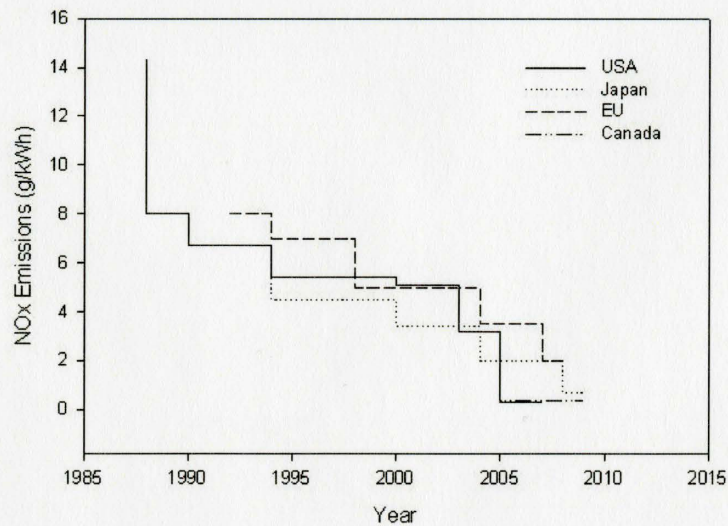


Figure 2.1: NOx emission standards (Schulte-Braucks, 2005)

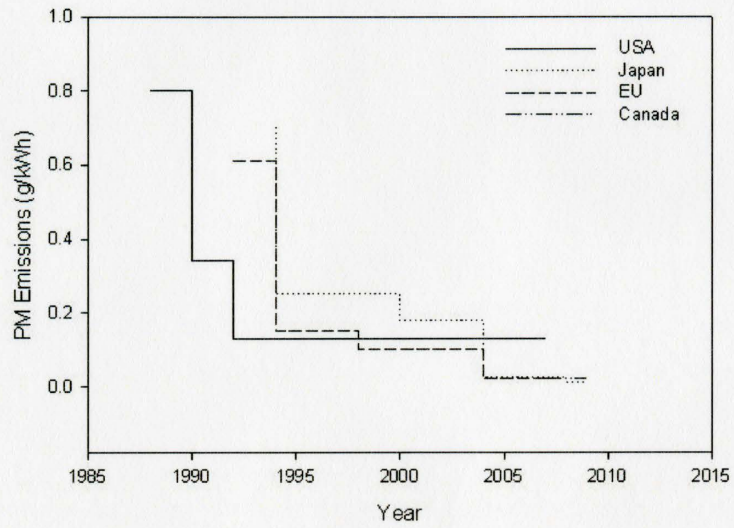


Figure 2.2: PM emission standards (Schulte-Braucks, 2005)

the deposited soot layer (Ornektekin, 1998), mostly due to the component and characteristics of PM. Diesel engine exhaust PM are a combination of highly agglomerated solid carbon and ash, as well as volatile organic and sulphur compounds (Kittelson, 1998) and are by-products of incomplete fuel combustion due to the non-uniform fuel air mixture within the combustion chamber (Adler et al., 1993). They are formed by the nucleation, coagulation and condensation of inorganic and organic compounds in the diesel exhaust (Kim et al., 2002).

Diesel engine particulate matter has a tri-modal distribution and are classified into three different modes; nuclei, accumulation and course mode. The number and mass distribution of typical diesel engine exhaust are shown in Figure 2.3. The nuclei mode consists of particles with diameters ranging from 0.005 to 0.05 μm and dominates in terms of number (>90%) but smaller in terms of mass (1 - 20%). It consists mainly of organic matter and sulphur compounds and also of volatile particles formed by nucleation. It can also contain some solid carbon and inorganic compounds (Desantes et al., 2005).

Nucleation is defined as the onset of phase transition, in this case, from a gas to a solid. The mechanisms of nucleation can be classified as homogeneous and heterogeneous. Homogeneous nucleation occurs when no interface is present, therefore a given volume of a nucleus must free enough energy to form a large enough surface such that it allows a nuclei to be viable. Heterogeneous nucleation relies on the energy that is released from the partial breakdown of the interface surface to allow a nuclei to be viable. The accumulation mode has a diameter in the range of 0.05 to 1.0 μm and is mainly comprised of carbon agglomerates and volatile matter adsorbed on the surface. It has a significantly lower number distribution, but has a higher mass concentration (60 to 90%).

The course mode, its particle size is greater than 1 μm and accounts for 5 -

20% of the total particle mass distribution. Typical Scanning Electron Microscopy (SEM) images of agglomerated soot particles is shown in Figure 2.4

There are many engine parameters that affect the characteristics of diesel engine PM. In the study by Ning et al. (2004), it was found that cooling the exhaust gas, such in the case of EGR cooling, can affect mass concentration, composition, number distribution and number-average diameter of particulate. Once the exhaust gas was cooled, the mass concentration increased, the mean of the particulate number distribution shifted towards larger particles and the total number of particles also decreased. The main mechanisms that are believed to have led to the changes were nucleation and condensation of VOCs and HC's as well as coagulation of particles. It was also observed that PM number density increased with increasing engine load (Ewing et al., 2004). In the study by Desantes et al. (2005), it was observed that increasing exhaust gas recirculation also shifts the particle number from the nuclei mode to the accumulation mode as shown in Figure 2.3. It can be observed that engine load and exhaust gas cooling can have a significant effect on PM characteristics and distribution.

Combustion particles has been known for some time to be electrically charged, Wesborg et al. (1973) observed that particles from low pressure flames could be deflected using an external electric field. It has been observed that individual diesel engine particulate matter have a charge ranging from ± 5 elementary charges, and as the charge increased, the mean particle size increased, however particle concentration decreased (Maricq, 2006). It has been also observed that 88% of the total PM that is charged, and have an equal number distribution between positive and negative charges (Kittelson et al., 1991). Electrically charged soot can play a significant role in deposition and adhesion as discussed in section 2.2.

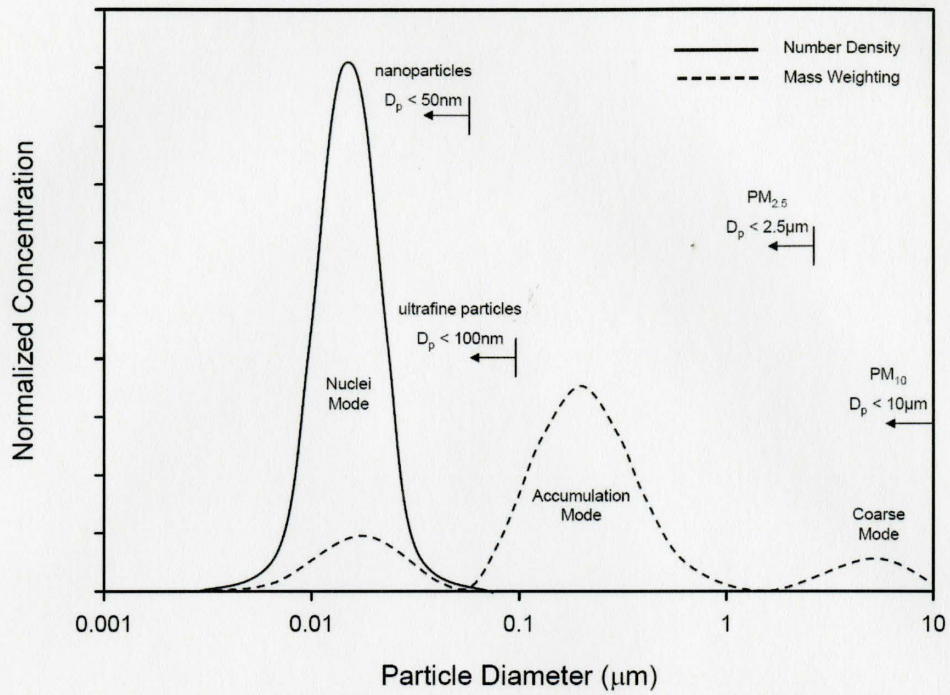


Figure 2.3: Typical mass and number concentration adapted from Kittelson (1998)

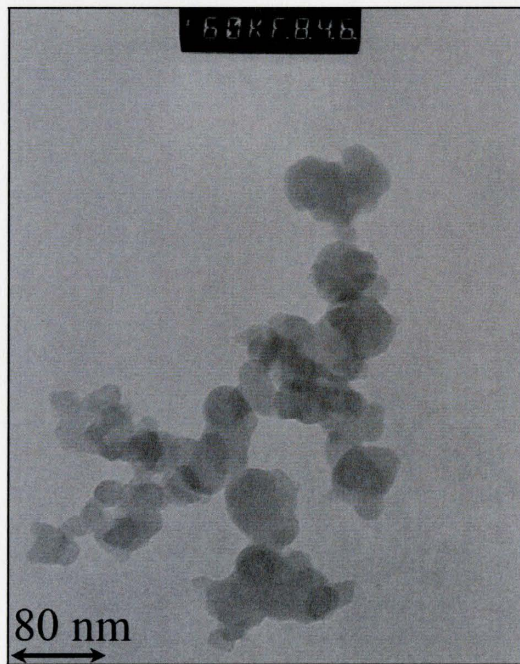


Figure 2.4: Typical SEM image of agglomerated soot particles

2.2 Soot Transport and Deposition Models

There are several mechanisms that govern the transport and deposition of soot. The transport equation under diluted soot in gas flow (Beuthe and Chang, 1995) show that the governing equations of the transport and deposition of diesel exhaust soot as follows:

$$\nabla \cdot J_s = -\frac{d[N_s]}{dt} + source - sink \quad (2.1)$$

, and

$$\vec{J}_s = N_s \overline{u_g} \pm \mu_{cs} N_{cs} \overline{E} - D_s \nabla N_s - G_s N_s \nabla T_g \quad (2.2)$$

, where J_s is the particle flux density and defines the number density of particles that pass through a control volume, N_s and N_{cs} are the particle number density of total soot and charged soot particles respectively, u_g is the gas velocity, μ_{cs} is the electric mobility of the charged soot, E is the applied electric field, D_s is the diffusion coefficient, G_s is the thermophoretic parameter and T_g is the gas temperature. The continuity equation can be broken down into four terms; the first one is the convective term; the second, the electric mobility term; the third being the diffusion term; and finally the last term, the thermophoretic term. Each term defines a mechanism of deposition and transport and are discussed in the following sections. The gravitational term has been neglected since gravitational effects for dilution conditions only have significant effects for particle diameter greater than $10\mu\text{m}$ (White, 1963). A summary of typical deposition models are shown in Table 2.2

Table 2.2: Summary of typical deposition and transport models

Particle Transport System	Mechanisms	Model
Thermophoresis of Small Aerosols ($d < \lambda$) (Waldmann and Schmitt, 1966)	Thermophoresis	$\vec{J} = -N_p \frac{-0.55\eta_g \nabla T_g}{\rho_g T_g}$
Thermophoresis of Large Aerosols ($d > \lambda$) (Hinds, 1982)	Thermophoresis	$\vec{J} = -N_p \frac{-3C_c \eta_g \nabla T_g}{e \rho_g T_g}$ $H = \left(\frac{1}{1+6\lambda/d_p} \right) \left(\frac{k_a/k_p + 4.4\lambda/d_p}{1+2k_a/k_p + 8.8\lambda/d_p} \right)$
Particle Deposition in a Heated Boundary Layer (Talbot et al., 1980)	Thermophoresis	$\vec{J} = -N_p K_{th} \frac{\nu_g}{T_g} \nabla T_g, K_{th} = 2C_s \frac{(k_g/k_p + C_t K n) C_c}{(1+3C_m K n)(1+2k_g/k_p + 2C_t K n)}$
Aerosol in Laminar Flow in Cylindrical Channels (Tan and Hsu, 1971)	Convection-Diffusion	$\vec{J} = N_p \bar{u}_g - D_p \nabla N_p, D_p = \frac{\kappa T_g}{3\pi \mu_g d_p} C_c$
Aerosol Flows in Rectangular Channels (Taulbee and Yu, 1975)	Convection-Diffusion, Sedimentation	$\left(V + \frac{2\sigma_x}{Pe} \right) \frac{\partial n}{\partial \xi} + \left(\frac{\sigma_y}{2} \right)^2 n = \frac{\partial^2 n}{\partial \eta^2}, V = \frac{3}{2}(1 - \eta^2)$
Poiseuille Flow of Aerosols in Rectangular Tubes (Ingham, 1975)	Convection-Diffusion, Sedimentation	$D \frac{\partial^2 n}{\partial x^2} = V(x) \frac{\partial n}{\partial z} - \nu_g \frac{\partial n}{\partial x}, V(x) = \frac{3Q}{4h} \left(1 - \frac{x^2}{h^2} \right)$
Charged Particles in Aerosol Flow in an Unbounded Region (Beuthe and Chang, 1995)	Convection-Diffusion, Thermophoresis, Electric Field	$J_p = N_p \bar{u}_g \pm \mu_{cp} N_{cp} \bar{E} - D_p \nabla N_p - G_p N_p \nabla T_g$
Electrostatic Charging of Neutral Dust (Brocilo et al., 2001)	Convection-Diffusion Electrostatic	$\bar{u}_g \cdot \vec{i} - \mu_i \nabla \cdot (N_i \bar{E}) - D_i \nabla N_i = -k N_i N_d$

2.2.1 Convection

Particles convected along a gas flow u_g can be defined by its mechanical terminal velocity, influenced by constant and varying forces including drag and curvilinear motion. The drag force of a moving particle in the Stokes region ($Re < 1$) given by (Hinds, 1982)

$$F_D = \frac{3\pi\eta_g V_s d_p}{C_c} \quad (2.3)$$

, where η_g is the gas viscosity, V_s is the relative particle velocity to the gas, d_p is the particle diameter and C_c is the Cunningham slip correction factor given by

$$C_c = 1 + Kn \cdot [1.257 + 0.4\exp(-1.1/Kn)] \quad (2.4)$$

, where Kn is the Knudsen Number. For larger particles, a different drag force is defined

$$F_D = C_D \frac{\pi}{8} \rho_g d_p^2 V_s^2 \quad (2.5)$$

, where ρ_g is the gas density, V_s is the relative particle velocity to the gas and C_D is the drag coefficient. In the Newton's Law regime ($Re > 1000$) the drag coefficient is given by (Hinds, 1982)

$$C_D \simeq 0.44 \quad (2.6)$$

In unsteady or accelerating flows, a relaxation or response time τ defines the

time a particle can adjust to a new velocity

$$\tau = mB = \frac{\rho_p d_p^2 C_c}{18\eta_g} \quad (2.7)$$

, where ρ_p is the particle density. The terminal velocity of a particle under the influence of any force is the product of its mechanical mobility, B defined as

$$B = \frac{V}{F_D} = \frac{1}{3\pi\eta_g d_p} \quad (2.8)$$

, and an external force, F is given by

$$V_{TF} = BF = \tau \frac{F}{m} \quad (2.9)$$

in terms of relaxation time (Hinds, 1982). Therefore, larger particles have a slower response time when following fluid streamlines whereas small particles tend to follow streamlines with a fast response time. Using equations 2.7, 2.8 and 2.9 the relaxation time for unit density particles is shown in Figure 2.5

2.2.2 Diffusion

Diffusion in particles is defined by an irregular wiggling motion in still air called Brownian motion. Diffusion forces occur in a number density gradient, and are transported from a location of high number density to a lower number density, due to collisions (Hinds, 1982). The diffusion coefficient governs and dictates the flux of particles J_p through a control volume, this equation is called Fick's first law of diffusion.

$$J_p = -D_p \nabla N_p \quad (2.10)$$

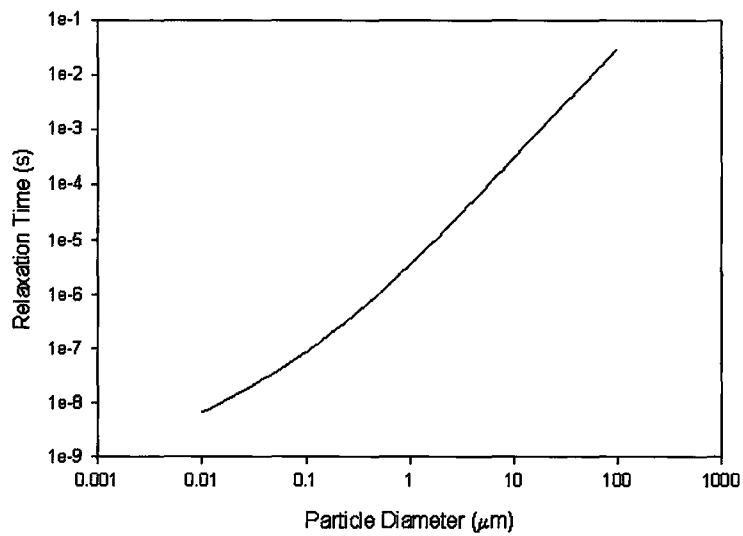


Figure 2.5: Relaxation time for unit density particles (Hinds, 1982)

, where the diffusion coefficient D_p is given by

$$D_p = \frac{kT_g C_c}{3\pi\eta_g d_p} \quad (2.11)$$

Equation 2.11 is called the Stokes-Einstein equation for particle diffusivity, where k is Boltzmann's Constant.

2.2.3 Thermophoresis

When a temperature gradient exists in a fluid, the particles in the fluid experiences a force from the higher temperature to the lower one, this is called the thermophoretic force. For small particles ($d < \lambda$) the thermal force on a particle of diameter d is given by (Hinds, 1982)

$$F_{th} = \frac{-P_g \lambda d^2 \nabla T_g}{T_g} \quad (2.12)$$

, which results in the velocity of thermophoresis by Waldmann and Schmitt (1966), where p is the gas pressure and λ is the particle mean free path.

$$V_{th} = \frac{-0.55\eta_g \nabla T_g}{\rho_g T_g} \quad (2.13)$$

The thermophoretic particle motion can be governed by the thermophoretic velocity, u_{th} , given by (Talbot et al., 1980)

$$u_{th} = -K_{th} \frac{\nu_g}{T_g} \nabla T_g \quad (2.14)$$

, where ν_g is the kinematic viscosity and K_{th} is the thermophoresis coefficient given

by (Talbot et al., 1980)

$$K_{th} = 2C_s \frac{(k_g/k_p + C_t Kn) C_c}{(1 + 3C_m Kn)(1 + 2k_g/k_p + 2C_t Kn)} \quad (2.15)$$

, where C_s is the thermal creep coefficient = 1.147, C_t is the temperature jump coefficient = 2.20 and C_m is the velocity jump coefficient = 1.146. This parameter was experimentally compared by Nishio et al. (1974) and found to be within reasonable agreement.

The thermophoresis parameter, G_p is related to the thermophoresis coefficient by

$$G_p = \frac{-\nu_g K_{th}}{T_g} \quad (2.16)$$

Several studies have been conducted for thermophoresis and deposition efficiency in both turbulent and laminar flow regimes. Thermophoretic studies are summarized in Table 2.3. Nishio et al. (1974) observed that fractional deposition increased with an increase temperature gradient with the pipe wall and exhaust gas, however, thermophoretic deposition decreased at an extremely high Reynolds number ($Re \approx 20000$) due to the formation of eddy currents, overcoming adhesion forces. Recently Messerer et al. (2003)) investigated the thermophoretic deposition of diesel soot particulate matter under laminar flow and observed that at low Reynolds numbers diffusion was the dominant mechanism, however was enhanced by the thermophoretic mechanism. Zhang et al. (2004)) investigated soot deposition as a function of mass flow rate and cooling temperature, it was observed that there was a decrease in soot deposition as the coolant temperature increased. Also, as mass flow rate increased, there was an increase in soot deposition.

Table 2.3: Summary of typical thermophoretic deposition studies adapted from Romay et al. (1998)

Investigators	Efficiency Model
Byers and Calvert (1969)	$\eta_L = 1 - \exp \left\{ -\frac{\rho C_p f Re_D K_{th} \nu (T_e - T_w)}{3 D h T} \left[1 - \exp \left(\frac{-4 h L}{u_m \rho C_p D} \right) \right] \right\}$
Nishio et al. (1974)	$\eta_L = 1 - \exp \left\{ -\frac{\rho C_p K_{th} \nu (T_e - T_w)}{k_g T} \left[1 - \exp \left(\frac{-4 h L}{u_m \rho C_p D} \right) \right] \right\}$
Batchelor and Shen (1985)	$\eta_\infty = Pr K_{th} \left[-\frac{T_e - T_w}{T_e} \right] \left[1 + (1 - Pr K_{th}) \left(-\frac{T_e - T_w}{T_e} \right) \right]$
Stratmann et al. (1994)	$\eta_\infty = 1 - \exp \left[-0.845 \left(\frac{Pr K_{th} + 0.025}{t_w / (T_e - T_w) + 0.28} \right)^{-0.932} \right]$
Romay et al. (1998)	$\eta_L = 1 - \left(-\frac{T_w + (T_e - T_w) \exp(-\rho Q C_p)}{T_e} \right)^{Pr K_{th}}$

2.2.4 Electrical Mobility

As discussed in section 2.1, soot may be electrically charged, it was also discussed that there may be an even distribution between positive and negative charges. The force on a charged particle q in a electric field E is defined by (Hinds, 1982)

$$F = qE \quad (2.17)$$

, where

$$q = ne \quad (2.18)$$

and where n is the number of charges and e is the elementary charge 1.602×10^{-19} Coulombs.

The electric mobility of a charged particle when placed in an electric field outside the Stokes region (i.e. $Re > 1000$), can overcome the forces of gravity and can be obtained by equating equations 2.17, 2.18 and Newton's resistance equation.

$$neE = C_D \frac{\pi}{8} \rho_g d_p^2 V_{TE}^2 \quad (2.19)$$

, where V_{TE} is the terminal electrostatic velocity. Solving for C_D gives

$$C_D = \frac{8neE}{\pi \rho_g d_p^2 V_{TE}^2} \quad (2.20)$$

, and multiplying both sides by Re^2 then yields

$$C_D Re^2 = \frac{8neE \rho_g}{\pi \eta^2} \quad (2.21)$$

, where Re is the Reynolds number. The terminal electrostatic velocity can be de-

terminated from the value of $C_D Re^2$ by graphical or tabular procedures (Hinds, 1982).

The collection efficiency, η_e , can be determined by

$$\eta_e = 1 - \exp\left(\frac{-V_{TE}A_c}{Q_g}\right) \quad (2.22)$$

, where A_c is the area of the collection surface and Q_g is the volume flow rate of the exhaust gas.

2.2.5 Adhesion of Particles

Once a soot particle has been attracted to the bounding wall and makes contact, there are several forces that causes the soot to adhere to the surface and remain deposited, mainly; Van der Waals force, Electrostatic force and surface tension of adsorbed films on both the wall surface and particle. These forces can be affected by the soot material, shape, size, relative humidity, temperature duration of contact and initial contact velocity (Hinds, 1982).

Van der Waal's forces arise from the random movement of electrons that cause momentary areas of charges called dipoles and can induce a dipole on a neighbouring particle or material if close enough. As soon as a dipole is induced, the particles have an attractive force between a sphere of diameter d_1 at a distance r as defined by (Whitby and Liu, 1966)

$$F = \frac{\pi^2 q_0^2 \lambda}{12r^2} d_1 \quad (2.23)$$

, where F is Van der Waal's force, q_0 is the number of atoms per cm^2 and λ is the Van der Waal's constant for attraction.

Electrostatic forces arises when the pre-charged soot mentioned in section 2.2.4 is deposited onto a wall and creates a local electric field. This local electric field then

attracts other pre-charged soot and once the entrained particle makes contact with the deposited soot layer, will adhere due to the electrostatic force. The electrostatic force is defined by (Whitby and Liu, 1966).

$$F = \frac{\epsilon q^2}{h^2} \quad (2.24)$$

, where ϵ is the permittivity of the dielectric medium and h is the distance of the particle from the dielectric medium.

Finally, forces due to surface tension from adsorbed film on the particle and condensed fluid on the wall surface are mainly dependent on humidity. For relative humidities $>90\%$ the adhering force is defined by (Hinds, 1982)

$$F = 4\pi\gamma r \quad (2.25)$$

, where γ is the surface tension of the liquid.

2.3 Two-Phase Flow Interaction

Diesel engine exhaust is considered a two-phase, gas-solid flow. There are two classification of gas-solid flows; a dense or a dilute flow (Soo, 1967). A dense flow considers a particle to particle interaction where as a dilute flow relies more on particle to gas interaction. The two phase flow interaction parameter $\sum_{2\phi}$ (Chang, 2003) determines whether a gas-solid flow is in the dense regime if $\sum_{2\phi}$ is greater than 1, or in the dilute regime otherwise as shown in equation 2.26.

$$\sum_{2\phi} = \frac{K_s N_s d_{p,i}}{\rho_g u_{g,i}} \quad (2.26)$$

, where K_s is the Stokes interfacial drag coefficient, N_s is the soot number density, $d_{p,i}$ is the particle diameter at the inlet, ρ_g is the gas density and $u_{g,i}$ is the gas velocity at the inlet.

There have been several studies involving the modeling of dense and dilute flows. It was observed by Soo (1967) and more detail by Keonigsdorff and Werther (1995) that a circulating fluidized bed, an example of a gas-solid flow can have both a dilute flow in the upper zone of the channel and dense flow driven by gravity. It was observed that particle to particle collisions influenced particle dispersion and that there exists a intensively coupled heat and mass transfer between the two flows. Mason and Levy (2001) developed a two layer model, with a dilute flow in the upper zone and dense flow in the lower one, to simulate fine powder flow in a horizontal pipe, with a mean particle diameter of $14 \mu\text{m}$. From their results they obtained good quantitative agreement of pressure gradients with experimental and numerical values in fully developed flows in pipes. It was also observed that as mean flow velocity increased, the depth of the dense layer decreased.

2.4 Non-Destructive Soot Deposition Measurement

There are many ways to measure deposited soot, however, few are non-destructive methods (i.e. techniques that do not disturb the deposited soot layer) that are applicable for soot deposition measurement. Focusing on the non-destructive techniques, the electrical impedance and optical technique require non-electrically conductive pipes and powders with a significant degree of reflectivity in a partially conductive pipe or chamber (Harvel and Chang, 1995). The diode laser transmittance method are only limited to circular pipes or chamber that require a transparent window for the laser to transmit through (Tree and Dec, 2001). There is also a pulse-echo ultrasound

technique by Chang and Morola (1990) however, can only function when the object of interest is in a liquid medium. Neutron radiography has been used to examine the distribution of neutrons when attenuated by a material, for example, the investigation by Ismail et al. (2004a) focused on real-time attenuation of neutrons in this case, the material was a combination of hydrocarbons from the deposited soot and aluminium from the chamber shown in Figure 2.6. The layers could be approximated by (Duderstadt and Hamilton, 1996)

$$\frac{I_s(x, z, \theta)}{I_o} = B\mu_m B\mu_s \exp([-2\mu_s\delta_s(x, z, \theta) - 2\mu_m\delta_m(x, z, \theta)]) \quad (2.27)$$

, where I_s is the attenuated neutrons from the soot, I_o is the neutron beam, μ_m and μ_s are the attenuation coefficient for the metal and the soot respectively and δ_m and δ_s are the thickness for the metal and soot respectively. The attenuated neutrons was then projected on a lithium doped screen which converts the neutrons into photons and is captured by a CCD camera to be analyzed by solving for δ_s in equation 2.27. It was successful at measuring soot layers in the μm range with an accuracy of 16% compared with direct destructive measurements. It was observed to be a viable method for non-destructively measuring soot layers inside an aluminium chamber. Khaial et al. (2006) improved on this technique to achieve higher neutron flux resulting in greater resolution and accuracy in soot thickness measurement.

2.5 Characterization of Soot Deposition Profiles In Diesel Engine EGR Cooling Devices

An investigation by Ismail et al. (2004b) was conducted to characterize soot deposition profiles of EGR cooling devices in diesel engine exhaust. The deposition of

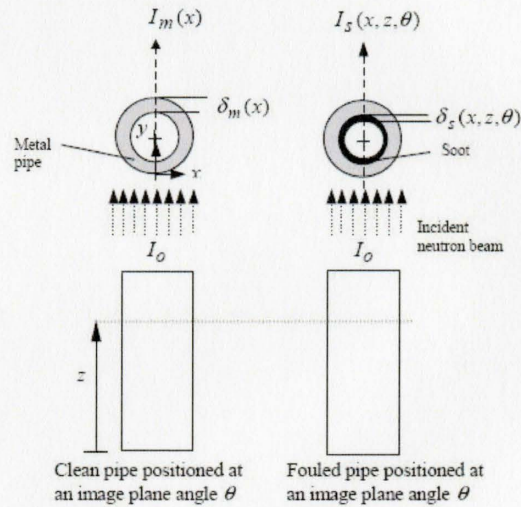


Figure 2.6: Concept of neutron attenuation from a sooted pipe adapted from Ismail et al. (2004a)

soot inside an EGR was measured using destructive and non-destructive techniques, this included a Real-Time Neutron Radiography technique mentioned in section 2.4. Their study involved a 2.4kW single cylinder engine, operated at 2.4 kW, as a source for their diesel exhaust gas. They used a single and three tube cooling devices with each tube of inner-diameter of 6.2mm and 4.1mm, respectively, and a length of 205mm connected to an expansion header with an expansion angle of 60 or 45 degree angles. The mass flow rate was controlled at 0.8 and 2.8 kg/h for the single tube EGR and a constant 6 kg/h for the three tube EGR, resulting in a Reynolds number of 2000, 7000 and 8000 respectively. The upstream temperatures ranging from 118 to 210°C depending on the mass flow rate. The operating times for both the single tube and three tube devices ranged from 1 to 5hrs, with a closed loop cooling system supplying a water coolant of 25 °C at a flow rate of 6 L/min to the tubes.

Ismail et al. (2004b) concluded that the rate of soot deposition was faster for a turbulent flow compared to a laminar flow. It was observed that the soot deposition thickness was highest at the entrance region in the first 13% of the entire length of the device for all the cases, the thicker deposition at the entrance extended further downstream for the laminar case compared to the turbulent case after an operating time of 5hrs. It was explained that the laminar flow has a longer developing region. A wavy pattern in the soot deposition had also developed as operating time approached 5hrs in most of the tube cases. When investigating the effects of the inlet headers of 60 and 45 degrees, it was observed that as the expansion header decreased, the less evenly distributed the soot was within the tubes (i.e. more soot was deposited in the central tube) particularly in the three tube case.

Chapter 3

Experimental Facilities and Methodology

The objective of the present investigation was to study the soot deposition in water cooled rectangular and cylindrical diesel engine exhaust sections. This chapter will discuss the experimental facilities and methodology used in the present study; which includes a diesel engine test facility, thermal imaging system and the Real-Time Neutron Radiography technique.

3.1 Water Cooled Sections

A series of experiments were performed to analyze soot deposition as a function of time, coolant temperature and applied electric field on two exhaust section geometries; a rectangular and cylindrical wall cooled section as shown in Figures 3.1 and 3.4 respectively, a physical image of the actual sections are shown in Figures 3.2 and 3.5 The material of both sections are made of aluminum for neutron radiography purposes explained in section 3.3. The main region of interest in both the rectangular

and cylindrical water cooled sections is the cooled portion of the devices as shown in Figures 3.3 and 3.6.

In the rectangular wall cooled section (RWCS), the gas flow channel has an inner width of 100mm, an inner height of 10mm and a length of 250mm, the design of the section length was limited by the field of view of the Real-Time Neutron Radiography (RTNR) system as explained in section 3.3. The gas flow channel is sandwiched symmetrically by two independent cooling channels of the same dimensions with two coolant inlet/outlet tube shaped ports of size 9.5mm (3/8") ID located at the upstream and downstream opposite of each other. The two cooling channels are connected to a parallel water cooling loop (as discussed in section 3.2) in a co-current flow (i.e. coolant flow is the same direction as exhaust gas flow). These cooling channels provide control of the gas channel wall temperature. The end of the cooling section is attached to the main gas line via a non-removable reducer to a 28.6mm (9/8") ID tube.

In the cylindrical wall cooled section (CWCS), the gas channel has an inner diameter of 28.6mm (9/8") and a length of 300mm, where, the design of the section length was limited by the field of view of the Real-Time Neutron Radiography system as explained in section 3.3. The outside of the gas channel is coaxially surrounded by a water jacket with a size of 47.6mm (1 7/8") ID with two coolant inlet/outlet tube shaped ports of size 9.5mm (3/8") ID located at the upstream and downstream opposite of each other. The two cooling channels are supplied by a parallel water cooling loop as discussed in section 3.2 in a co-current flow, to provide control of the gas channel wall temperature. The CWCS is a straight tube with no transition or reducer from the non-cooled to the cooled region.

For the study of electric field, the CWCS was modified to accommodate a 0.5mm tungsten wire electrode placed coaxially at the centre of the cylinder. The

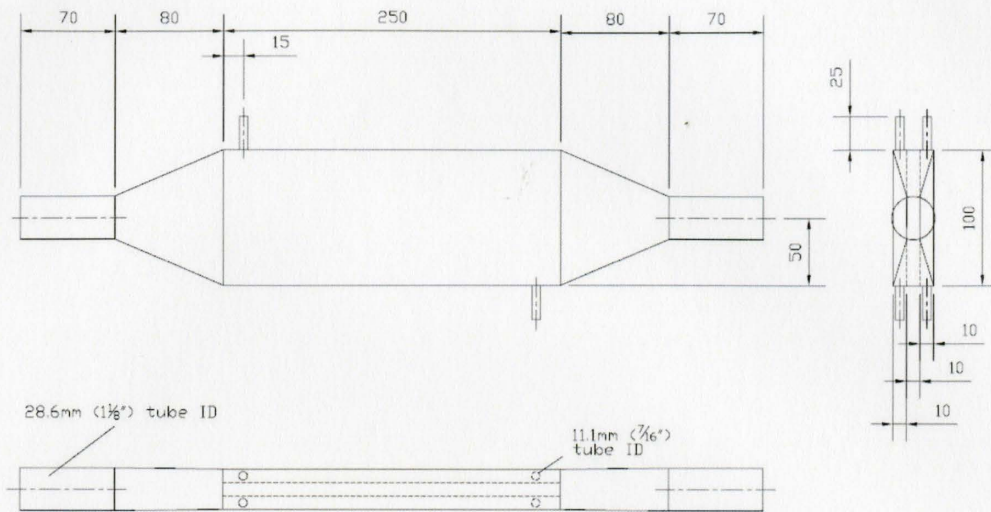


Figure 3.1: Dimensions of the RWCS

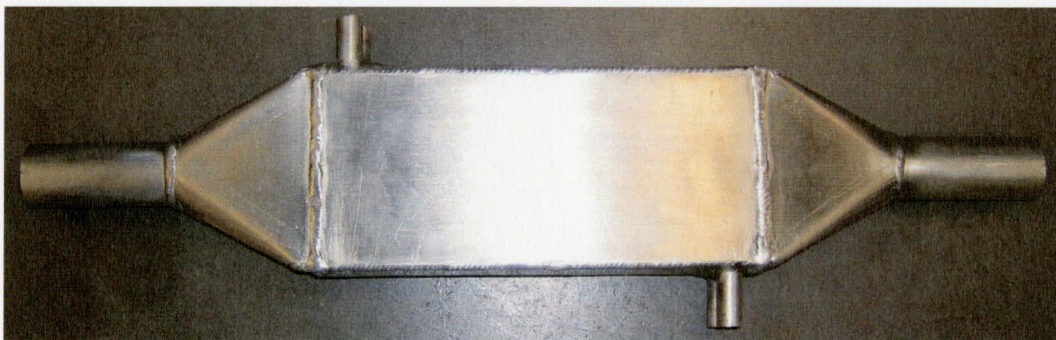


Figure 3.2: Image of the RWCS

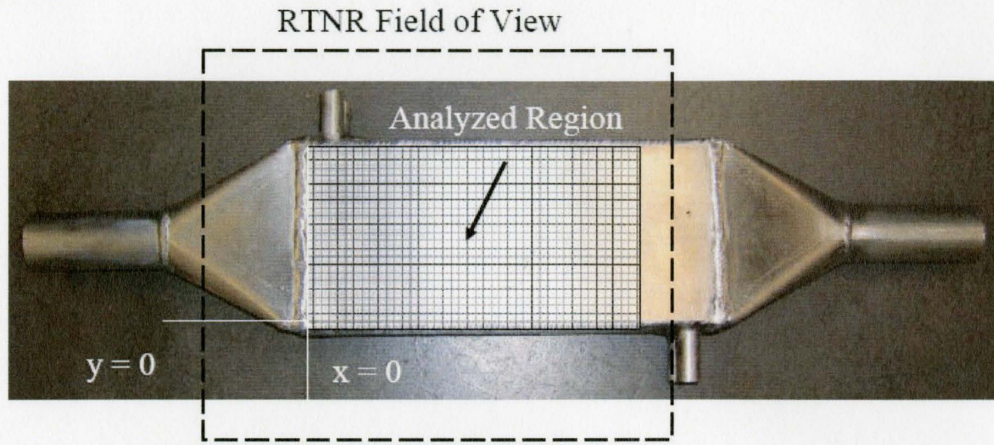


Figure 3.3: RTNR field of view and analysis region of the RWCS

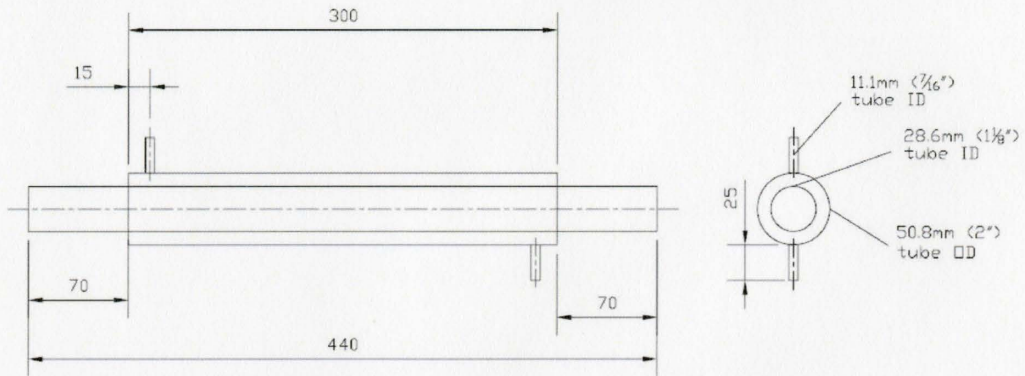


Figure 3.4: Dimensions of the CWCS



Figure 3.5: Image of the CWCS

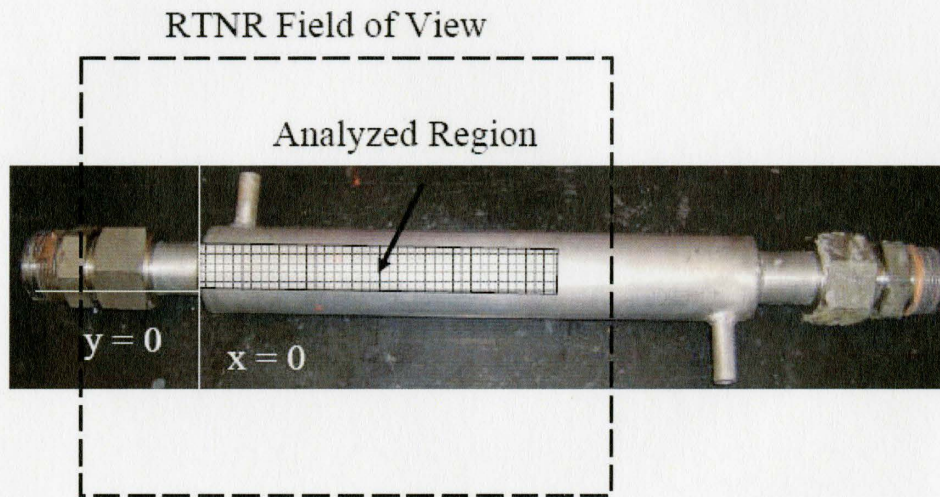


Figure 3.6: RTNR field of view and analysis region of the CWCS

tungsten rod was connected to the GLASSMAN high voltage power supply and the body of the CWCS was grounded such that the gas flow could be subjected to an applied electric field. A schematic of the modified cylindrical wall cooled section (CCWCSE) is shown in Figure 3.7. A physical image and analysis region of the CCWCSE as shown in Figures 3.8 and 3.9 respectively.

Several flow parameters were measured in the cooled sections as follows; upstream and downstream exhaust gas temperature, inlet and outlet of the cooling temperature, upstream soot mass concentration and gas composition. The upstream and downstream exhaust gas temperatures were measured by two T-type Omega thermocouples located 220mm away from cooled section inlet and exit respectively. The inlet and exit coolant temperature was measured at the inlet and exit ports of the cooling channel using two T-type thermocouples at each port. The voltage from the thermocouples were acquired using a National Instruments (NI SCXI-1112) thermocouple board and the signal was processed and recorded onto memory using LabView 9.

The temperature distribution of the outer cooling channel walls was measured by a FLIR ThermaCam SC3000 thermal imaging system for each experiment. Outer wall temperature distributions of the cooled sections were taken at 15 minute intervals to approximate the gas-coolant boundary wall. The cooled sections were coated with an oil based paint which yielded an emissivity of 0.94. The ThermaCam SC3000 has a range of -20 to 1500 °C and an accuracy of 1 °C for temperatures up to 150 °C and 2 °C for temperatures above 150 °C.

The upstream soot mass concentration was measured using the HAZ-DUST III real-time optical particle counter in a sampling chamber. The HAZ-DUST III has an internal pump that takes a sample of exhaust gas from the main gas stream and uses the principle of near-forward light scattering of infrared radiation to measure the concentration of the soot mass in mg/m^3 . The particle size range of the HAZ-DUST

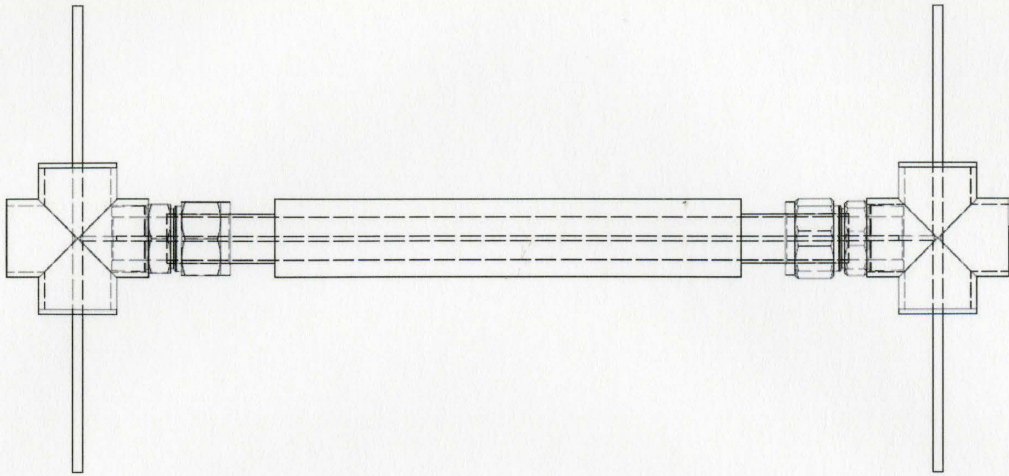


Figure 3.7: Schematic of the CCWCSE

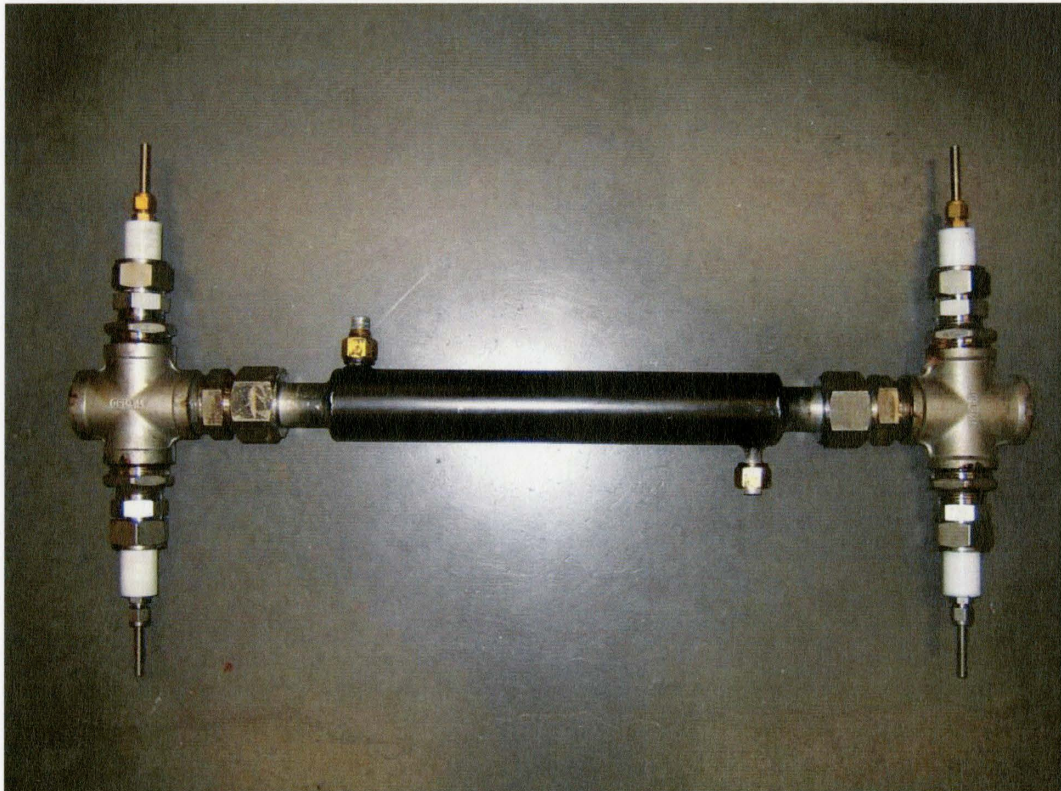


Figure 3.8: Image of the CCWCSE

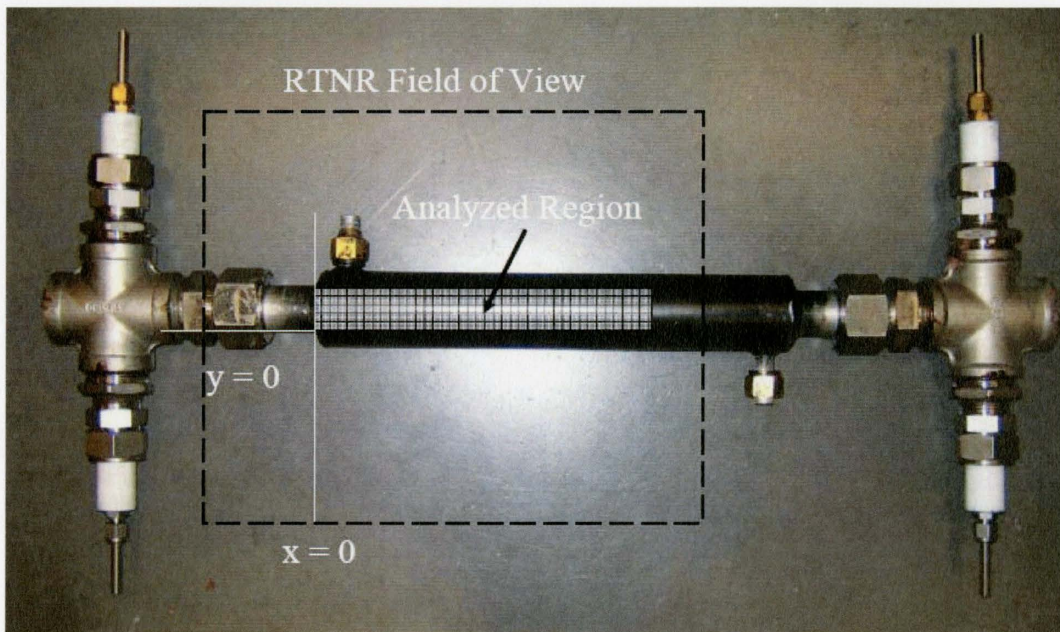


Figure 3.9: RTNR field of view and analysis region of the CCWCSE

III is between 0.1 to 100 μm and an accuracy of $\pm 10\%$. The near-forward light scattering principle uses an infrared light source positioned at a 90° from a photo-detector. As the soot particles from the exhaust gas cross the infrared beam, they scatter, and the amount of light received from the photo-detector is directly proportional to the soot mass concentration. Internal signal processing within the system compensates for noise and drift. The HAZ-DUST III then records the information within its internal memory at a sampling rate of 1 second.

The gas composition, in particular, O_2 , CO , CO_2 and NO_x , was measured using the EuroTron GreenLine 8000 flue gas analyzer. The GreenLine 8000 uses non-dispersive infrared sensors to measure CO_2 and CO , and electrochemical sensors to measure O_2 and NO_x simultaneously. It has an accuracy of $\pm 0.1\%$ vol for O_2 , $\pm 4\%$ for CO , $\pm 0.3\%$ for CO_2 and $\pm 4\%$ for NO_x . The GreenLine 8000 can record these measurements within its internal memory at a sampling rate of 1 minute. Both the soot mass concentration and gas composition used an isokinetic sampling technique.

3.2 Near Zero Emission Diesel Exhaust Test Facility

The source of the diesel engine exhaust gas is supplied by a 2.4kW LOMBARDINI 15LD350 single cylinder diesel engine generator located in the Near Zero Emission Diesel Exhaust Test Facility (NZE-DTF) as shown in Figure 3.10, where the engine characteristics are summarized in Table 3.1.

Two main modifications were made to this engine; the fuel tank and the exhaust system. The fuel tank was replaced by a graduated cylinder to measure fuel consumption. The exhaust system was modified such that the exhaust gas mass flow

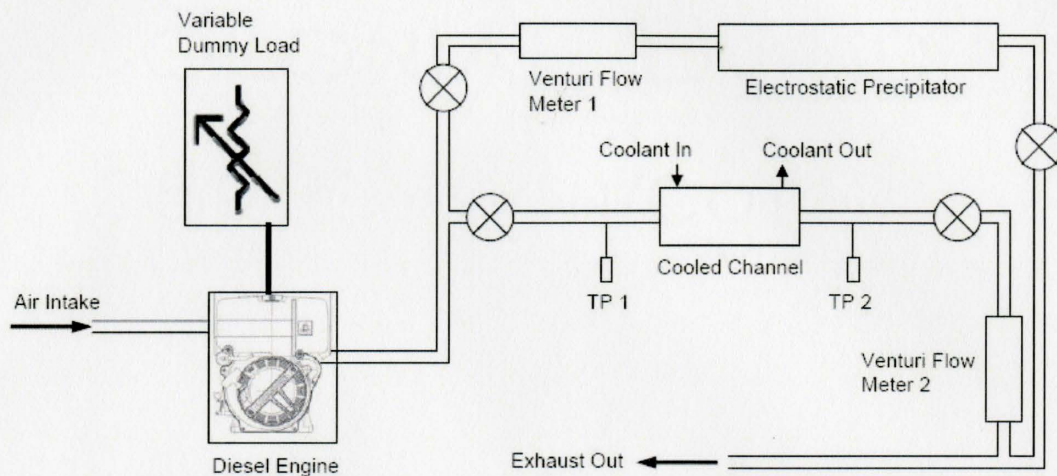


Figure 3.10: Schematic of the NZE-DTF

Table 3.1: Lombardini 15LD350 engine characteristics

Cylinders (No.)	Bore & Stroke (mm × mm)	Displacement (cm ³)	Speed (rpm)	Max Power (kW/HP)	Max Torque (Nm@rpm)
1	76 × 66	350	3600	5.5/7.4	16.5@2400

rate could be controlled; by connecting the engine exhaust manifold to a parallel piping system consisting of a test leg and a bypass leg. The cooled section was connected to the test leg and the flow was monitored by a Venturi flow meter (VFM II); flow was regulated by two gate valves located at each end of the test leg and any excess flow was accommodated by the bypass leg which was also monitored by a Venturi flow meter (VFM I). The differential pressure across the Venturi flow meter was measured using a Validyne DP15TL differential pressure transducer connected to pressure taps in the Venturi flow meter. Temperature was also measured at the Venturi flow meters to adjust for gas density via a lookup table. A calibration curve of both Venturi flow meters can be found in appendix A. There were two test points located at the upstream and the downstream of the cooled chambers. These two test points allowed the upstream and downstream measurements of soot mass concentration, gas composition and temperature as mentioned in section 3.1.

In parallel to the diesel engine, a compressed air source and heater was attached to the exhaust gas loop. The main purpose of the heated air source was to inject hot air into the exhaust loop, particularly into the test leg, to preheat the leg; this reduced the temperature transient prior to starting the main soot deposition experiments.

Gas composition, mainly O_2 , SO_2 , CO_2 , NO_x and particulate matter (PM) concentrations, was found to be dependent on the engine load, (Ewing et al., 2004). The engine load could be varied between 0 and 3.4kW by attaching a 120V electrical generator to the engine drive shaft. The generator was then attached to a resistor bank (dummy load) consisting of 12, 36Ω resistors, each dissipating 0.42kW of average power. In the course of these experiments, the engine load was fixed at 2.4kW resulting a PM mass concentration fluctuating between 190 and 210 mg/m^3 .

In order to feed the cooling channels of both test sections, a closed water cooling loop as shown in Figure 3.11 was used. The water cooling loop consisted of a

GRUNDFOS UP 25-64 pump, reservoir and heat exchanger; the entire system had a capability of pumping water at 10 L/min to the cooling channels of the test sections.

3.3 Dynamic Neutron Radiography Facility

Once the cooled section was sooted, the soot deposition thickness profile was measured by a non-destructive Real-Time Neutron Radiography (RTNR) developed by Ismail et al. (2004a) utilizing the Dynamic Neutron Radiography (DNR) Facility located at beam port 3 in the McMaster Nuclear Reactor (MNR), as shown in Figure 3.12. The MNR operates at a standard of 3MW thermal providing the neutron source for the DNR, the neutrons are then collimated using a series of lead, paraffin wax and boron carbide collimators with a bismuth filter, yielding a collimated neutron beam with a flux of 1.1×10^7 n/cm² - s inside the beam cave (Khaial et al., 2006). The collimated neutron beam is a key part of the RTNR technique where the system is shown in Figure 3.13. The RTNR system consists of a neutron source, a ZnS/LiF scintillator screen that converts thermal neutrons to photons, a CCD camera and a camera shielding box. The object of study is placed in between the neutron source and the ceramic screen such that the neutron beam is attenuated by the object of study, the main neutron beam and the attenuated neutrons are then projected on to the ZnS/LiF scintillator screen, the LiF absorbs the neutrons and converts them to α -particles and the ZnS converts the energy from the α -particles into photons. The scintillator screen size is the limiting factor to the field of view of the RTNR system, with an area of 200 x 200mm. The CCD camera placed inside the camera box then captures these photons at a rate of 30 fps and is recorded on to a digital recording device, the recorded image represents neutron intensity scaled into 256 greyscale levels (8-bit), where 0 is black and 255 is white. The camera box serves two purposes;

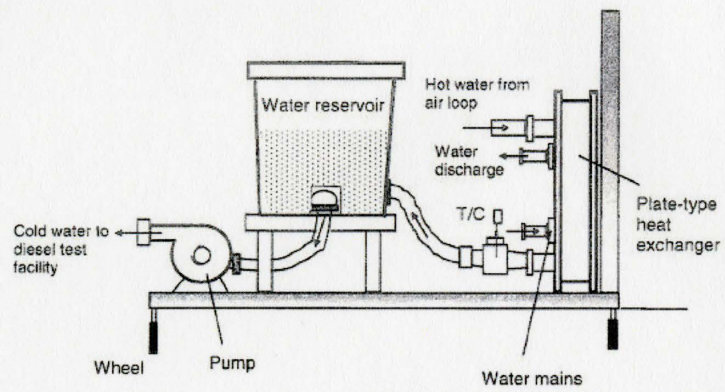


Figure 3.11: Cooling water loop

to shield the camera from radiation damage and to prevent any foreign light source that will interfere with the neutron converted photons. The camera box also uses two mirrors to reflect the photons in two 90 degree bends; this positions the camera away from the direct path of the neutron beam. The RTNR system also allows the object of study to be rotated axially normal to the ground (x-axis) giving the ability to analyze the test section at different angles with the possibility of reconstructing the image in 3-D.

3.4 Image Processing for Determining Deposited Soot Thickness

Once a real-time neutron radiograph image has been recorded, the live image must be processed to reduce any background noise and section off the region of interest to result in a soot thickness profile, a block diagram is shown in Figure 3.14 to summarize the steps of the image processing. Three key RTNR images must be obtained to successfully process an image for soot thickness profiling; an image of a clean cooled section, an image of the same section with soot deposited inside and a neutron beam image of the same RTNR session. Each RTNR image are frame averaged at 200 frames using HImage++ to remove any background noise and convert the live image to a still photograph, if required, further noise can be removed by filtering. Once the frame captured is completed, the image processing data is passed to MATLAB 6.5 for further analysis. Edge detection is used to crop the image and focus on the region of interest as discussed in section 3.1. The beam image is then subtracted from each of the clean and sooted image for normalization; an example is shown in Figures 3.15 and 3.16 for a raw and normalized image respectively.

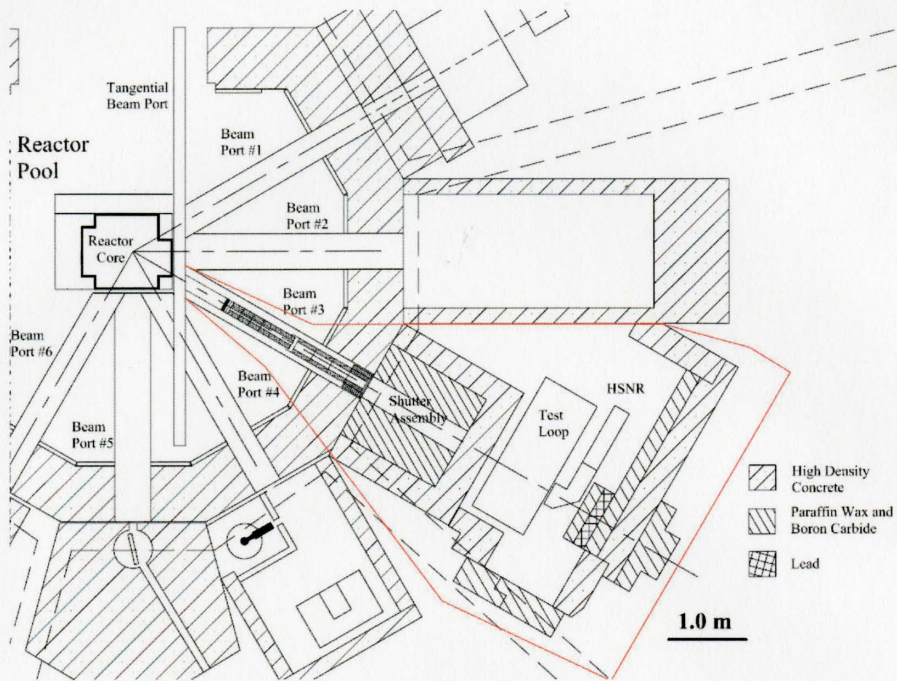


Figure 3.12: Location of the DNR at the MNR

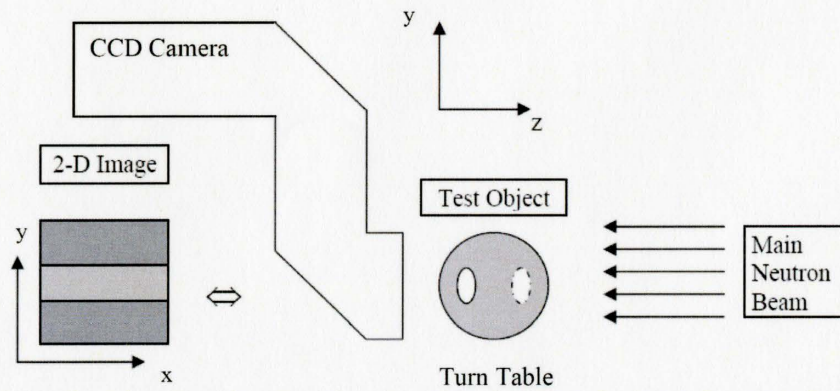


Figure 3.13: Schematic of the RNTR

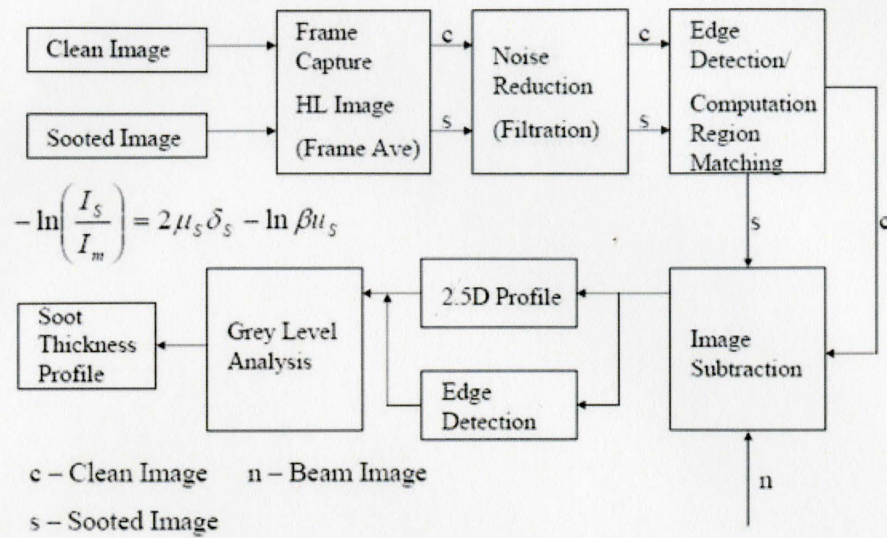


Figure 3.14: Block diagram of the image analysis process

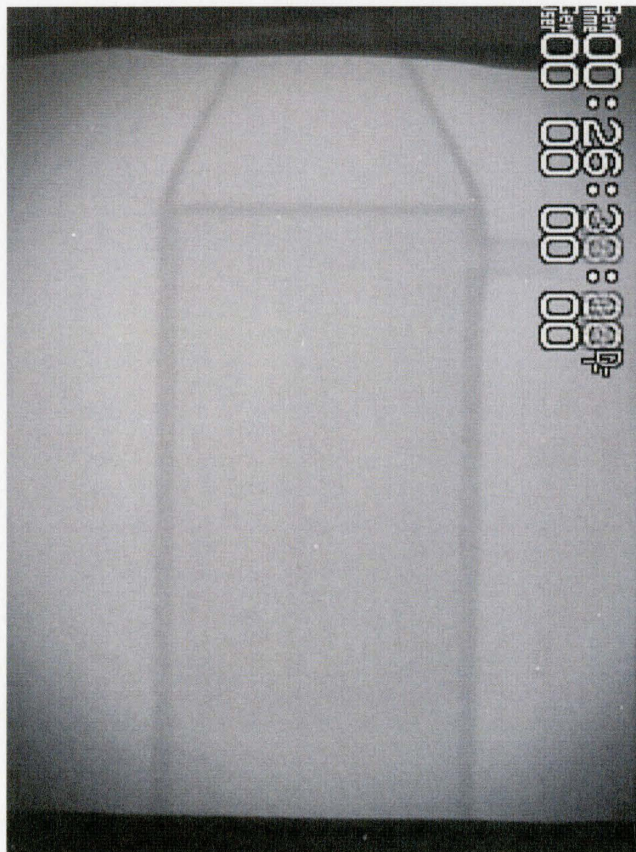


Figure 3.15: Raw RNTTR image of the RWCS



Figure 3.16: Normalized image of RWCS with background subtracted

Edge detection can be used again for non-destructive geometrical measurements, or soot thickness could be calculated by solving the approximation of the intensity of an attenuated neutron beam transmitted through an object consisting of different layers (Duderstadt and Hamilton, 1996).

$$\frac{I(x, y)}{I_o} = B(\delta_s, \mu_s)(\mu_m \mu_s) \exp(-2\mu_s \delta_s(x, y) - 2\mu_m \delta_m(x, y)) \quad (3.1)$$

, where, I is the attenuated object with soot image and I_o is the incident neutron beam. B is the build up factor due to neutron back scattering and μ_s is the attenuation coefficient of soot, calculated to be 1 and 0.023 mm^{-1} by Ismail et al. (2004), μ_m is the attenuation coefficient of aluminum, δ_s is the thickness of soot and δ_m is the thickness of the aluminum. Note that there is a 2 in front of both thickness terms since the equation takes into consideration the assumed front and back layer of the test section. Hence,

$$\frac{I_m(x, y)}{I_o} = B(\delta_s, \mu_s) \mu_m \exp(-2\mu_m \delta_m(x, y)) \quad (3.2)$$

$$-2\mu_m \delta_m(x, y) = \ln(I_m(x, y)/I_o(x, y)) - \ln B(\delta_s, \mu_s) \mu_m \quad (3.3)$$

, where I_m is the attenuated image of a clean test section. Subbing equation 3.3 into 3.1 and simplifying to yield

$$\frac{I(x, y)}{I_m(x, y)} = \exp(-2\mu_s \delta_s(x, y)) \quad (3.4)$$

The soot thickness term $2\delta_s$ can be isolated and solved for in MATLAB 6.5.

$$2\delta_s(x, y) = -\ln(I_s(x, y)/I_m(x, y)) \mu_s \quad (3.5)$$

Since I and I_m are a 2 dimensional 424×247 pixel image, each pixel value is considered an element in a 424×246 matrix, then the soot thickness profile is the result.

Chapter 4

Experimental Results

The effect of wall cooling on soot deposition was investigated for two geometries; a rectangular and cylindrical wall cooled section (RWCS and CWCS respectively). Both geometries were studied with a fixed nominal exhaust mass flow rate of 20 ± 2 kg/h, an engine load of 2.4 ± 0.2 kW and a water coolant flow of 9.5 ± 0.2 L/min for all cases. The parameters investigated were initial cooling temperature of 20 ± 3 °C, 40 ± 3 °C, no cooling water and exposure times of 1, 2 and 3hrs. The Reynolds Number, based on the mass flow per cross sectional area times the hydraulic diameter, was 6300 for the rectangular cooling section and 9000 for the cylindrical cooling section. The nominal upstream gas temperature for the rectangular cooling sections was 260 ± 3 °C and 270 ± 3 °C for the cylindrical section. Both the temperature profile for the outside cooling wall and the soot deposition profile will be compared for this investigation.

4.1 Particulate Matter Mass Concentration and Gas Composition

An important parameter in this study is PM mass concentration because it dictates the amount of soot deposition that are caused by the different mechanisms as stated in section 2.2. Typical PM mass concentration levels taken at the inlet of the devices can be observed in Figure 4.1 over a 2hr operating period, with a minimum of $105 \pm 11 \text{mg/m}^3$ a maximum of $131 \pm 13 \text{mg/m}^3$ and a time average of $114 \pm 11 \text{mg/m}^3$ calculated after 40 ± 1 minutes of operation, where PM levels have reached a steady state. It can be observed that there was a sudden increase between the 100 ± 1 and 120 ± 1 minute of operation which may be due to the re-entrainment of deposited soot at the upstream of the sampling point. Along with PM mass concentration, NO_x , CO , CO_2 and O_2 were monitored to ensure engine conditions were consistent. It can be observed in Figure 4.2 that typical NO_x and CO levels over a 2hr operation time; with NO_x concentration levels having a minimum of $432 \pm 17 \text{ppm}$, a maximum of $512 \pm 20 \text{ppm}$ and a time average of $457 \pm 18 \text{ppm}$; and the CO concentration levels having a minimum of $571 \pm 50 \text{ppm}$, a maximum of $800 \pm 50 \text{ppm}$ and a time average of $710 \pm 50 \text{ppm}$. Figure 4.3 shows the number concentration percentage of CO_2 and O_2 in the exhaust gas; with O_2 having a minimum of $13 \pm 0.3 \%$, a maximum of $13.6 \pm 0.3 \%$ and a time average of $13.3 \pm 0.3 \%$; CO_2 having a minimum of $5.8 \pm 0.3 \%$, a maximum of $6.1 \pm 0.3 \%$ and a time average of $5.9 \pm 0.3 \%$.

4.2 Rectangular Wall Cooled Section

Typical exhaust gas temperature characteristics of the rectangular wall cooled section (RWCS) are shown in Figure 4.4, the engine exhaust gas has a temperature

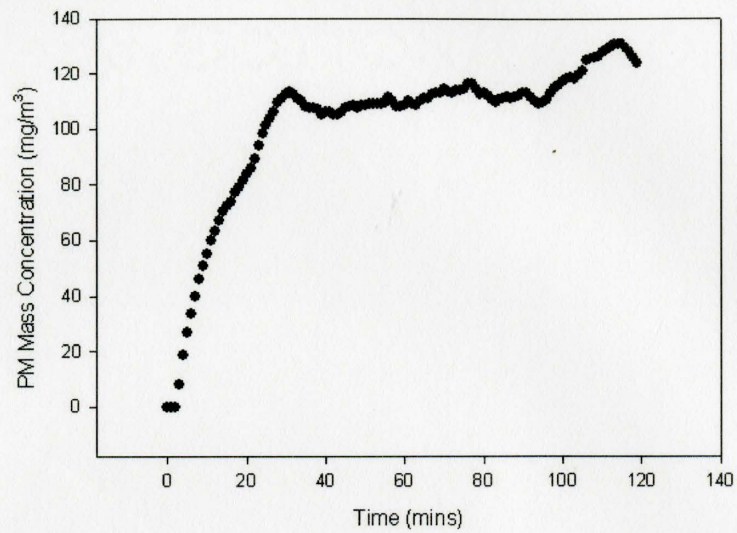
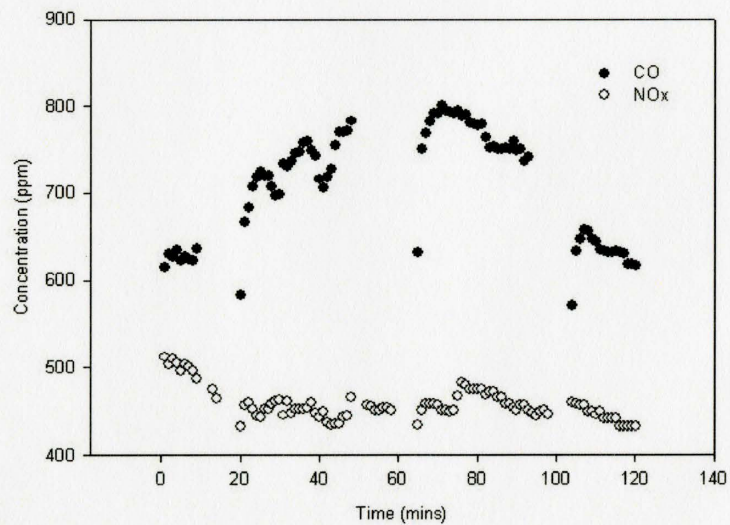


Figure 4.1: Transient of nominal exhaust Gas PM mass concentration

Figure 4.2: Transient of nominal exhaust Gas CO and NO_x concentration

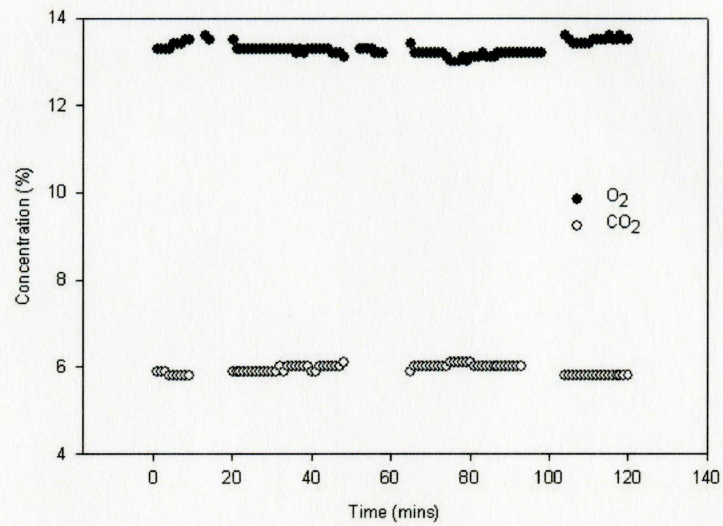


Figure 4.3: Nominal Exhaust Gas O₂ and CO₂ concentration

transient over the initial 40 ± 1 minutes of the test, this is caused by the thermal inertia of the cool metal pipes of the test section and the cool metal components of the diesel engine. After the initial 40 ± 1 minutes it can be observed that the temperature reaches a steady state temperature of $260 \pm 3^\circ\text{C}$ with the downstream temperatures ranging from $166 \pm 3^\circ\text{C}$ to $185 \pm 3^\circ\text{C}$ depending on the initial coolant temperature, with the downstream temperature increasing as the initial cooling temperature increases. Typical cooling system temperature characteristics are shown in Figure 4.5 with initial temperature increasing as time increases reaching a steady state of $40 \pm 3^\circ\text{C}$. For the 20°C case, it can be observed that the temperature has a $15 \pm 3^\circ\text{C}$ increase in a time span of 2hrs; caused by the inability to remove enough heat from the heat exchanger of the closed loop water cooling system.

4.2.1 Effect of Diesel Flue Gas Exposure Time on Soot Deposition

Two-dimensional soot deposition profiles for sooted diesel exhaust flow exposure time with a constant coolant temperature of $40 \pm 3^\circ\text{C}$ were investigated. The resulting two-dimensional soot deposition profiles are shown in Figures 4.6, 4.8 and 4.10 for exposure times of 1, 2 and 3hrs respectively, where the corresponding outside wall temperature distribution profile are shown in Figure 4.7, 4.9 and 4.11 respectively. It can be observed that there is an increase of deposited soot as the exposure time increases. Note the analyzed regions of the soot deposition profiles and the temperature distribution profile are $3/4$ of the entire region of the device from the upstream entrance as discussed in chapter 3. Also note that the exhaust gas flow is from left to right and gravity points into the page.

For the 1hr case, Figure 4.6 shows the mean amount of deposition thickness

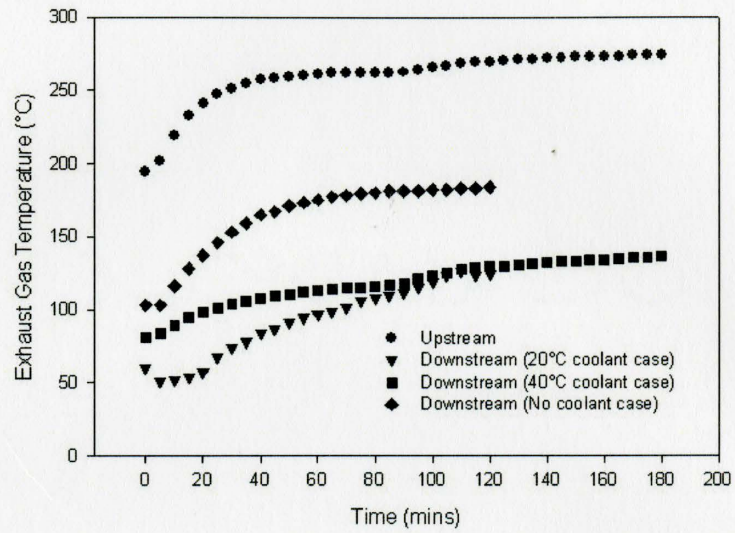


Figure 4.4: Transient of nominal exhaust gas temperature

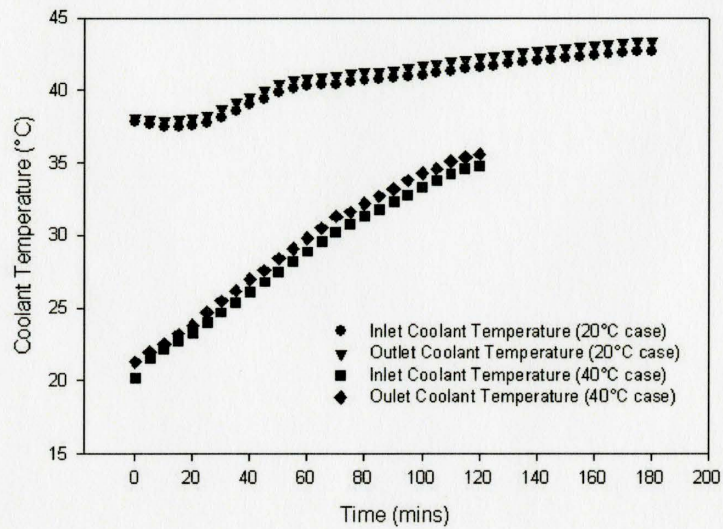


Figure 4.5: Transient of nominal coolant temperature

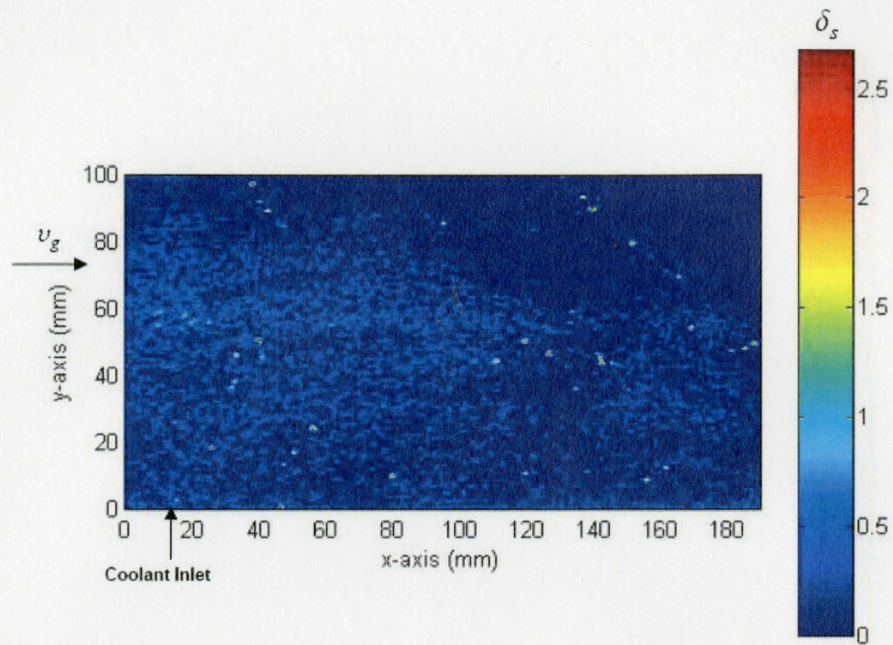
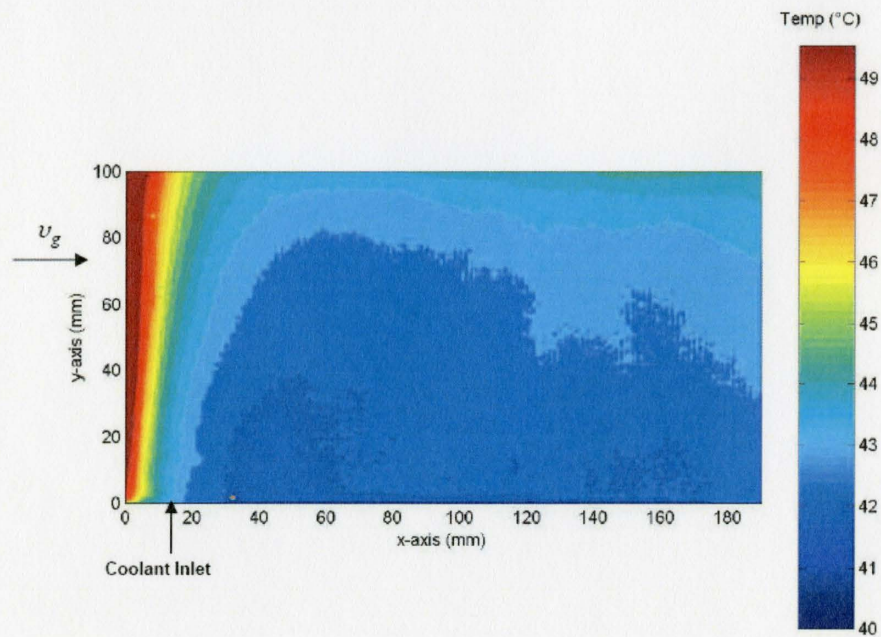
Figure 4.6: Soot deposition profile of RWCS for 40 °C, 1hr case; δ_s in mm

Figure 4.7: Nominal RCWS outside wall temperature profile for 40 °C, 1hr case

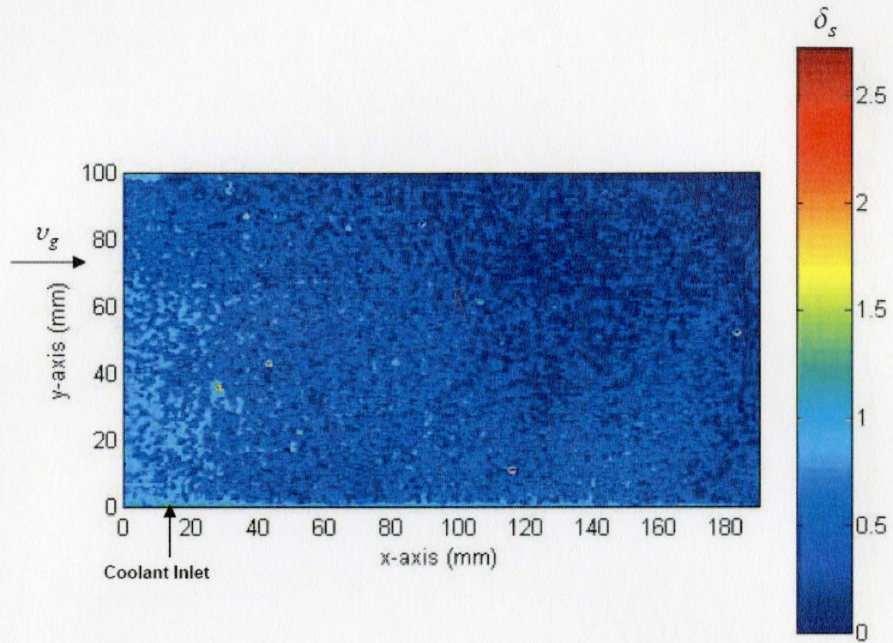


Figure 4.8: Soot deposition profile of RWCS for 40°C, 2hr case; δ_s in mm

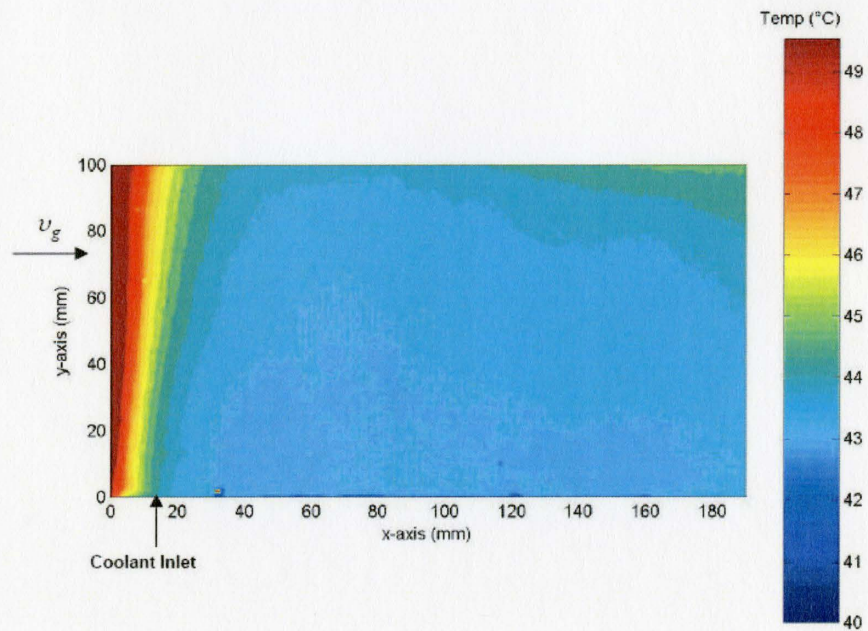


Figure 4.9: Nominal RCWS outside wall temperature profile for 40°C, 2hr case

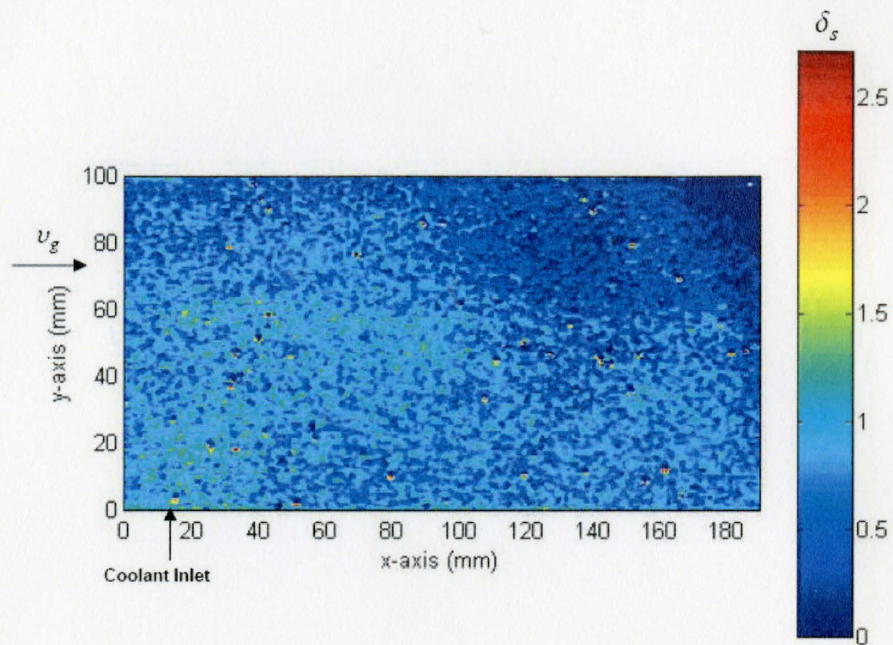


Figure 4.10: Soot deposition profile of RWCS for 40°C, 3hr case; δ_s in mm

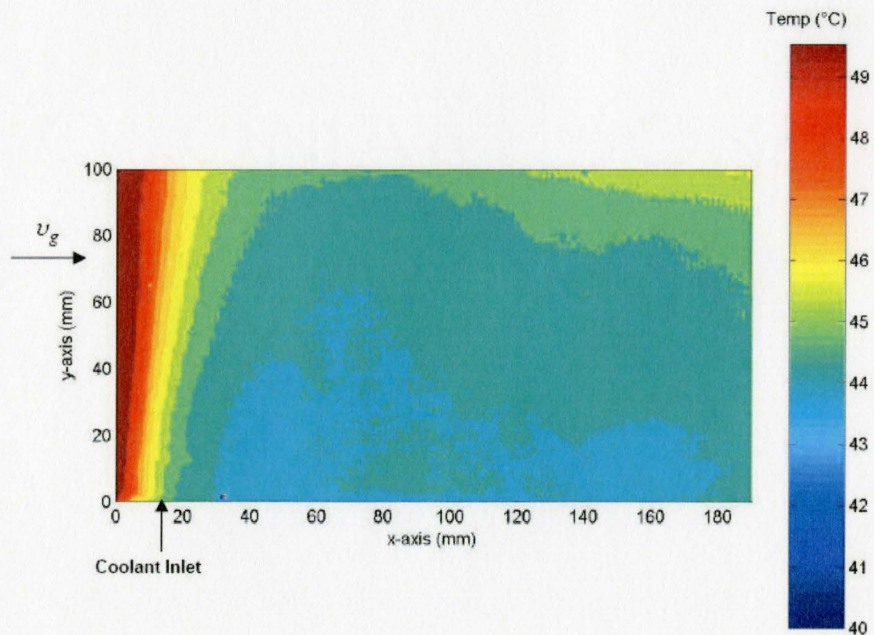


Figure 4.11: Nominal RCWS outside wall temperature profile for 40°C, 3hr case

is 0.21 ± 0.03 mm along the entire area of analysis. The three soot deposition profiles of the soot deposition along the x-axis at $y = 5$ mm, 50 mm and 95 mm are shown in Figure 4.12. Figure 4.12 shows that the mean soot deposition at $y = 50$ mm is thicker than at $y = 5$ mm and 95 mm with a mean soot deposition of 0.17 ± 0.03 , 0.27 ± 0.04 and 0.057 ± 0.009 mm respectively, where this suggests that the deposition is thicker at the central region of the device. This thicker deposition along the central region may be due to the non-ideal distribution of the exhaust gas caused by a jet from the transition of the cylinder inlet to the RWCS gas channel.

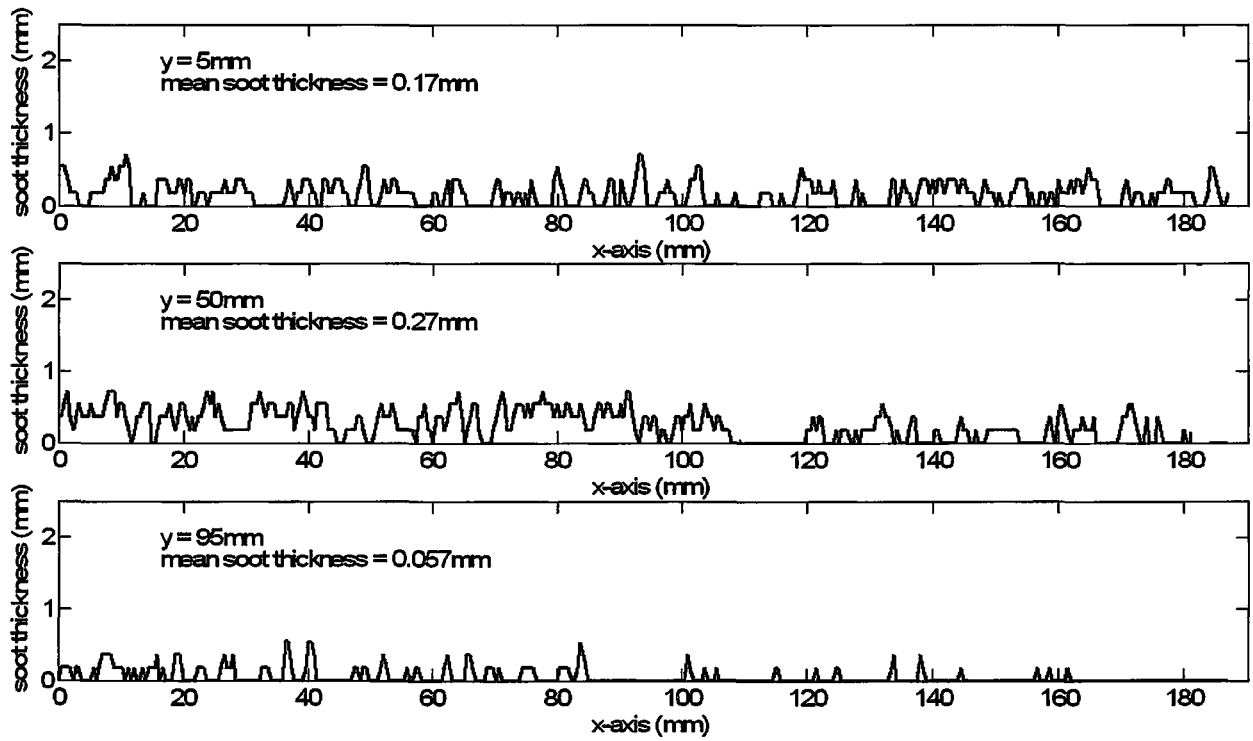


Figure 4.12: x-axis soot deposition profile of 1hr exposure time and 40°C coolant temperature at $y = 5\text{mm}$, 50mm and 95mm .

For the 2hr case in Figure 4.8, it can be observed that the soot deposition thickness has started to increase with a mean deposition thickness of $0.50\pm 0.08\text{mm}$. The soot deposition is now concentrated at the entrance region of the RWCS gas channel that may be due to entrance effects and convection. There are also localized soot deposition close to the coolant inlet that may be due to combination of thermophoresis, particle agglomeration and enhanced adhesion due to water condensation on the gas wall. The soot deposition profile pattern in Figure 4.8 is qualitatively matching the outer wall surface temperature profile pattern as shown in Figure 4.9, with the exception of the entrance region due to the axial conduction of the device seen in the thermal image, where the soot deposition being biased to the lower portion of the device. The three soot deposition profiles of the soot deposition along the x-axis at $y = 5\text{mm}$, 50mm and 95mm are shown in Figure 4.13, with mean depositions of 0.55 ± 0.09 , 0.46 ± 0.07 and $0.36\pm 0.06\text{mm}$ respectively were observed. Figure 4.13 shows that there is more deposition at the inlet section and at the lower portion of the RWCS wall where the cooling water inlet is located, compared to the top portion.

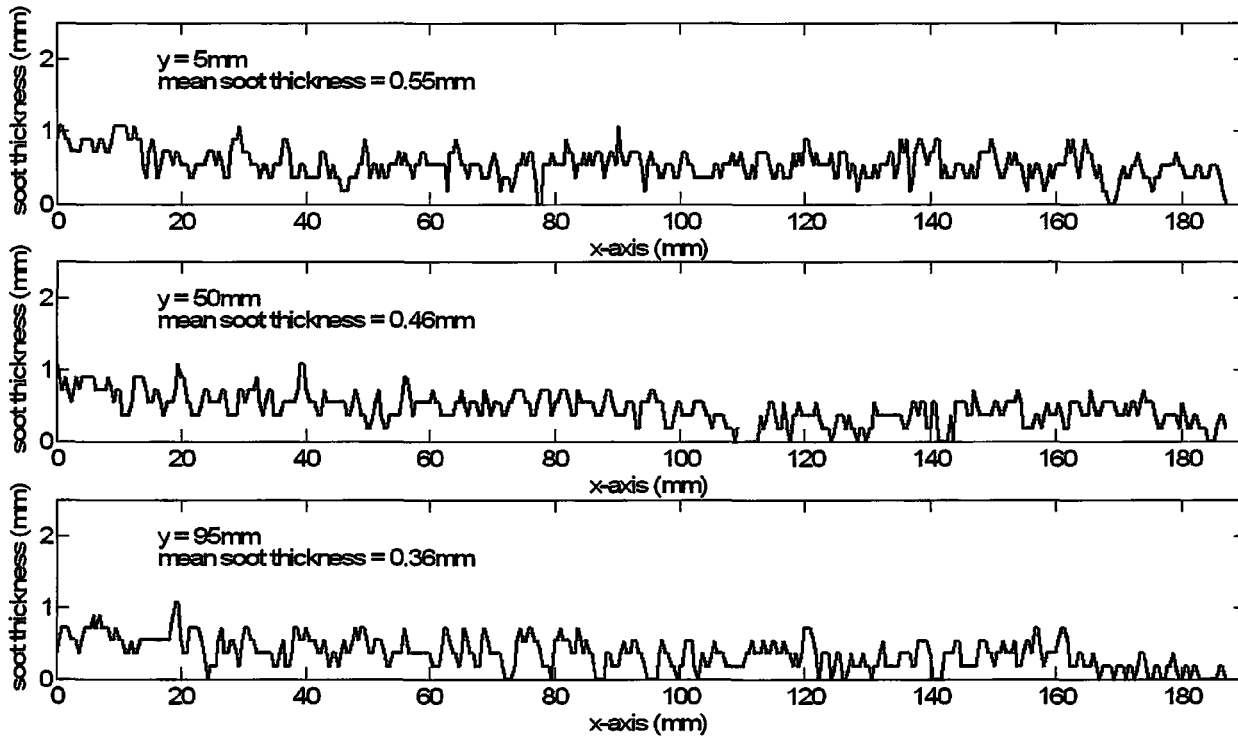


Figure 4.13: x-axis soot deposition profile of 2hr exposure time and 40°C coolant temperature at $y = 5\text{mm}$, 50mm and 95mm.

For the 3hr case in Figure 4.10, it can be observed that the soot deposition has increased significantly with a mean deposition thickness of $0.82\pm.13\text{mm}$. The soot deposition is still concentrated both at the inlet section of the RWCS wall and near the coolant inlet. The soot deposition profile pattern in Figure 4.10 has a close qualitative match to the wall surface temperature profile pattern in Figure 4.11, where the soot deposition being biased toward the lower portion of the device. Again taking three line profiles of the soot deposition along the x-axis at $y = 5\text{mm}$, 50mm and 95mm are shown in Figure 4.14, where the mean soot deposition thickness are 0.88 ± 0.14 , 0.50 ± 0.08 and $0.58\pm 0.09\text{mm}$ respectively along the x-axis. It can be observed that there is significantly more deposition at the inlet section and at the lower portion of the RWCS wall near the coolant inlet section, compared to the top portion of the device.

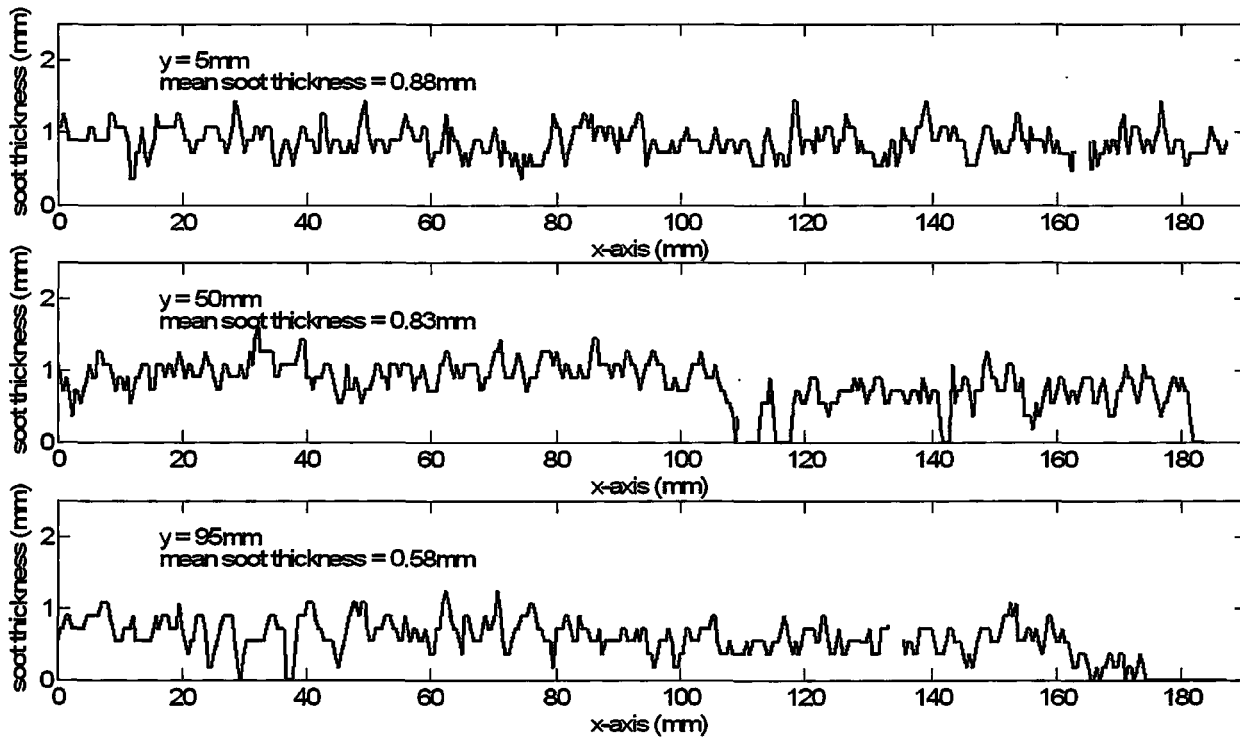


Figure 4.14: x-axis soot deposition profile of 3hr exposure time and 40 °C coolant temperature at $y = 5\text{mm}$, 50mm and 95mm .

4.2.2 Effect of Cooling Temperature on Soot Deposition

Two-dimensional soot deposition profiles for initial inlet coolant temperature of $20 \pm 3^\circ\text{C}$ and no coolant cases are shown in Figures 4.15 and 4.17 respectively at a constant exposure time of 2hrs. Corresponding outer wall temperature profiles are shown in Figures 4.16 and 4.18 for initial inlet coolant temperature of $20 \pm 3^\circ\text{C}$ and no coolant cases respectively.

Figure 4.15 with the $20 \pm 3^\circ\text{C}$ coolant temperature and 2hr exposure time case shows that there is a significant amount of deposition with a mean soot deposition thickness of $0.91 \pm 0.15\text{mm}$ along the entire area of the analysis region. The soot deposition profiles along the x-axis at $y = 5\text{mm}$, 50mm and 95mm is shown in Figure 4.19, where all three profiles have relatively the same mean soot deposition of $0.88 \pm 0.14\text{mm}$ for $y = 5$ and $y = 95\text{mm}$, and $0.9 \pm 0.14\text{mm}$ for $y = 50\text{mm}$. This result suggests that deposition is more uniform along the y-axis and also a significant deposition concentration at the entrance of the channel section that may be due to entrance effects and convection as shown in Figure 4.19.

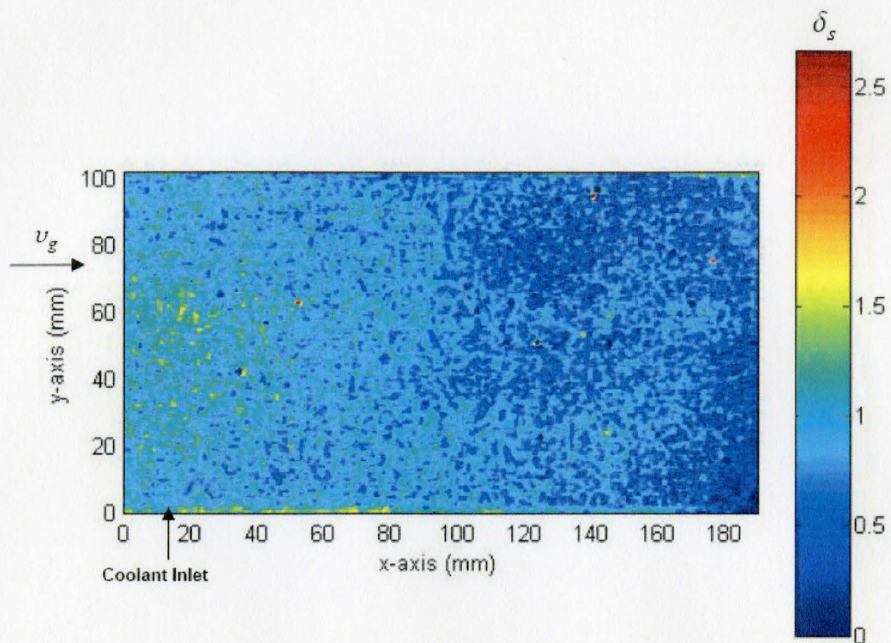


Figure 4.15: Soot deposition profile of RWCS for 20 °C, 2hr case; δ_s in mm

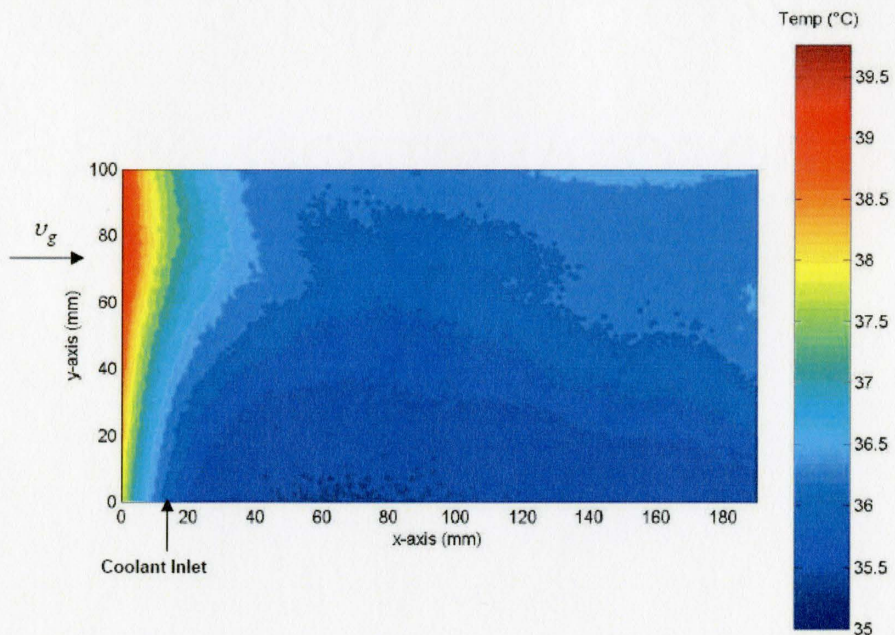


Figure 4.16: Nominal RCWS outside wall temperature profile for 20 °C, 2hr case

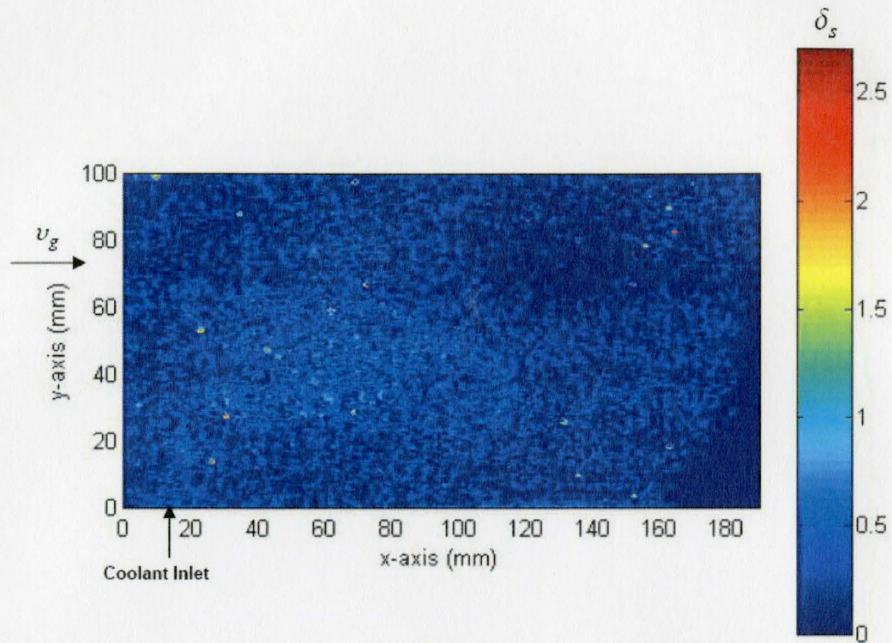


Figure 4.17: Soot deposition profile of RWCS for the no coolant, 2hr case; δ_s in mm

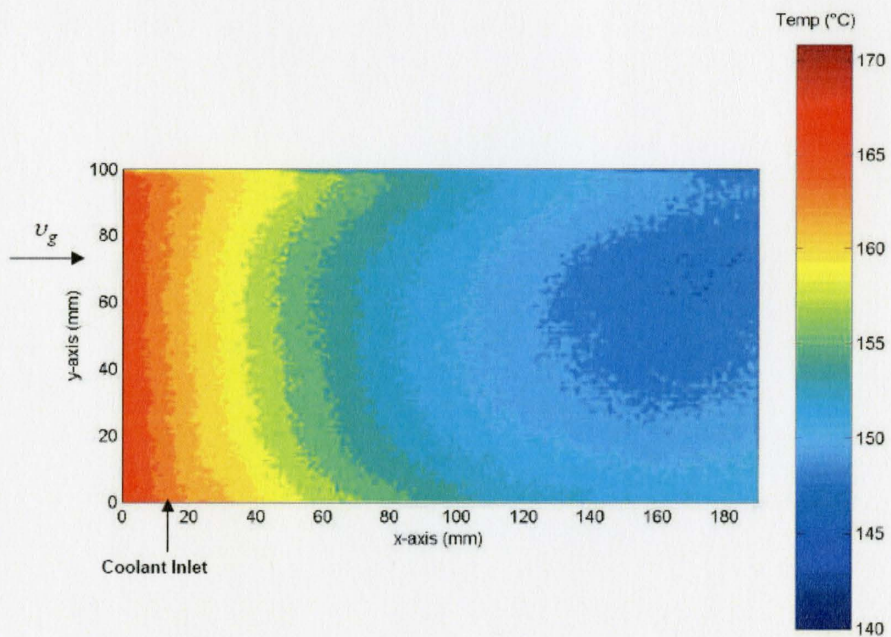


Figure 4.18: Nominal RCWS outside wall temperature profile for no coolant, 2hr case

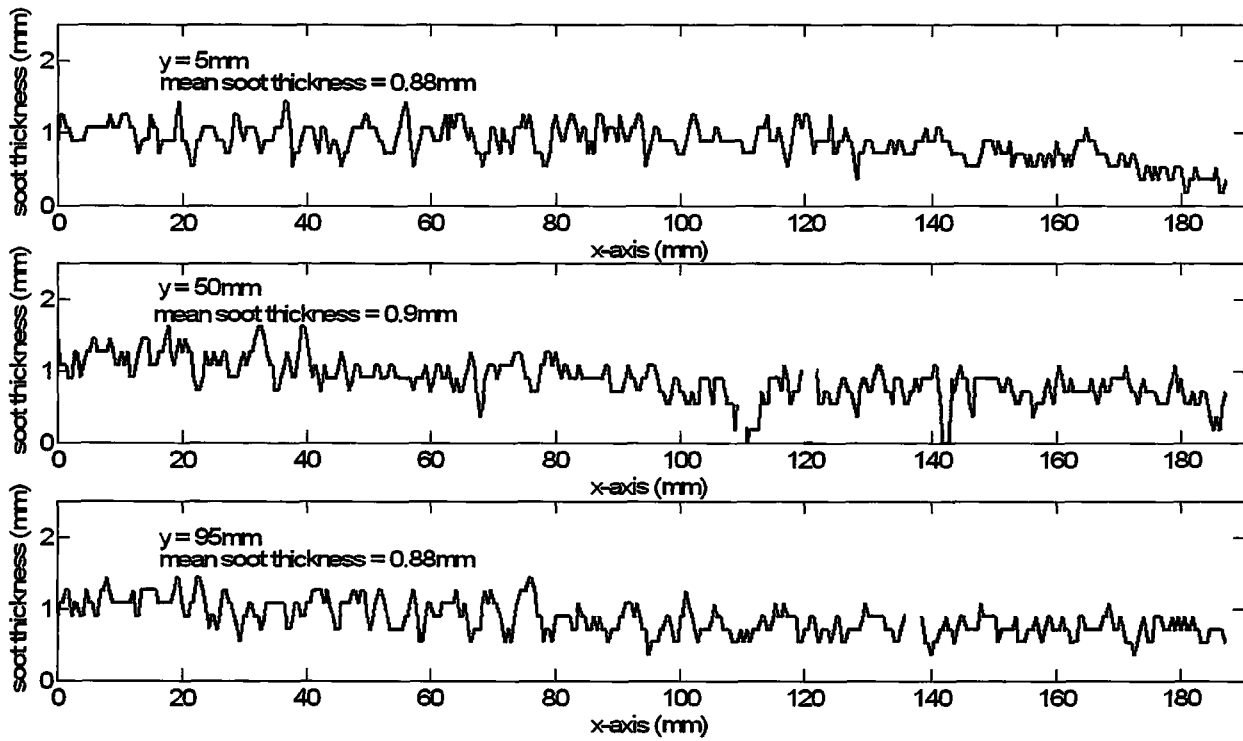


Figure 4.19: x-axis soot deposition profile of RWCS for 2hr exposure time and 20°C coolant temperature at $y = 5\text{mm}$, 50mm and 95mm

For the $40 \pm 3^\circ\text{C}$ inlet coolant temperature and 2hr case exposure time as shown before in Figure 4.8 that the soot deposition has significantly thinner with a mean deposition thickness of $0.50 \pm 0.08\text{mm}$ with the soot deposition concentrated at the inlet section of the RWCS wall and coolant inlet region.

For the no coolant condition and 2hr exposure time case, it can be observed that the soot deposition has decreased even further with a mean deposition thickness of $0.33 \pm 0.05\text{mm}$ since wall is relatively hot and uniform as observed from the thermal image in Figure 4.18. The wall temperature was approximately $148 \pm 3^\circ\text{C}$. The soot deposition was no longer concentrated at the coolant entrance region of the RWCS wall, but more importantly the symmetrical deposition pattern observed may be due to less thermophoretic effects. Based on the soot deposition profiles along the x-axis at $y = 5\text{mm}$, 50mm and 95mm as shown in Figure 4.20, with mean depositions of 0.36 ± 0.06 , 0.46 ± 0.07 and $0.34 \pm 0.05\text{mm}$ respectively, there is significantly more deposition at the inlet region and at the lower portion of the gas channel wall compared to the top portion of the device wall.

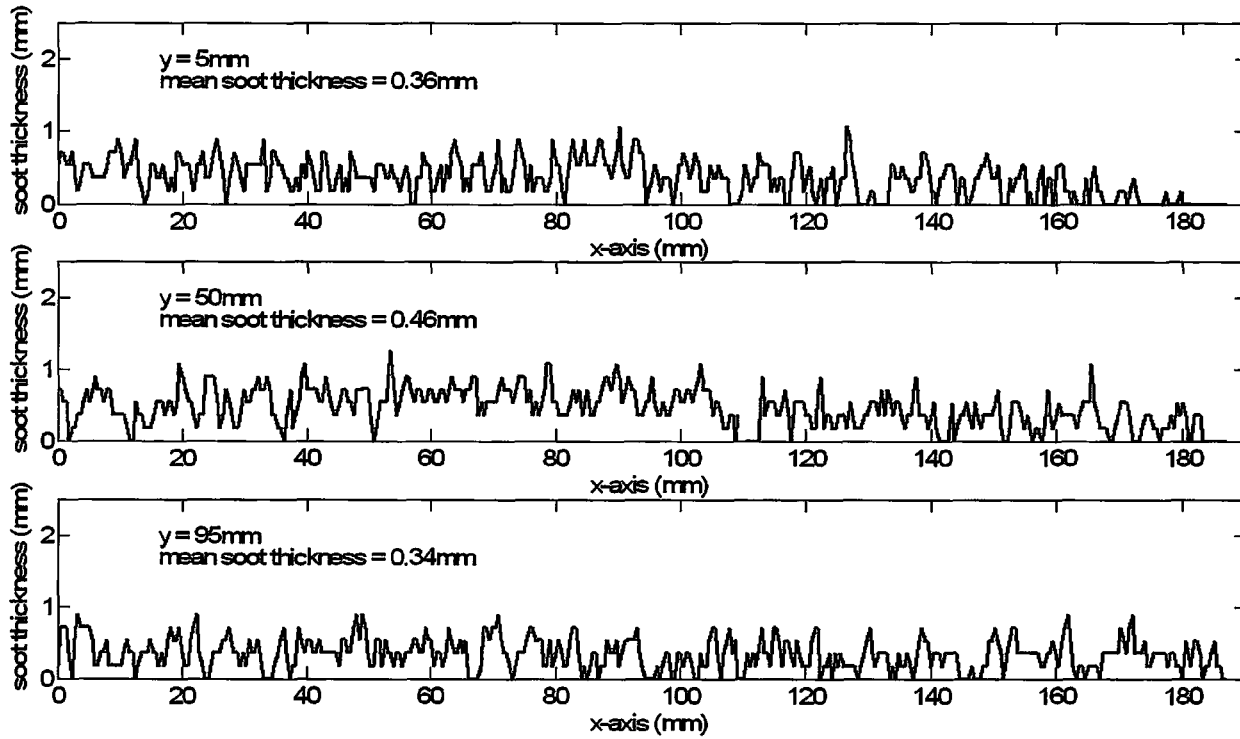


Figure 4.20: x-axis soot deposition profile of RWCS for 2hr exposure time and no coolant at $y = 5\text{mm}$, 50mm and 95mm .

4.3 Cylindrical Wall Cooled Section

Typical exhaust gas temperature characteristics of the cylindrical wall cooled section (CWCS) are shown in Figure 4.21, the engine exhaust gas has a temperature transient for the initial 40 ± 1 minutes of operation, again may be caused by the thermal inertia of the diesel loop in metal pipes of the test section and the cool metal components of the diesel engine. The system reaches a steady state exhaust gas temperature of $274 \pm 3^\circ\text{C}$ with the cooling section downstream temperatures ranging from $173 \pm 3^\circ\text{C}$ to $241 \pm 3^\circ\text{C}$ depending on the initial inlet coolant temperature after 40 ± 1 minutes of operation. Here the downstream temperature increased as the initial cooling temperature increased during this initial 40 ± 1 minute transient. Comparing these downstream exhaust gas temperatures with the RWCS downstream gas temperatures as shown in Figure 4.47, the CWCS temperatures are higher because the CWCS has a significantly less heat transfer surface on the gas channel (CWCS = 269cm^2 vs, RWCS = 500cm^2). Typical cooling system temperature characteristics are shown in Figure 4.22, where initial temperature increased with operation time then reaching a steady state of $40 \pm 3^\circ\text{C}$. For the $20 \pm 3^\circ\text{C}$ case, it can be observed that the temperature has a $15 \pm 3^\circ\text{C}$ increase in a time span of 2hrs; caused by the inability to remove enough heat from the heat exchanger of the closed loop water cooling system, as the case for the RWCS.

4.3.1 Effect of Diesel Flue Gas Exposure Time on Soot Deposition

Two-dimensional soot deposition profiles as a function of exposure time with a constant cooling temperature of $40 \pm 3^\circ\text{C}$. The resulting soot deposition thickness profiles is shown in Figures 4.23, 4.25 and 4.27 for exposure times of 1, 2 and 3hrs

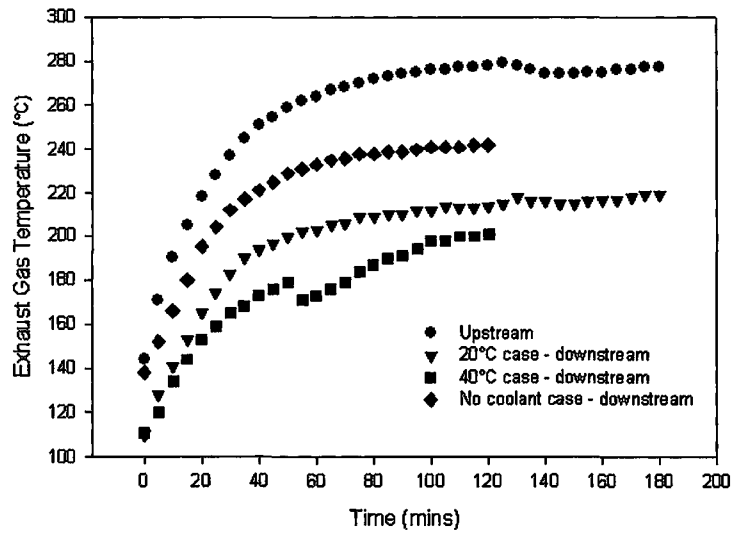


Figure 4.21: Transient nominal gas temperatures for CWCS

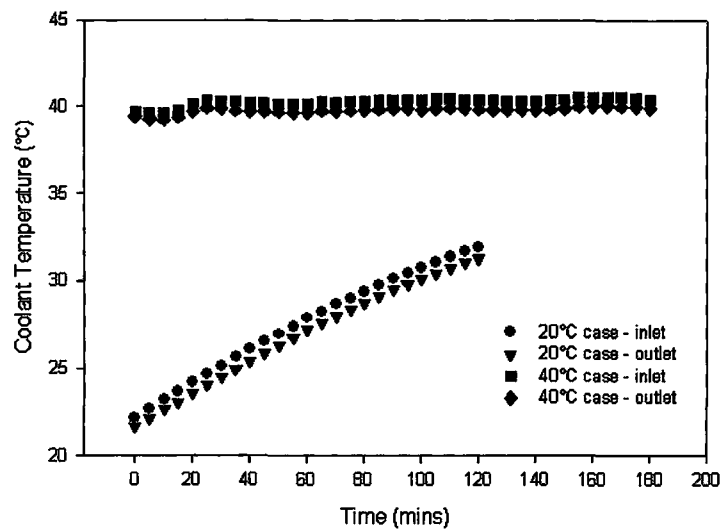


Figure 4.22: Transient nominal coolant temperatures for CWCS

respectively, where the corresponding wall surface temperature distribution profiles are shown in Figures 4.24, 4.26 and 4.28, respectively. It can be observed that there was an increase of deposited soot as the exposure time increased. Note similarly to the RWCS, the analyzed regions of the soot deposition profiles and the temperature distribution profiles are 3/4 of the entire region of the device from the upstream entrance as discussed in chapter 3. Also note that the exhaust gas flow is from left to right and gravity points into the page for all images.

For the 1hr exposure time case, it can be observed that the mean amount of deposition thickness is 0.20 ± 0.03 mm along the entire area of the analysis region as shown in Figure 4.23. Taking a cross-sectional average of the soot deposition over the radius of the CWCS, and plotting it along its length, as shown in Figure 4.29. The cross-sectional average wall soot thickness shows that a slight wavy pattern along its x-axis may be due to re-entrainment of deposited soot as proposed by Ismail et al. (2004b). There are no significant soot depositions near the coolant inlet region as shown in Figure 4.23, where it may suggest that there is no significant thermophoretic effects. Also deposition is uniformly distributed along the x-axis of the CWCS.

For the 2hr exposure time case as shown in Figure 4.25, the soot deposition has significantly increased with a mean deposition thickness of 0.51 ± 0.08 mm, by comparing to the 1hr exposure time case. The soot deposition is evenly distributed throughout the length of the CWCS that may be due to the rate of deposition and the rate of re-entrainment reaching an equivalent value, the entrance region of the CWCS has a smoother transition at the entrance region, thus has less entrance effects. There is also a slight deposition bias to the lower section may be due to a slight gravitational effect or re-entrained coagulated soots. A cross-sectional average of the soot deposition thickness along its x-axis is shown in Figure 4.30, where the wavy pattern is still present but not significant.

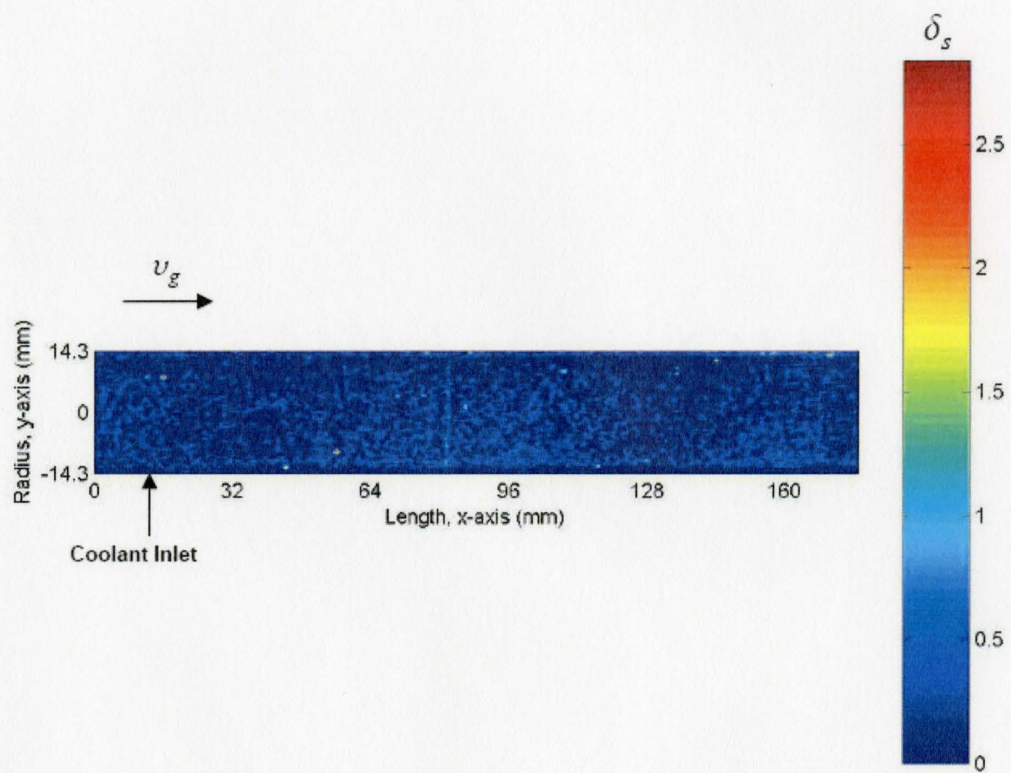


Figure 4.23: Soot deposition profile of CWCS for 40°C, 1hr case; δ_s in mm

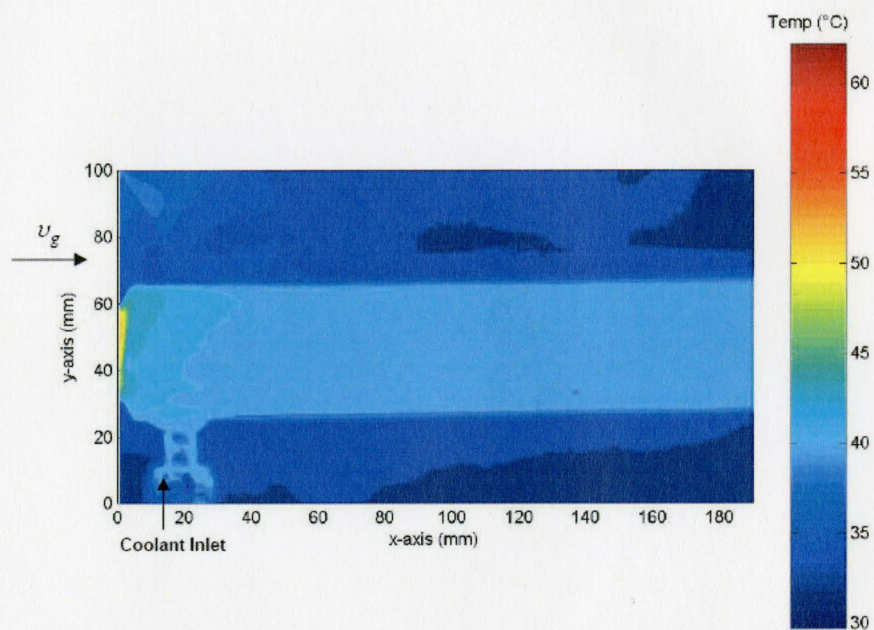


Figure 4.24: Temperature profile of CWCS for 40 °C, 1hr case

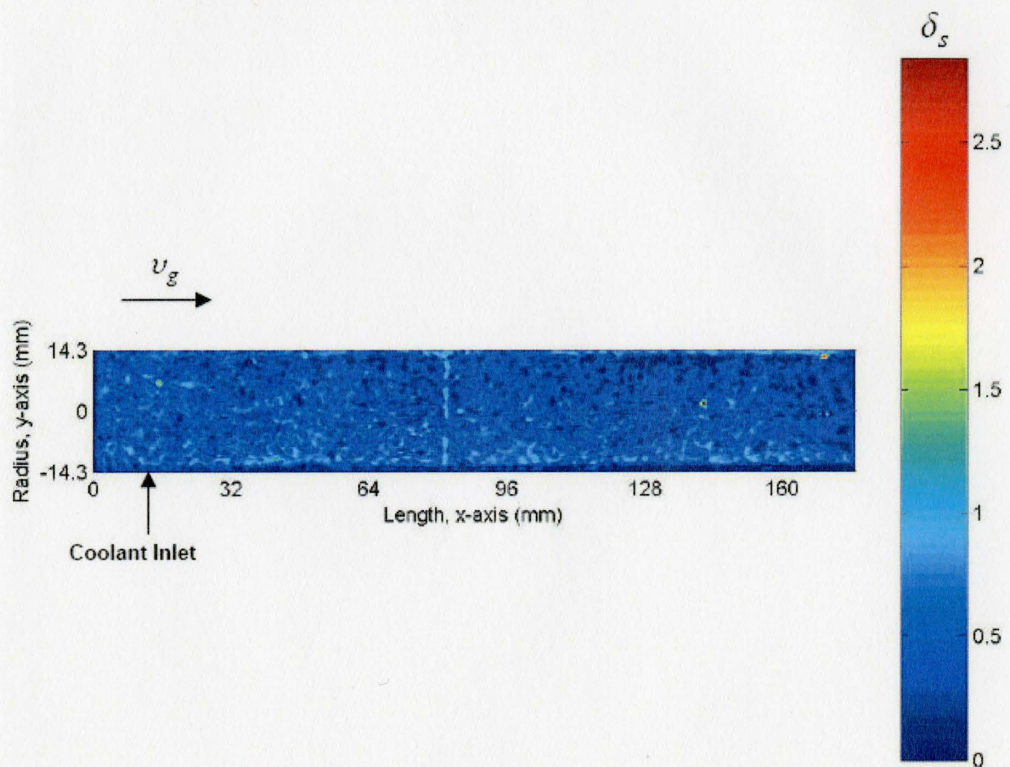


Figure 4.25: Soot deposition profile of CWCS for 40°C, 2hr case; δ_s in mm

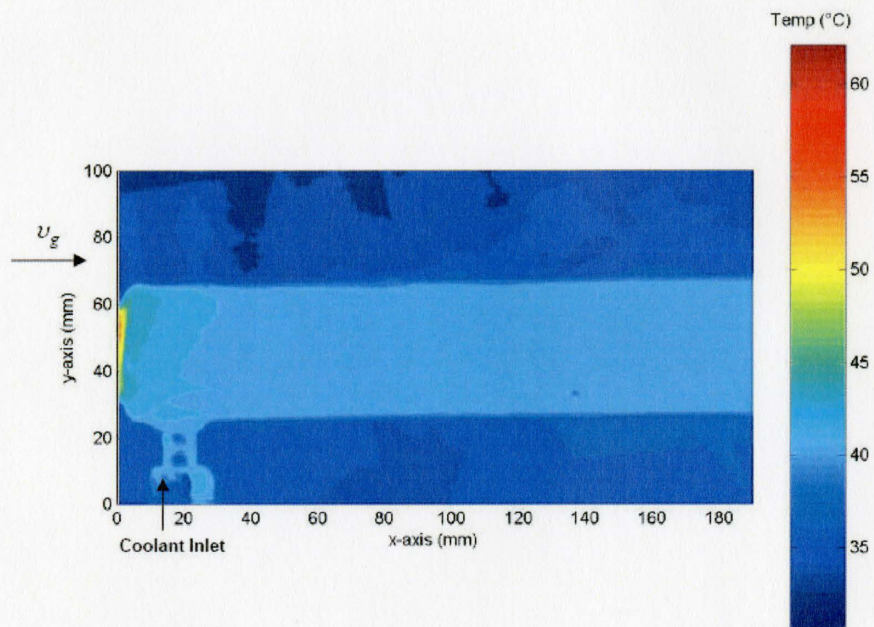


Figure 4.26: Temperature profile of CWCS for 40 °C, 2hr case

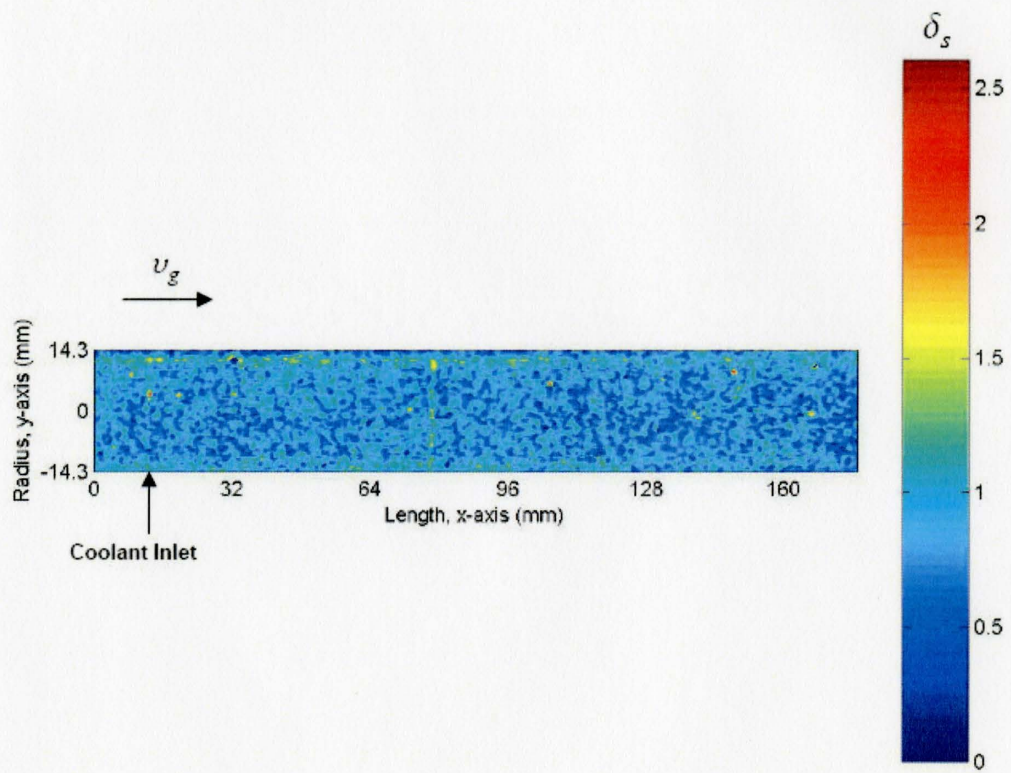


Figure 4.27: Soot deposition profile of CWCS for 40°C, 3hr case; δ_s in mm

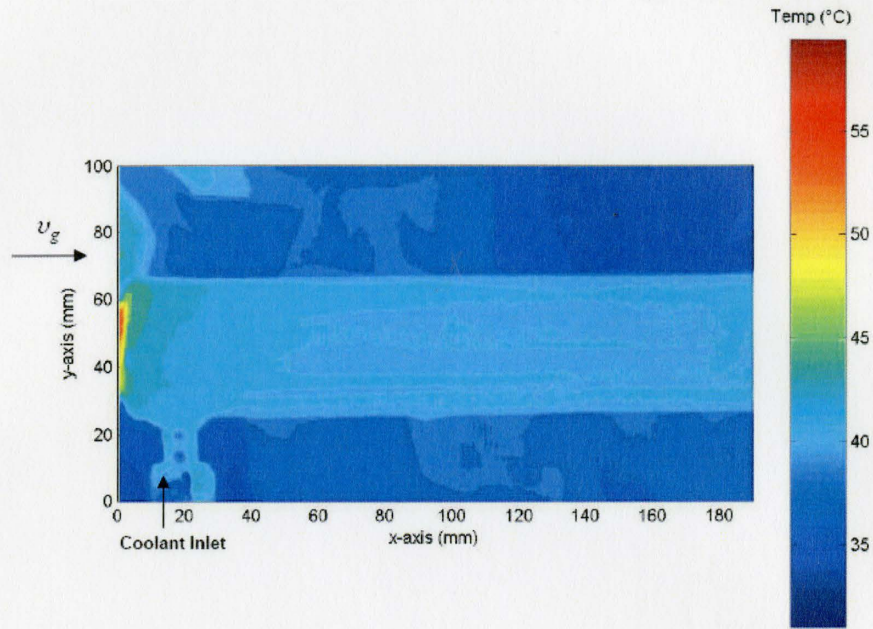


Figure 4.28: Temperature profile of CWCS for 40 °C, 3hr case

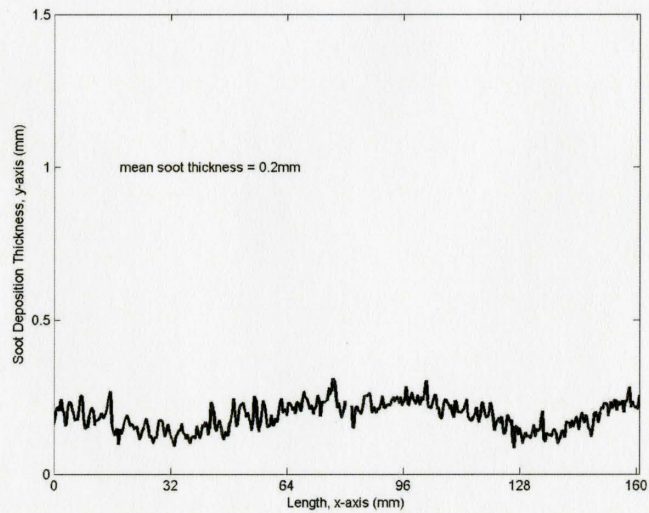


Figure 4.29: Cross-sectional soot deposition thickness average after 1hr operation time and 40 °C coolant temperature, CWCS

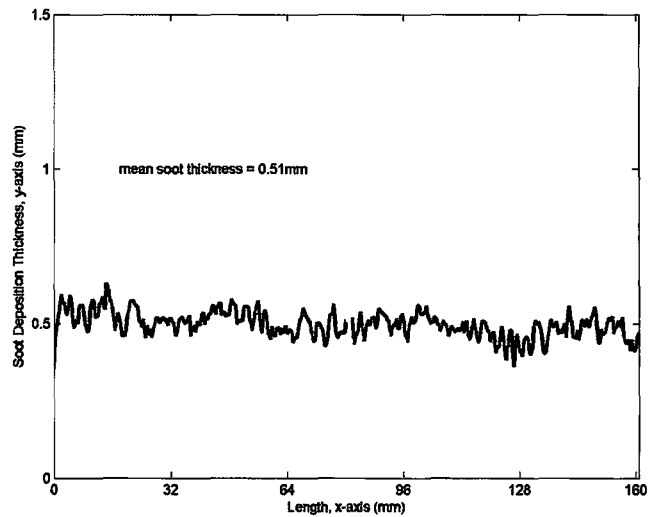


Figure 4.30: Cross-sectional soot deposition thickness average after 2hr operation time and 40 °C coolant temperature, CWCS

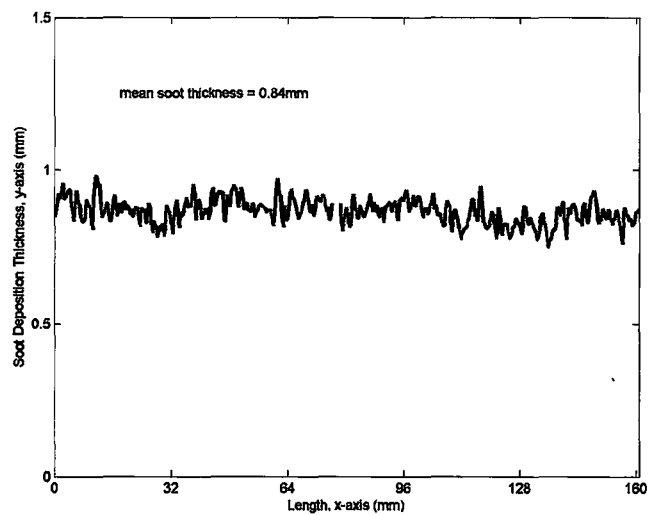


Figure 4.31: Cross-sectional soot deposition thickness average after 3hr operation time and 40 °C coolant temperature, CWCS

For the 3hr exposure time case, Figure 4.27 shows that the soot deposition has increased significantly with a mean deposition thickness of $0.84\pm 0.13\text{mm}$. The soot deposition still remains evenly distributed throughout the length and radius of the CWCS. The cross-sectional average along its x-axis is shown in Figure 4.31, where the wavy pattern is still present but not significant.

4.3.2 Effect of Cooling Temperature on Soot Deposition

Two-dimensional soot deposition profiles as shown in Figures 4.32 and 4.34 for initial coolant temperatures of $20 \pm 3^\circ\text{C}$ and no coolant condition respectively at a fixed exposure time of 2hrs and comparing them to the corresponding typical wall surface temperature distribution profiles as shown in Figures 4.26 and 4.35. It can be observed that there was an increase of deposited soot as the initial coolant temperature decreases. Again note the analyzed regions of the soot deposition profiles and the temperature distribution profiles are 3/4 of the entire region of the device from the upstream entrance as discussed in chapter 3, with gravity pointing down and the gas flow is from left to right.

Two-dimensional soot deposition profiles for the $20\pm 3^\circ\text{C}$ coolant temperature, and 2hr exposure time case, shows that there is a large amount of deposition with a mean soot deposition thickness of $0.82\pm 0.13\text{mm}$ along the entire area, Figure 4.32 shows that the deposited soot is localized along the CWCS. The a cross-sectional average of the soot deposition along its x-axis is shown in Figure 4.36, where a large wavy pattern in the soot deposition is evident in the CWCS along its length, that may be due to re-entrainment of deposited soot. There are no significant qualitative localized soot depositions which may be due to the thermophoretic effects at the coolant inlet, since soot is deposited at random localized sections of the CWCS.

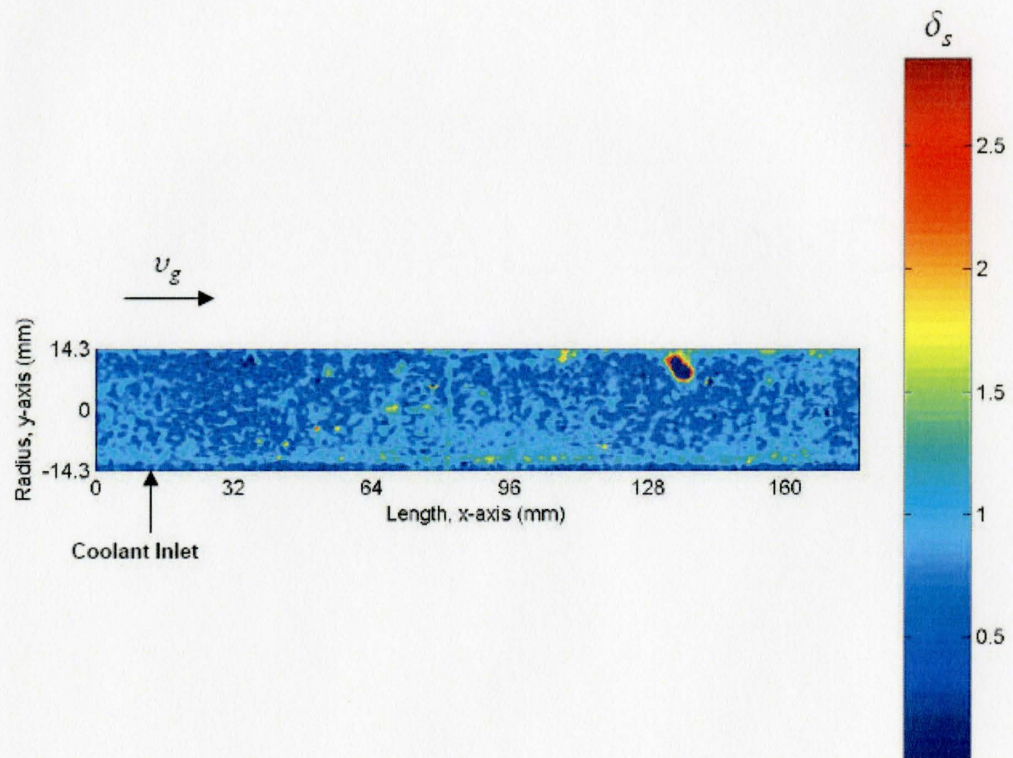


Figure 4.32: Soot deposition profile of CWCS for 20°C, 2hr case; δ_s in mm

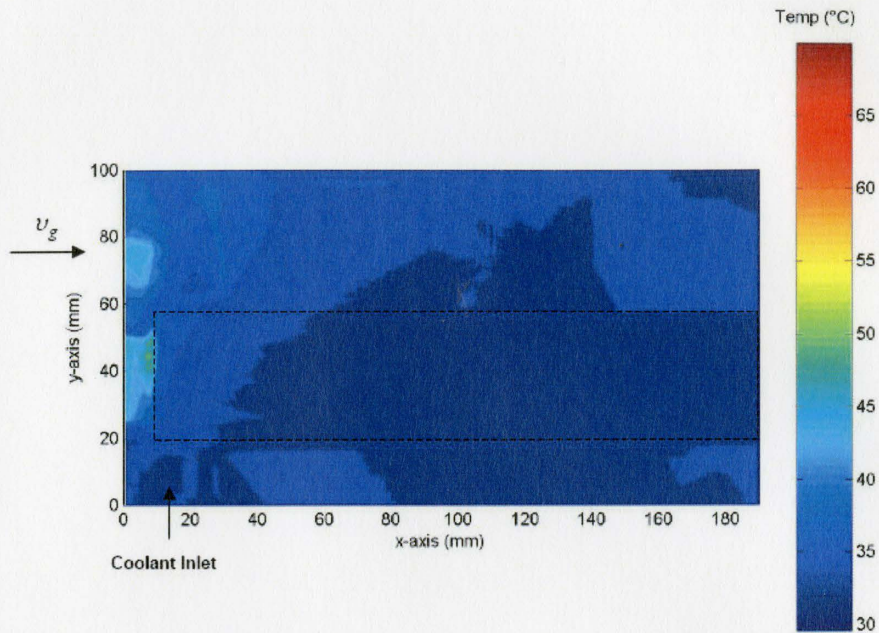


Figure 4.33: Temperature profile of CWCS for 20 °C, 2hr case

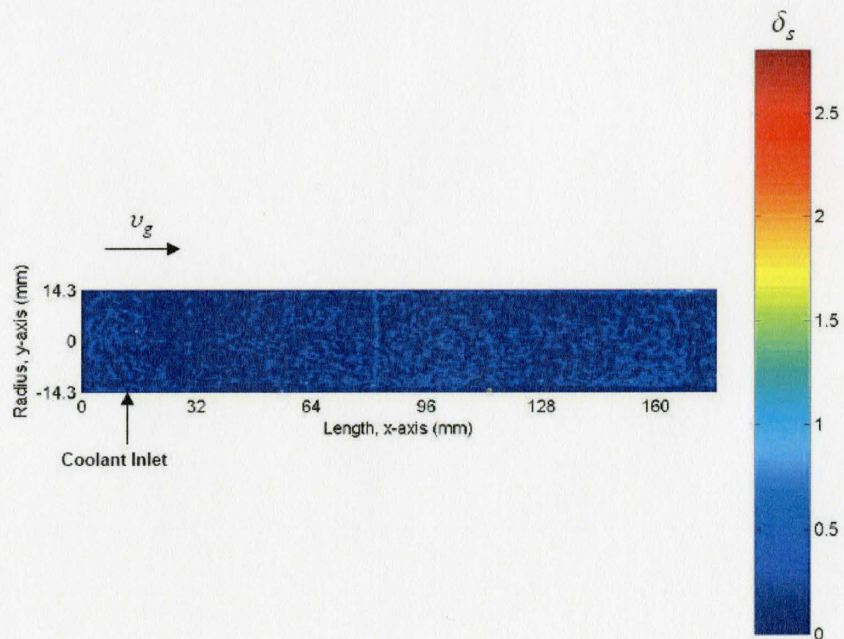


Figure 4.34: Soot deposition profile of CWCS for the no coolant, 2hr case; δ_s in mm

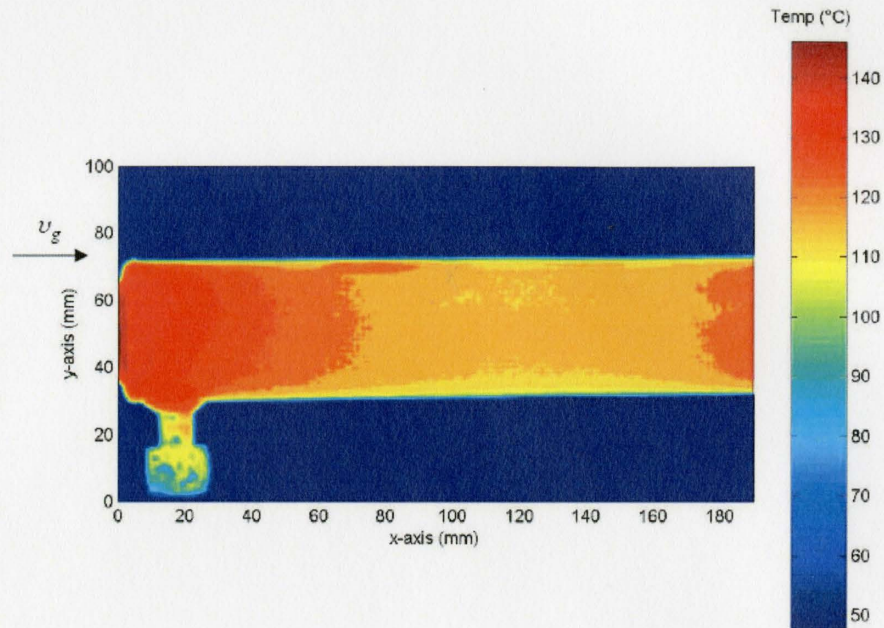


Figure 4.35: Temperature profile of CWCS for the no coolant, 2hr case

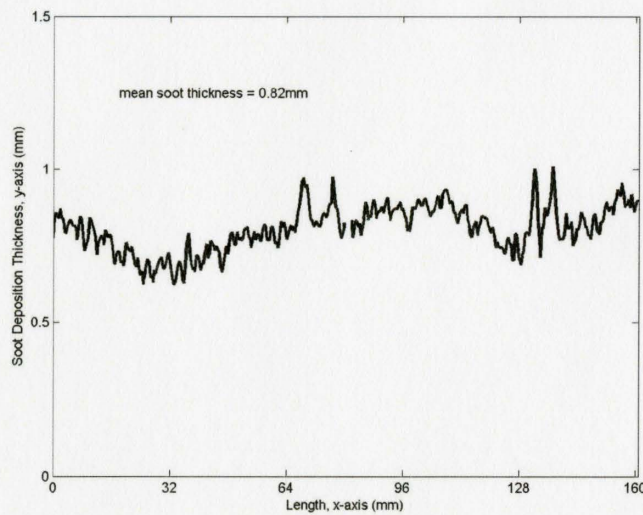


Figure 4.36: Cross-sectional soot deposition thickness average after 2hr operation time and 20 °C coolant temperature, CWCS

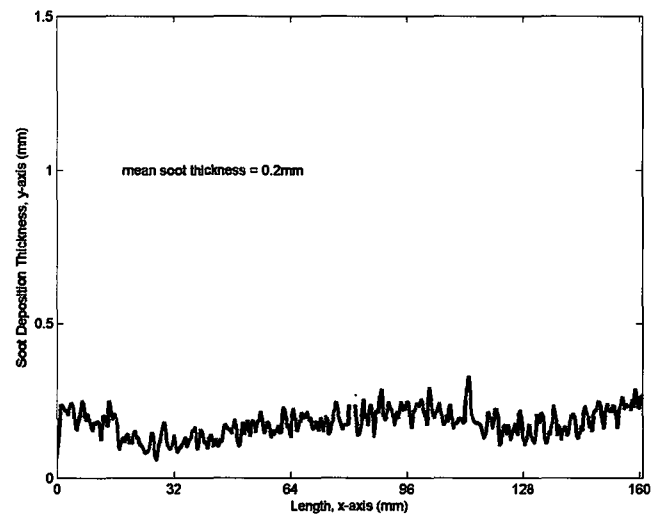


Figure 4.37: Cross-sectional soot deposition thickness average after 2hr operation time with no coolant condition, CWCS

For the $40 \pm 3^\circ\text{C}$ coolant temperature and 2hr exposure time case, Figure 4.25 shows that the amount of soot deposition has significantly increased with exposure time with a mean soot deposition thickness of $0.51 \pm 0.08\text{mm}$ along the entire area of the analysis region. The deposited soot is evenly distributed along the x-axis of the CWCS, with depositions biased on the lower part similarly to section 4.2.2, this may be due to the effects of gravity for coagulated soot. Taking a cross-sectional average of the soot deposition thickness along its x-axis as shown in Figure 4.30, A slight, but not evident wavy pattern in the soot deposition is present, again may be due to re-entrainment of soot, and mechanisms of soot layer adhesion. There are no obvious enhanced localized soot deposition, this may be due to less thermophoretic effects at the coolant inlet, since soot is deposited evenly throughout the CWCS.

For the no coolant condition and 2hr exposure time case as shown in Figure 4.34, it is observed that the soot deposition has decreased to a mean deposition thickness of $0.2 \pm 0.03\text{mm}$ by comparing with present coolant flow. The wall temperature was approximately $126 \pm 3^\circ\text{C}$. The deposition of soot is evenly distributed along the entire area of the CWCS and this may mean that there are no significant gravitational or thermophoretic generated soot depositions. The cross-sectional average soot layer thickness in Figure 4.37 shows that the deposited soot is evenly distributed throughout the length of the CWCS with a slight wavy pattern that may be caused by re-entrainment or adhesion mechanisms.

4.4 Electrical Effects on Soot Deposition

Maricq (2006) shows that diesel soot has a charge upon exiting the combustion chamber, thus an externally applied electrical field may significantly affect soot deposition. In this section, the results of soot deposition on a cylindrical wall cooled

geometry as a function of applied voltage will be investigated and discussed. The inlet water cooling temperature used in this experiment is fixed at $40 \pm 3^\circ\text{C}$. Time averaged discharge current-voltage characteristics for positive and negative polarities are shown in Figure 4.38 for soot free conditions, where corona on-set is 4kV for positive polarity and -10kV for negative polarity. Since only electric field effects are being investigated, only voltages below corona on-set was considered, thus applied voltages of 0kV, -3kV and +3kV are the parameters investigated in this section at an operation time of 2hrs.

Two-dimensional soot deposition profiles for applied voltage are shown in Figures 4.39, 4.40 and 4.41 for $0 \pm 0.1\text{kV}$, $-3 \pm 0.1\text{kV}$ and $+3 \pm 0.1\text{kV}$ respectively. The soot deposition cross-sectional average over the radius of the coaxial cylindrical wall cooled with applied electric field (CCWCSE) is shown in Figures 4.42, 4.43 and 4.44 for $0 \pm 0.1\text{kV}$, $-3 \pm 0.1\text{kV}$ and $+3 \pm 0.1\text{kV}$ respectively. The analyzed region is only the upstream $3/4$ of the entire length of the CCWCSE as mentioned in chapter 3.

By comparing the $0 \pm 0.1\text{kV}$ case with the $40 \pm 3^\circ\text{C}$ 2hr case (Figure 4.25 in section 4.3.2), it can be observed that the mean deposition thickness of $0.50 \pm 0.08\text{mm}$ is consistent and repeatable even with the coaxial wire electrode in the central axis. Here the faint horizontal line present in the soot deposition profile in Figure 4.39 represents deposited soot on the electrode wire. The cross-sectional average soot deposition shows that the deposited soot is evenly distributed throughout the length of the CCWCSE with a subtle wavy pattern.

The soot deposition profile for the $-3 \pm 0.1\text{kV}$ case shows a significant increase in soot deposition with a mean deposition thickness of $0.91 \pm 0.15\text{mm}$, which may be due to a significant applied electric field effect on soot deposition. The deposited soot is evenly distributed throughout the area of the CCWCSE that may be due to the effect of the uniformly distributed applied voltage along the length of the device.

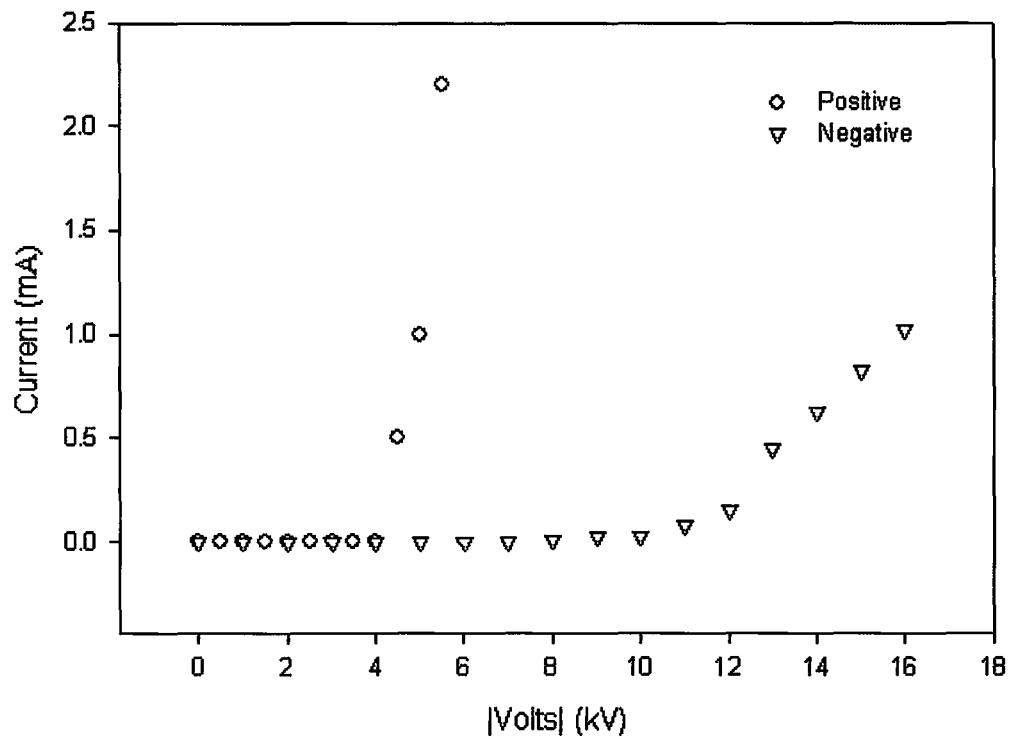


Figure 4.38: Time averaged discharge current and voltage characteristics of the CCWCSE for positive and negative polarities for soot free condition

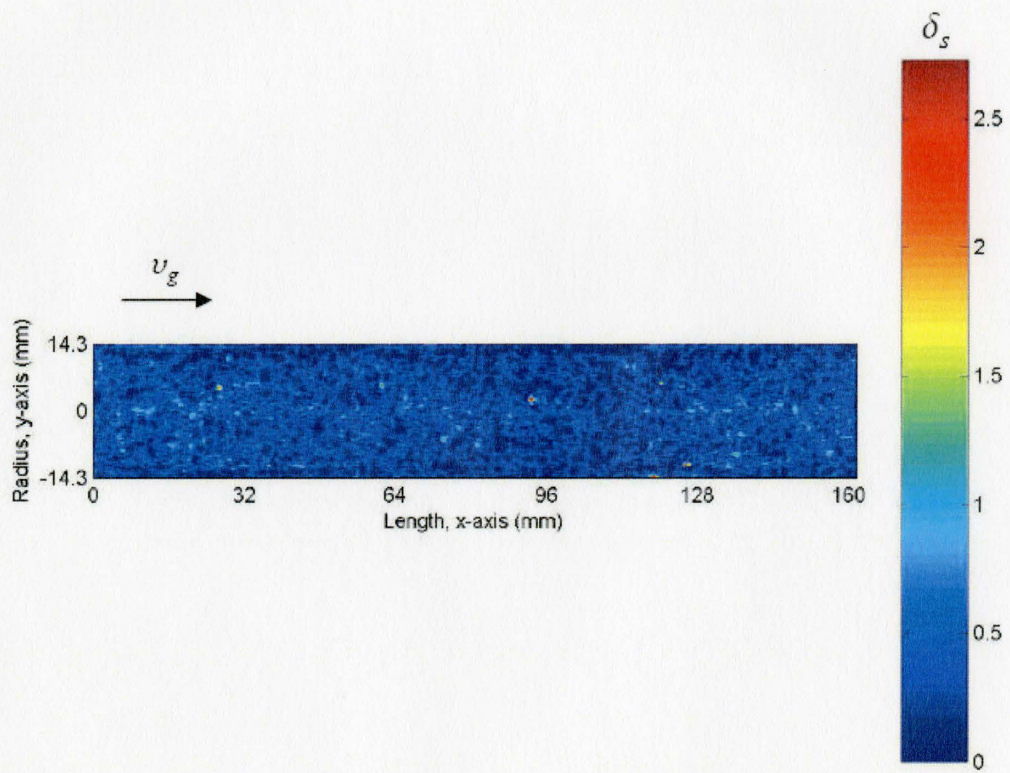


Figure 4.39: Soot deposition profile of CCWCSE for the 0kV case; δ_s in mm

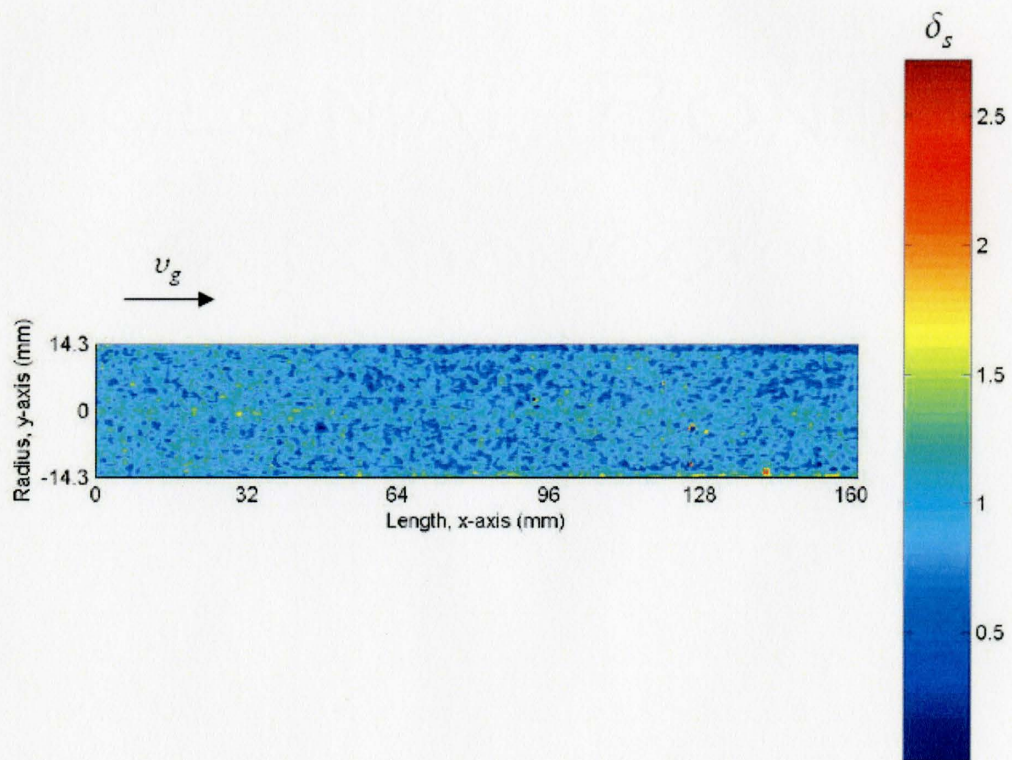


Figure 4.40: Soot deposition profile of CCWCSE for the -3kV case; δ_s in mm

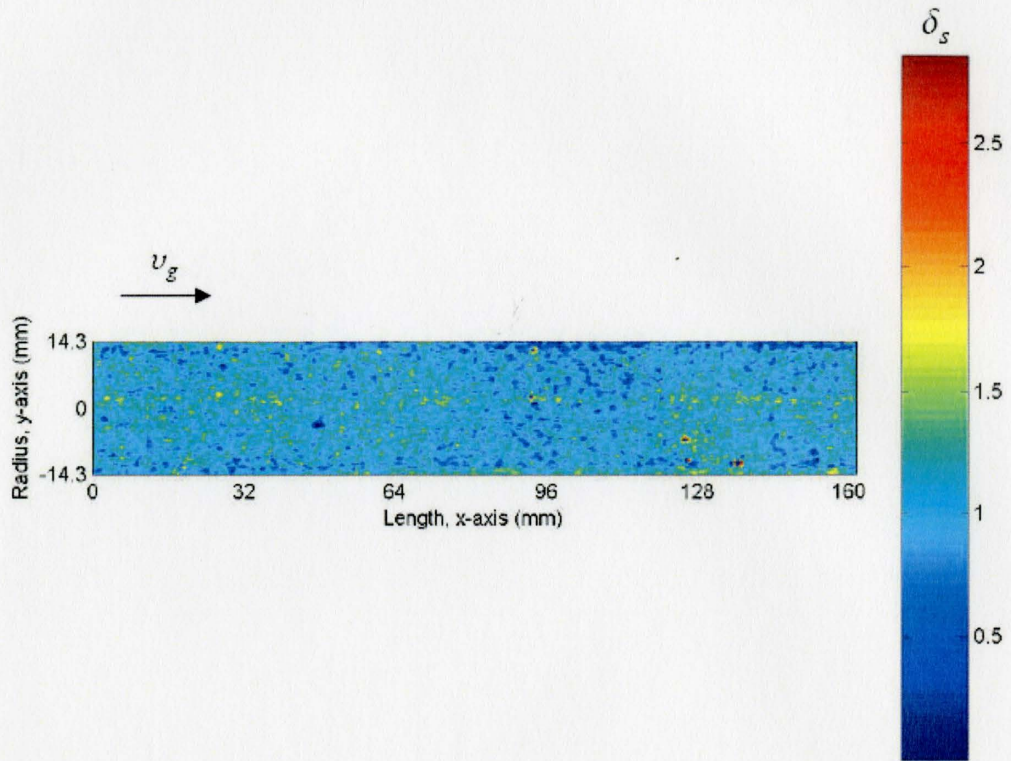


Figure 4.41: Soot deposition profile of CCWCSE for the +3kV case; δ_s in mm

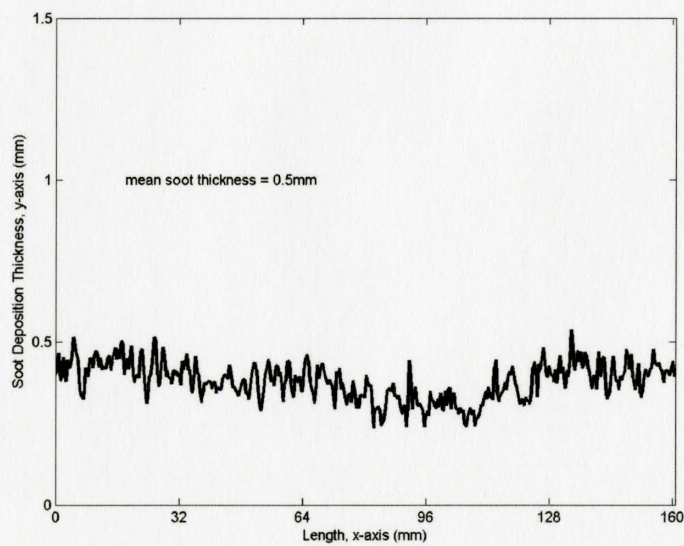


Figure 4.42: Cross-sectional average of soot deposition profile for 0kV case, CCWCSE

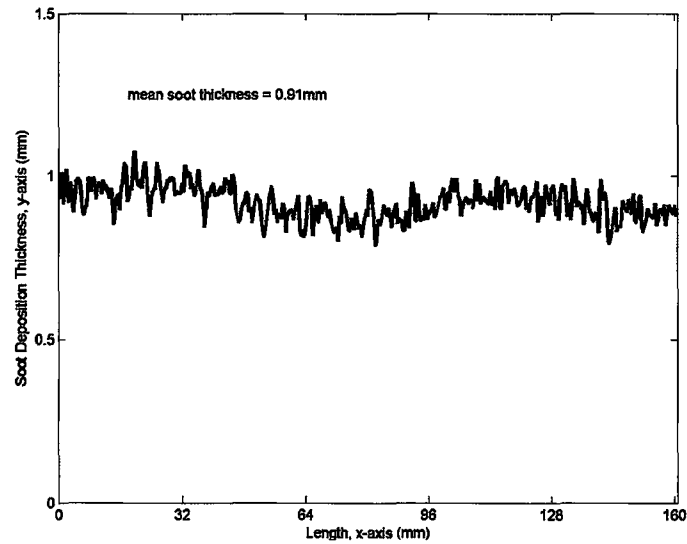


Figure 4.43: Cross-sectional average of soot deposition profile for -3kV case, CCWCSE

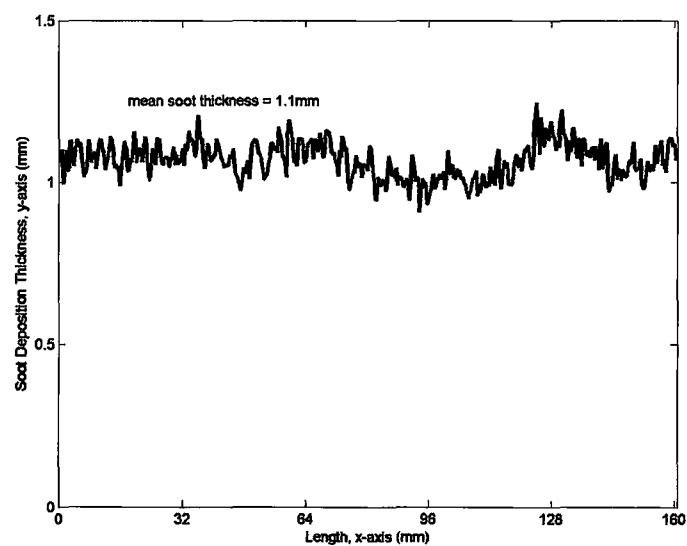


Figure 4.44: Cross-sectional average of soot deposition profile for +3kV case, CCWCSE

The deposition of the electrode wire is present and observed by the horizontal line in the deposition profile, this deposition may be caused by the positively charged soot depositing on the electrode. Looking at the cross-sectional average soot deposition profiles, there is a slight, but more evident wavy pattern again is present. This wavy pattern may be caused by re-entrainment of deposited soot, or since this wavy pattern was not as evident at this level of soot deposition, could possibly be caused by an uneven distribution of the electric field along the length of the electrode wire after the soot has deposited.

In the $+3\pm 0.1\text{kV}$ case, it can be observed that a similar soot deposition profile compared to the -3kV case, including the mean deposited soot thickness of $1.1\pm 0.18\text{mm}$. This suggests that there is a slight significant polarizing effect between positively and negatively charged particles in the exhaust gas. The soot covered wire electrode is again present at the centre of x-axis of the CCWCSE. There is a slight wavy pattern, but not as evident as the -3kV case that may be due to a non-uniformly distributed electric field along the length of the device, also there is a localized increase in soot deposition thickness at the $x = 128\text{mm}$ from the cross sectional average, this could be caused again by soot layer re-entrainment or an uneven distribution of the electric field.

4.5 Comparison with Deposition Models

Comparisons of the CWCS experimental results with the modified transport model of Chang (1987) was conducted, where the model was based on convection, diffusion, thermophoresis and electric field effects as shown in equation 4.1.

$$\underline{U}_g \nabla N \pm \mu_s \nabla N \cdot \underline{E} \pm \mu_s \nabla N \cdot \underline{E} - G_s N_s \nabla T_g = 0 \quad (4.1)$$

The same parameters used in the experimental results (20°C, 2hr case) as shown in Table 4.1 were utilized to calculate numerically from the solution of equation 4.1 by assuming ideal plug flow ($U_g = const$), uniform radial electric ($E = const$) and temperature gradient ($\nabla T \approx (T - T_o)/D_s = const$) profiles with no space charge ($E = V/D_s$) effects, similar to Chang (1987) as follows:

$$\frac{N}{N_o} = J_o(r/D_s) \exp \left\{ \frac{U_g \pm \mu_s \cdot E}{2D_s} - \left[\left(\frac{U_g \pm \mu_s \cdot E}{2D_s} \right)^2 + \frac{G_s N_s (T - T_o)}{D_s R_t} + \frac{2.405^2}{R_t} \right]^{1/2} \right\} Z \quad (4.2)$$

The experimental result for the 20°C case normalized by the inlet number density as shown in Figure 4.45, where numerical values based on modified Chang's model also shown in this figure for comparison. The profile based on the model considers convection, diffusion, thermophoresis and electric field effects, U , D , σ and E respectively, the second profile neglects electric field effects, and the third profile neglects thermophoresis and electric field effects. It can be observed from the numerical results that as each effect are compounded, the soot deposition efficiency of the CWCS increases, however the model does not correlate with present experimental data, since the even distribution of soot deposition along the length of the CWCS may be due to re-entrainment and a combination of dense and dilute flow interaction.

4.6 Summary

The results of operation time, temperature and electric field effects on mean soot deposition are summarized in Figures 4.46, 4.47 and 4.48 respectively. It is observed in Figure 4.46 that as operation time increased, the mean soot deposition also increased non-linearly. Figure 4.47 shows that there is a significant effect of

Table 4.1: Experimental parameters implemented in numerical solution

Parameter	Value
U_g	7.2 [m/sec]
R_t	14.3 [mm]
μ_s	2.72×10^{-7} [m ² /sec·volt]
N_s	1.0×10^8 [# /m ³]
E	2.1×10^5 [V/m]
D_{Re}	1.2×10^{-8} [m ² /s]
G_p	1.4×10^{-8}
$(T - T_o)$	210 [°C]

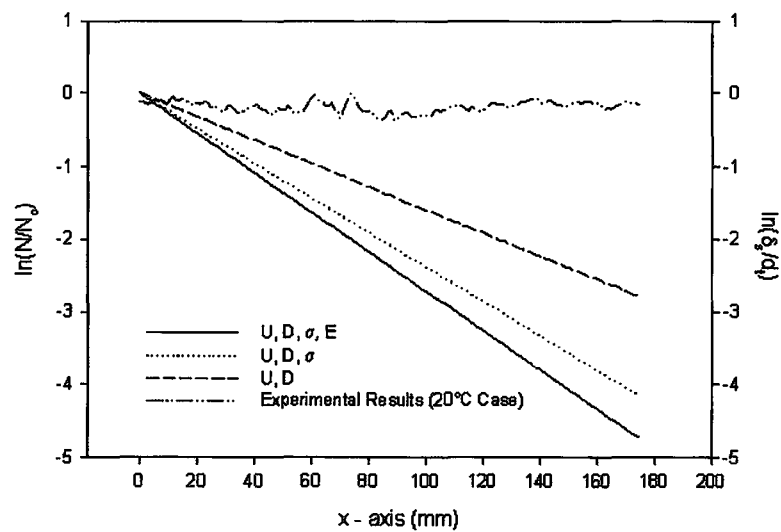


Figure 4.45: Experimental results compared with modified Chang's model

initial cooling temperature in the first 180 minutes of operation having an increase of almost 400% as the initial coolant temperature approaches $20 \pm 3^\circ\text{C}$. However as the coolant temperature approaches zero degrees as observed in the present experiment at coolant temperature at 10°C , there are more mechanisms involved in deposition and re-entrainment due to water condensation. For electric field effects, it also shows that there was a significant effect of electric field on soot deposition, achieving a 182 to 220% increase as a negative and positive 3kV, respectively was applied. More interestingly, there was a similar deposition behaviour between positive and negative polarities that may be due to a near even distribution of positive and negative charged particles.

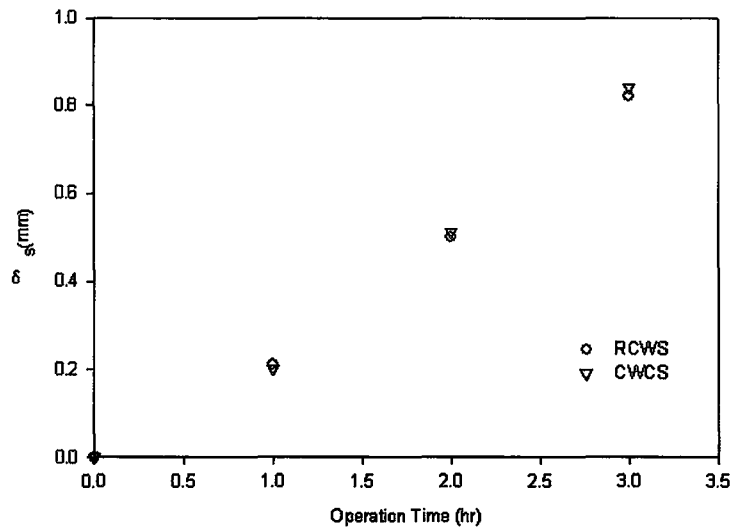


Figure 4.46: Mean soot deposition thickness as a function of operation time for RWCS and CWCS

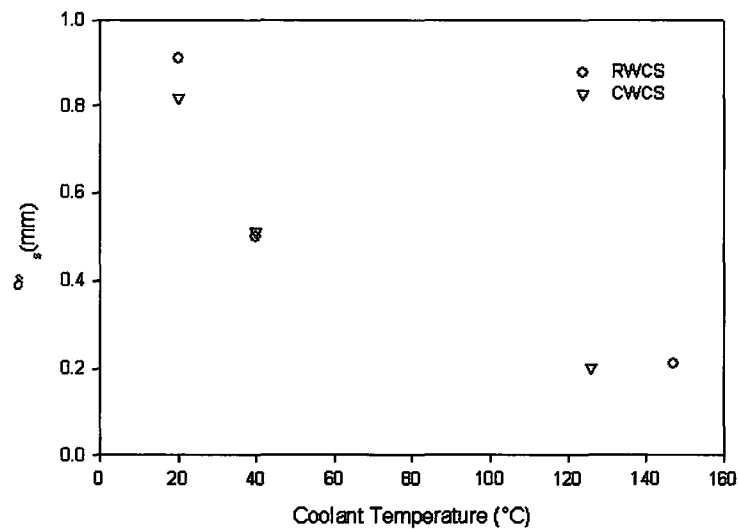


Figure 4.47: Mean soot deposition thickness as a function of initial inlet coolant temperature for RWCS and CWCS

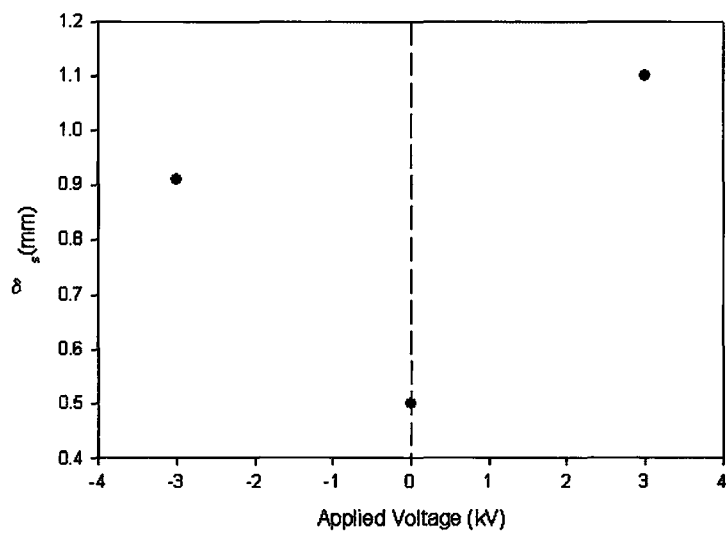


Figure 4.48: Mean soot deposition thickness as a function of applied voltage for CCWCSE

Chapter 5

Conclusions

The effect of convection, diffusion, thermophoresis and electric field on soot deposition using a Real-Time Neutron Radiography technique was investigated for three devices; a rectangular wall cooled section(RWCS); a cylindrical wall cooled section(CWCS) and a coaxial cylindrical wall cooled section with applied electric field(CCWCSE). Three parameters investigated; coolant temperature, operation time and applied voltage at a fixed exhaust gas mass flow rate of 20kg/hr resulting in a Reynolds number of 6300 and 9000 for the rectangular and cylindrical wall cooled sections respectively and the following conclusions were made:

- The effect of thermophoresis on soot deposition in the RWCS was investigated by changing the initial water coolant temperature from 20°C, 40°C and no coolant. The results show that as cooling temperature increased, the mean soot deposition thickness decreased non-linearly, with deposition rate of -2.05mm/°C from 20°C to 40°C and -0.27mm/°C from 40°C to 147°C. From the soot deposition distribution, it could be observed that soot deposition was more evident near the coolant inlet of the device with the soot deposition profile pattern matching the coolant temperature profile, that is, more deposition at

the cooler regions, as shown in the higher 40°C coolant temperature case. This same pattern could also be observed in the lower 20°C coolant temperature case, however, soot has become more evenly distributed through out the device, but there are still localized depositions at the entrance and near the coolant inlet. For the no coolant case, the soot distribution is more uniformly distributed and is more symmetrical, that is, there is no deposition bias towards the inlet of the coolant, this suggests that the localized deposition near the coolant inlet was dominated by the thermophoretic effect.

- The effect of thermophoresis on soot deposition in the CWCS was investigated by changing the coolant temperature from 20°C, 40°C and no coolant. Similarly to the RWCS, that as the cooling temperature increased, the mean soot deposition thickness decreased, with deposition rate of -1.55mm/°C from 20°C to 40°C and -0.36mm/°C from 40°C to 126°C. Compared to the RWCS, it can also be observed that there are no localized deposition in the CWCS, this could be caused by the nature of the coolant flow, where there were large secondary coolant flows (seen in appendix B) in the RWCS causing localized hot regions, therefore decreasing the temperature gradient, where in the CWCS, the main coolant flow causes the coolant to flow in one direction from the inlet to the exit, causing a more uniformly distributed cooling temperature in the CWCS.
- The effect of diesel operation length on soot deposition in both the CWCS and the RWCS were investigated by systematically exposing the sections to the exhaust gas from 1 to 3hrs. It can be observed that for both devices, as operating time increased, mean soot deposition increased almost linearly, with a mean deposition rate of 0.29mm/hr from 1hr to 2hrs and 0.32mm/hr from 2hrs to 3hrs. However a linear proportion cannot be assumed since this could be a

part of a transient, and the soot deposition thickness as a function of operation time could reach a steady state.

- Both the CWCS and RWCS achieved similar mean soot deposition thicknesses as a function of time, since the PM number concentration/density and temperature gradient were similar for both devices under a turbulent regime.
- The effect of applied electric field on soot deposition for the CCWCSE was investigated by applying an external electric field below corona on-set voltage for both positive and negative applied voltages. It was observed that the soot deposition increased with an increase of applied voltage for both positive and negative voltages, where the positive applied voltage shows higher mean soot deposition layer compared to negative applied voltage (polarity effects).

Chapter 6

Recommendations for Future Work

Based on the present study, it can be recommended for future work for analysis of deposition initiation, charge measurement of soot and deposition and an analysis of soot deposition using 3-dimensional reconstruction analysis.

It could be observed from the thermophoretic effects on soot deposition for the rectangular wall cooled section(RWCS) that there were localized regions of high soot deposition present, particularly in the cooler regions of the RWCS. It can be suggested that initial deposition can be highly dependant on cooling temperature as found in this study, thus an analysis of deposition initiation and adhesion mechanisms could be important for soot deposition analysis.

Since, there was a significant effect on soot deposition by applying an external electric field, it could be beneficial to have known the charge distribution of soot in diesel exhaust for various parameters and operating conditions. Also a study could be considered for determining the cause of and source of the soot electrically charging. It could also be beneficial to quantify the charge of each soot particle such that future soot deposition models could incorporate localized electric field caused by deposited soot.

The current method used in this study was a 2-dimensional analysis of the deposited soot, since, 2-dimensional neutron radiography does not differentiate z-position (i.e. axis in parallel to the neutron beam) it would be beneficial to develop a 3-dimensional Real-Time Neutron Radiography system, such that more complex geometries could be analyzed.

References

- G. H. Abd-Alla. Using exhaust gas recirculation in internal combustion engines: A review. *Energy Conversion and Management*, 43(8):1027–1042, 2002.
- U. Adler, H. Bauer, and R. Bosch. *Automotive Handbook*. Robert-Bosch-GmbH, Stuttgart, 3rd edition, 1993.
- G. K. Batchelor and C. Shen. Thermophoretic deposition of particles in gas flowing over cold surfaces. *Journal of Colloid and Interface Science*, 107(1):21–37, 1985.
- T. G. Beuthe and J. S. Chang. *Gas Discharge Phenomena*, chapter 9. Handbook of Electrostatic Processes. Marcel Dekker Inc., New York, 1995.
- D. Brocilo, J. S. Chang, R. D. Findlay, Y. Kawada, and T. Ito. Modelling of the effect of electrode geometries on the corona discharge current-voltage characteristic for wire-plate electrostatic precipitators. *Annual Report of CEIDP*, pages 681–684, 2001.
- R. L. Byers and S. Calvert. Particle deposition from turbulent streams by means of thermal force. *Industrial and Engineering Chemistry Fundamentals*, 8:646, 1969.
- J. S. Chang. The effects of space charge density on the aerosol particle collection efficiency in co-flow type electrostatic packed bed filters. *Journal of Aerosol Science*, 18(6):861–864, 1987.
- J. S. Chang. Recommended international standard for dimensionless parameters used in electrohydrodynamics. *IEEE Trans, DEI*, 10:3–6, 2003.
- J. S. Chang and E. C. Morola. Determination of two-phase interfacial areas by an ultrasonic technique. *Nuclear Engineering and Design*, 122:143–156, 1990.
- J. M. Desantes, V. Bermudez, J. M. Garcia, and E. Fuentes. Effects of current engine strategies on the exhaust aerosol particle size distribution from a heavy-duty diesel engine. *Journal of Aerosol Science*, 36(10):1251–1276, 2005.
- R. Detels, D. P. Tashkin, J. W. Sayre, S. N. Rokaw, F. J. Massy, A. H. Coulson, and D. H. Wegman. The ucla population studies of cord: X. a cohort study of

- changes in respiratory function associated with chronic exposure to sox, nox, and hydrocarbons. *American Journal of Public Health*, 81(3):350–359, 1991.
- J. J. Duderstadt and L. J. Hamilton. *Nuclear Reactor Analysis*. John Wiley and Sons, New York, 1996.
- D. Ewing, F. Charles, and J. Colenbrander. Diesel emission characterization and micro dilution tunnel. In J. S. Chang, editor, *Diesel and Micro-Gas Turbine Integrated Electrostatics/Non-Thermal Plasma Emission Controls*, June 8, 2004.
- G. D. Harvel and J. S. Chang. Determination of time-dependent void fraction distribution in bubbly two-phase flow by a real-time neutron radiography technique. *Nuclear Technology*, 109(1):132–141, 1995.
- W. C. Hinds. *Aerosol Technology*. Addison-Wesley, New York, 1982.
- D. B. Ingham. Diffusion of aerosols from a stream flowing through a cylindrical tube. *Journal of Aerosol Science*, 6:125–132, 1975.
- B. Ismail, D. Ewing, J. S. Chang, and J. S. Cotton. Development of a non-destructive radiography technique to measure the three-dimensional soot deposition profiles in diesel engine exhaust systems. *Journal of Aerosol Science*, 35:1275–1288, 2004a.
- B. Ismail, D. Ewing, J. S. Cotton, and J. S. Chang. Characterization of the soot deposition profiles in diesel exhaust gas recirculation cooling devices using a digital neutron radiography imaging technique. *SAE Paper*, 04ANNUAL-324, 2004b.
- T. Johnson. Diesel emission control - 2003 in review. *SAE Technical Paper*, 2004-01-0070, 2004.
- R. Keonigsdorff and J. Werther. Gas-solids mixing and flow structure modeling of the upper dilute zone of a circulating fluidized bed. *Powder Technology*, 82(3):317–329, 1995.
- A. Khaial, G. D. Harvel, and J. S. Chang. Neutron transport characteristics of a nuclear reactor based dynamic neutron imaging system. *Proceeding of ICONE 14*, 2006.
- D. Kim, M. Gautam, and D. Gera. Parametric studies on the formation of diesel particulate matter via nucleation and coagulation modes. *Journal of Aerosol Science*, 33(12):1609–1621, 2002.
- D. B. Kittelson. Engines and nanon particles - a review. *Journal of Aerosol Science*, 29(5):575–588, 1998.

- D. B. Kittelson, J. Reinertsen, and J. Michalski. Further studies of electrostatic collection and agglomeration of diesel particles. *SAE Technical Paper*, 910329, 1991.
- M. M. Maricq. On the electrical charge of motor vehicle exhaust particles. *Journal of Aerosol Science*, 37(7):858–874, 2006.
- D. J. Mason and A. Levy. A model for non-suspension gas-solids flow of fine powders in pipes. *Journal of Multiphase Flow*, 27:415–435, 2001.
- A. Messerer, R. Nierssner, and U. Poschl. Thermophoretic deposition of soot aerosol particles under experimental conditions relevant for moder diesel engine exhaust gas systems. *Journal of Aerosol Science*, 34(8):1009–1021, 2003.
- Z. Ning, C. S. Cheung, and S. X. Liu. Experimental investigation of the effect of exhaust gas cooling on diesel particulate. *Journal of Aerosol Science*, 35(3):333–345, 2004.
- G. Nishio, S. Kitani, and K. Takahashi. Thermophoretic deposition of aerosol particles in a heat-exchanger pipe. *Ind. Eng. Chem*, 13(4):408, 1974.
- S. Ornektekin. Effect of exhaust gas on corrosion of metals. *International Journal of Enviromental Studies*, 55(3):199–210, 1998.
- C. A. Pope, R. T. Burnett, M. J. Thun, E. E. Calle, D. Krewski, K. Ito, and G. D. Thurston. Lung cancer, cardiopulmonary mortality, and long -term exposure to fine particulate air pollution. *Journal of the American Medical Association*, 287(9): 1132–1141, 2002.
- F. J. Romay, S. S. Takagaki, D. Y. H. Pui, and B. Y. H. Liu. Thermophoretic deposition of aerosol particles in turbulent pipe flow - microspheres in air. *Journal of Aerosol Science*, 29(8):943–959, 1998.
- R. Schulte-Braucks. Emission standards for heavy duty vehicles. In *Heavy Duty Diesel Emissions Control Symposium*, Sept. 21, 2005.
- D. Schwela and O. Zali. *Urban Traffic Pollution*. Routledge, New York, 1999.
- H. B. Servati, S. Petreanu, S. E. Marshall, H. Su, R. Marshall, C. H. Wu, K. Hughes, L. Simons, L. Berrimann, J. Zabsky, T. Gomulka, F. Rinaldi, M. Tynan, J. Salem, and J. Joyner. A nox reduction solution for retrofit applications: A simple urea scr technology. *SAE Technical Paper*, 2005-01-1857, 2005.
- S. L. Soo. *Fluid Dynamics of Multiphase Flows*. Blaisdell Pub Co., Waltham, MA, 1967.

- F. Stratmann, E. Otto, and H. Fissan. Thermophoretic and diffusional particle transport in cooled laminar tube flow. *Journal of Aerosol Science*, 25(7):1359–1365, 1994.
- L. Talbot, R. K. Cheng, R. W. Schefer, and D. R. Willis. Thermophoresis of particles in a heated boundary layer. *Journal of Fluid Mechanics*, 101:737–758, 1980.
- C. W. Tan and C. J. Hsu. Diffusion of aerosols in laminar flow in a cylindrical tube. *Journal of Aerosol Science*, 2:117–124, 1971.
- D. B. Taulbee and C. P. Yu. Aerosol flow in rectangular channels. *Journal of Aerosol Science*, 6:433, 1975.
- D. R. Tree and J. E. Dec. Extinction measurements of in-cylinder soot deposition in a heavy-duty direct injection diesel engine. *SAE Technical Paper*, 2001-01-1296, 2001.
- L. Waldmann and K. H. Schmitt. *Thermophoresis and Diffusiophoresis of Aerosols*, chapter 6. Aerosol Science. Academic Press, London, 1966.
- B. L. Wesborg, J. B. Howard, and G. C. Williams. Physical mechanisms in carbon formation in flames. *Proceeding of 14th Symposium on Combustion*, pages 929–940, 1973.
- K. T. Whitby and Y. H. Liu. *The Electrical Behaviour of Aerosols*, chapter 3. Aerosol Science. Academic Press, London, 1966.
- H. J. White. *Industrial Electrostatic Precipitation*. Addison-Wesley, Reading, MA, 1963.
- R. Zhang, F. Charles, D. Ewing, J. S. Chang, and J. S. Cotton. Effect of diesel soot deposition on the performance of exhaust gas recirculation cooling devices. *SAE Paper*, 2004-01-0122, 2004.
- M. Zheng, G. T. Reader, and J. G. Hawley. Diesel engine exhaust gas recirculation - a review on advanced and novel concepts. *Energy Conversion and Management*, 45:883–900, 2004.
- A. Zukeran, P. C. Looy, A. Chakrabati, A. A. Berezin, S. Jayaram, J. Cross, T. Ito, and J. S. Chang. Collection efficiency of ultrafine particles by an electrostatic precipitator under dc and pulse operating modes. *IEEE Transactions on Industry Applications*, 35(5):1184–1191, 1999.

Appendix A

Venturi Calibration Curves

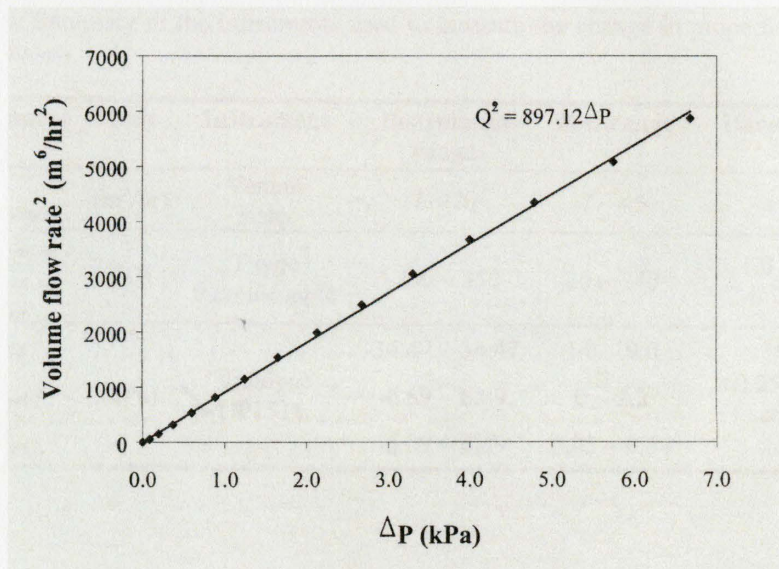


Figure A.1: Calibration curve of venturi flow meter I as a function of ΔP

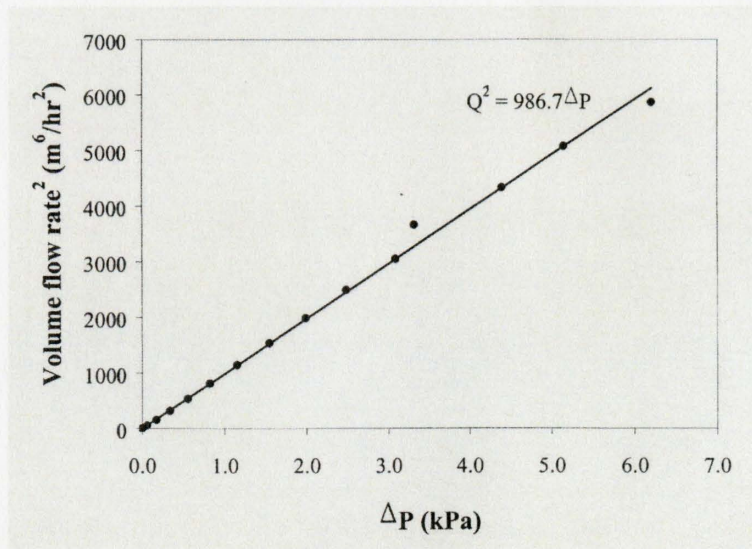


Figure A.2: Calibration curve of venturi flow meter II as a function of ΔP

Appendix B

Real-Time Neutron Radiography Images of the Cooled Sections

This appendix will show the unprocessed and rotated Real-Time Neutron Radiography (RTNR) images of the rectangular wall cooled section (RWCS) and the cylindrical wall cooled section (CWCS).

B.1 Rectangular Wall Cooled Section

The series of unprocessed RTNR images shows the RWCS being rotated every 30 degrees from 0 to 90 degrees with and without water in the coolant chambers.

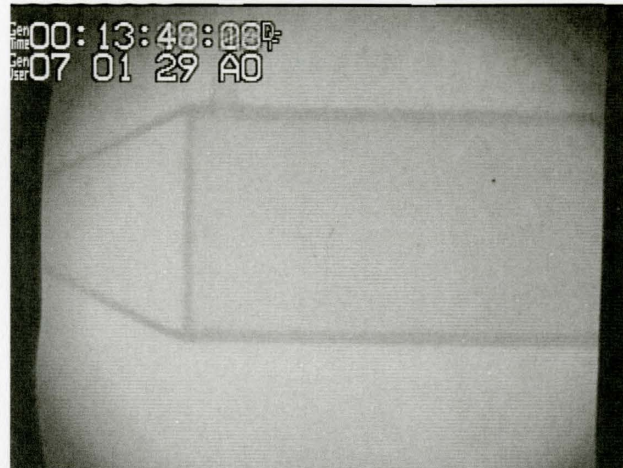


Figure B.1: Unprocessed RTNR image of the RWCS exposed to diesel exhaust gas for 2 hrs at an initial coolant temperature of 20 degrees celcius, 0 degrees rotation, without water

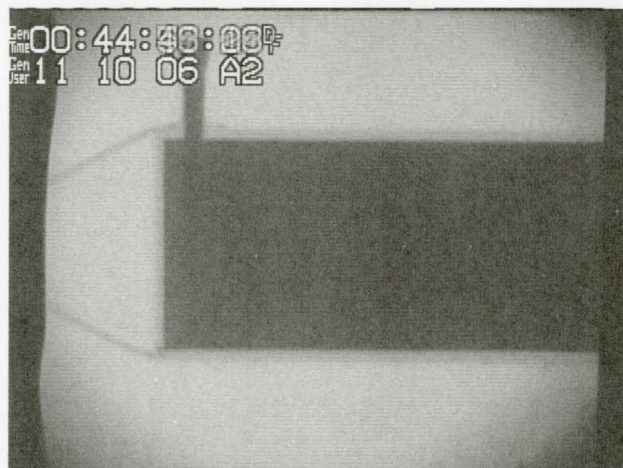


Figure B.2: Unprocessed RTNR image of the RWCS exposed to diesel exhaust gas for 2 hrs at an initial coolant temperature of 20 degrees celcius, 0 degrees rotation, with water



Figure B.3: Unprocessed RTNR image of the RWCS exposed to diesel exhaust gas for 2 hrs at an initial coolant temperature of 20 degrees celcius, 30 degrees rotation, without water

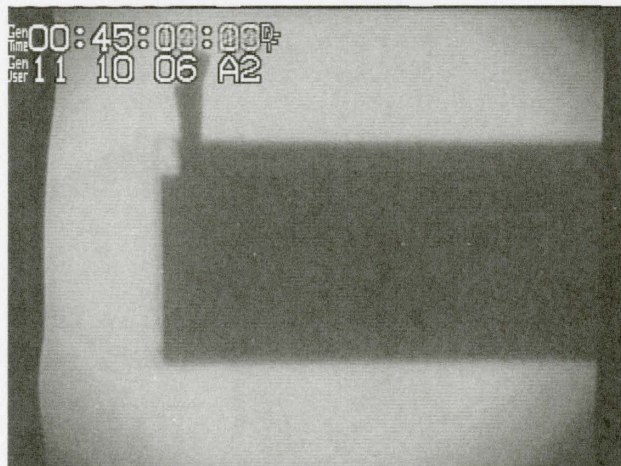


Figure B.4: Unprocessed RTNR image of the RWCS exposed to diesel exhaust gas for 2 hrs at an initial coolant temperature of 20 degrees celcius, 30 degrees rotation, with water



Figure B.5: Unprocessed RTNR image of the RWCS exposed to diesel exhaust gas for 2 hrs at an initial coolant temperature of 20 degrees celcius, 60 degrees rotation, without water

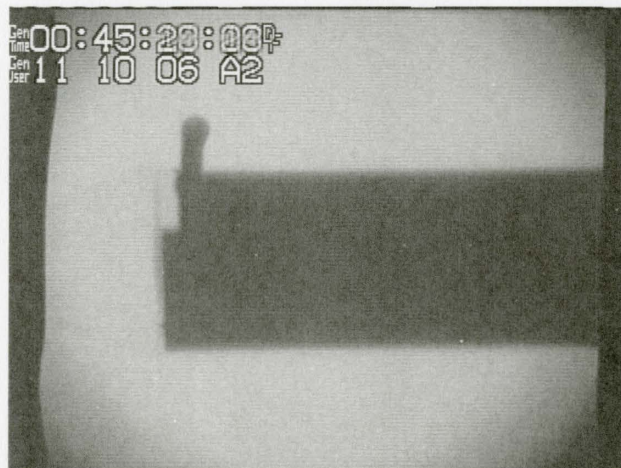


Figure B.6: Unprocessed RTNR image of the RWCS exposed to diesel exhaust gas for 2 hrs at an initial coolant temperature of 20 degrees celcius, 60 degrees rotation, with water

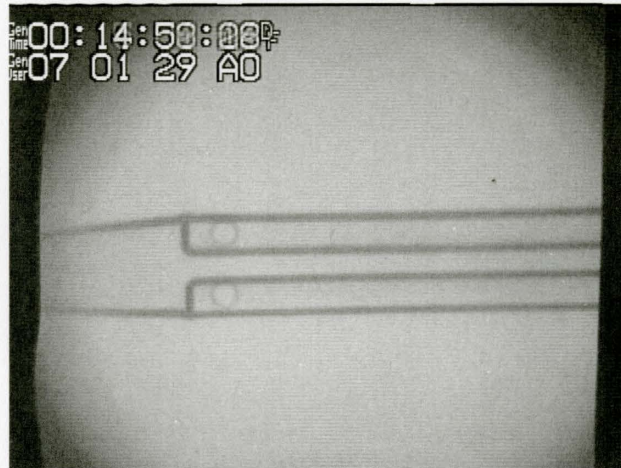


Figure B.7: Unprocessed RTNR image of the RWCS exposed to diesel exhaust gas for 2 hrs at an initial coolant temperature of 20 degrees celcius, 90 degrees rotation, without water

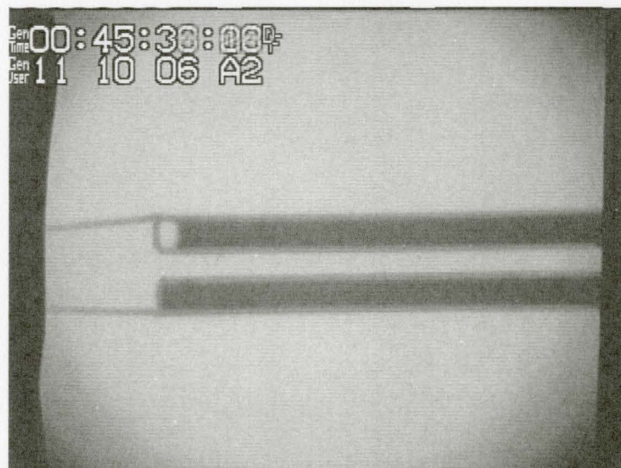


Figure B.8: Unprocessed RTNR image of the RWCS exposed to diesel exhaust gas for 2 hrs at an initial coolant temperature of 20 degrees celcius, 90 degrees rotation, with water

B.2 Cylindrical Wall Cooled Section

The series of unprocessed RTNR images shows the CWCS being rotated every 90 degrees from 0 to 90 degrees, without water in coolant chamber.



Figure B.9: Unprocessed RTNR image of the CWCS exposed to diesel exhaust gas for 2 hrs at an initial coolant temperature of 20 degrees celcius, 0 degrees rotation, without water



Figure B.10: Unprocessed RTNR image of the CWCS exposed to diesel exhaust gas for 2 hrs at an initial coolant temperature of 20 degrees celcius, 90 degrees rotation, without water

Appendix C

Digital Images of Soot Inside the Cylindrical Wall Cooled Section



Figure C.1: Digital image of the top portion inside the CWCS gas channel at upstream exposed to diesel exhaust gas for 2 hrs at an initial coolant temperature of 20 degrees celcius



Figure C.2: Digital image bottom of the portion inside the CWCS gas channel at upstream exposed to diesel exhaust gas for 2 hrs at an initial coolant temperature of 20 degrees celcius



Figure C.3: Digital image of the top portion inside the CWCS gas channel at downstream exposed to diesel exhaust gas for 2 hrs at an initial coolant temperature of 20 degrees celcius

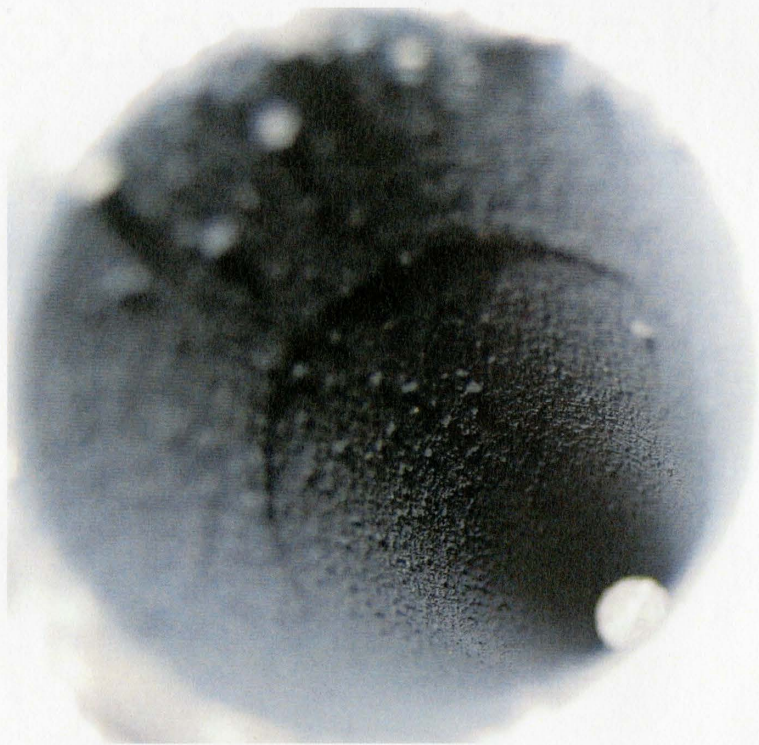


Figure C.4: Digital image of the bottom portion inside the CWCS gas channel at downstream exposed to diesel exhaust gas for 2 hrs at an initial coolant temperature of 20 degrees celcius

12 21A